

**Compact Magnetic Resonance-Guided High-Intensity
Focused Ultrasound Phased Array System**

by
Andre Lafreniere

A Thesis
Presented to Lakehead University
in Partial Fulfillment of the Requirement for the Degree of
Master of Science
in
Electrical and Computer Engineering

Thunder Bay, Ontario, Canada

31 May 2021

Abstract

Andre Lafreniere. Compact Magnetic Resonance-Guided High-Intensity Focused Ultrasound Phased Array System (Under the Supervision of Dr. Carlos Christoffersen, Dr. Laura Curiel, Dr. Samuel Pichardo).

Phased array ultrasound transducers (Tx) can induce electronically controllable localized hyperthermia to tissue deep within the human body. This localized heating can be applied to tumours as an adjunct therapy in multimodal oncology treatments. Magnetic resonance-guided high-intensity focused ultrasound (MRgHIFU) systems utilize imaging techniques to monitor tissue temperature during sonication, providing feedback for control of the Tx's beam-forming. The electromagnetic environment within and near the magnetic resonance (MR) bore restricts the design of driving solutions. The arrays are normally driven by linear amplifiers and matching networks placed at a distance from the MR bore. As clinical arrays can contain over 2000 Tx, this method of driving can result in significant costs and heating.

This thesis proposes a novel MRgHIFU phased array system integration, and an associated rapid design and production processes. The system's array is designed for conformal use in 3T MR head and neck hyperthermia applications. The array is powered using a high-efficiency quasi class-DE (qDE) driving method to yield equal acoustic output from all Tx without use of inductors. This allows the drivers to be placed directly within the MR bore. The driver gating signals are controlled by a field-programmable gate array (FPGA) also placed inside the MR bore.

A rapid design and production process is proposed to facilitate case-by-case target oriented arrays, which yield smaller arrays that can be used as conformal devices. These conformal transducers can help facilitate treatment of targets in challenging locations, and help compensate for patient movement. A Tx casing design was developed for individual ceramics to facilitate repeated removal from various array shells. These removable Tx can be re-used in multiple arrays as they are tuned for qDE driving independent of the array geometry.

A series of MATLAB functions were created to find sparse array designs by running thousands 3D k-space pseudospectral heterogeneous acoustic simulations, varying the pseudo-random Tx positions, array geometry, or steering position between each simulation. The designed functions are used to sweep array geometry and randomized element positions to find a configuration that yields sufficient performance. Once an acoustically correct solution is found, it is verified by executing k-Wave thermal diffusion simulations based on the acoustic simulation's resultant pressure waves. Heating was applied for 30 minutes using a discrete PID controller based on temperature feedback. The array geometry can be exported from MATLAB for use in Autodesk Inventor to 3D print the array exactly as represented in simulation. Multiple groups of Txs were electrically characterized then binned until an appropriate qDE driving solution was achievable.

Active MR testing of the system is currently on hold due to COVID19 restrictions on non-essential hospital operations. If the active MR testing results are successful, the system integration proposed in this work presents a significantly more compact, efficient, and cost effective alternative to systems commonly in use today.

Acknowledgements

I thank my supervisors, Dr. Carlos Christoffersen, Dr. Samuel Pichardo, and Dr. Laura Curiel, for the countless hours they dedicated to thoroughly answering an endless stream of questions, and for their guidance and vision. I also thank my thesis reviewers, Dr. Yushi Zhou, Dr. Adam Waspe, and Dr. Waleed Ejaz, for providing their insightful feedback on very short notice.

I acknowledge Veterans Affairs Canada for providing me with the opportunity to complete these studies under the purview of their Veteran rehabilitation plan.

I am grateful to my wife, Amanda Lafreniere, for her continued support throughout this process.

Andre Lafreniere

Contents

List of Figures	vi
List of Tables	x
List of Symbols	xi
List of Abbreviations	xiv
1 Introduction	1
1.1 Motivations	1
1.1.1 Cost Considerations	1
1.1.2 Conformal Array	2
1.1.3 Driving System	2
1.2 Objectives	3
1.3 Contributions	3
1.4 Thesis Structure	4
2 Background and Literature Review	5
2.1 High-Intensity Focused Ultrasound	6
2.1.1 HIFU Image Guidance	6
2.1.2 Hyperthermia Applications of Head and Neck Tumours	7
2.2 HIFU Phased Array Configurations	9
2.2.1 Array Geometry	9
2.2.2 Transducer Distribution	10

2.3	MR Compatibility	12
2.3.1	Definition of MR Compatibility	12
2.3.2	MR Subsystems and Electromagnetic Theory	13
2.3.3	MR Compatibility of Piezoelectric Drivers	14
2.4	Piezoelectric Transducer Characterizations Theory	16
2.4.1	Lumped Element Circuit Representation	16
2.4.2	Acoustic Conversion Efficiency	17
2.5	Quasi Class-DE Driving Theory	18
2.5.1	qDE Switching Conditions	19
2.5.2	qDE Power Equations	20
2.5.3	qDE Power Balancing Procedure	22
2.6	Acoustic and Thermal Characterizations	23
2.6.1	Acoustic Characterizations	23
2.6.2	Tissue Characterization	26
2.7	Ultrasound Time-Domain Simulation	27
2.7.1	Simulation Implementations	28
2.7.2	k-Wave Toolbox	29
3	Proposed System	32
3.1	Proposed System Overview	33
3.1.1	System Integration	34
3.1.2	Design Process	36
3.2	Acoustic and Thermal Simulations	37
3.2.1	Acoustic Simulation: Initialization & Sequencing	39
3.2.2	Acoustic Simulation: Main Function	39
3.2.3	Heating Simulations	43
3.3	Array Shell and Transducer Fabrication	45
3.3.1	Transducer Casing	46
3.3.2	Array Shell	48
3.4	Quasi Class-DE Power Balancing	49
3.4.1	Transducer Electrical Characterization	50

3.4.2	Transducer Acoustic Conversion Efficiency	51
3.4.3	Calculating qDE Driving Parameters	52
3.5	Driver Printed Circuit Board & Power Supply	53
3.5.1	Driver Printed Circuit Board	53
3.5.2	Driver Board Assembly	55
3.5.3	Power Delivery	57
3.6	FPGA Controller	59
3.6.1	Printed Circuit Board	59
3.6.2	MATLAB Verilog Export	60
3.6.3	Verilog Code and Program Structure	61
3.6.4	Quartus and ModelSim	64
4	Evaluation	67
4.1	Acoustic Simulation Results	68
4.1.1	Solution Validation	68
4.1.2	FUS_Array_RUN_Batch.m Results	69
4.1.3	FUS_Array_RUN_Steering.m Results	74
4.1.4	FUS_Array_RUN_Heating.m Results	75
4.1.5	Discussion	77
4.2	Quasi Class-DE Driver Power Balancing	78
4.2.1	Group A Transducers	78
4.2.2	Group B Transducers	86
4.2.3	Group C Transducers	90
4.2.4	qDE Balancing Discussion	96
4.3	FPGA Simulation	98
4.3.1	Steering Position Phases	98
4.3.2	Combined Steering and Power Balancing	100
4.3.3	FPGA Discretization Limitations	102
4.3.4	MRI B0 Field FPGA Testing	104
4.3.5	Discussion	105
4.4	Electrical Testing	107

4.4.1	Driver Output Voltage Waveforms	108
4.4.2	Discussion	112
5	Conclusions	113
	Appendices	127
A	Extracted Transducer Characteristics	128
B	MATLAB Function Descriptions	131
B.1	Prime Number Search	131
B.2	FUS_Array_GenRandSpherical.m	132
C	MATLAB Simulation Exported Phases	133
D	Driver Printed Circuit Board Schematic	135
E	ModelSim Waveform	137

List of Figures

2.1	Piezoelectric ceramic equivalent circuit.	16
2.2	Quasi class-DE simplified amplifier schematic.	19
2.3	Quasi class-DE waveform diagrams from [72].	19
3.1	Components of proposed system that are placed within MR bore.	33
3.2	Example of system topology for a 16 Tx array.	33
3.3	Proposed layout for MRgHIFU system integration.	35
3.4	A layout often used in existing clinically approved MRgHIFU systems.	35
3.5	Signal flow overview, example of 16 Tx array.	36
3.6	High-level design flow of proposed MRgHIFU modular platform.	37
3.7	High-level flow of solution finding process using MATLAB functions.	38
3.8	FUS_Array.m : flow of process for defining source mask.	41
3.9	FUS_Array.m : Source mask in grid showing focal point (blue) and geometric centre (red).	42
3.10	Picture of assembled array shell and Tx's.	45
3.11	Picture of Tx casings, where the black casings on the far left and right are poly- carbonate.	46
3.12	Tx casing assembly process.	46
3.13	Picture of printed circuit board (PCB) mounted in casing.	47
3.14	Picture of assembled array shell and Tx's.	47
3.15	Picture of array shells.	48
3.16	Picture of FDM printed polycarbonate shell before post-processing.	48
3.17	Python script qDE solution solving process.	49

3.18	NanoVNA-F measurement setup	50
3.19	Picture of acoustic conversion efficiency () measurement processes.	51
3.20	Pictures of assembled driver PCB v1, 70 mm x 70 mm.	53
3.21	Driver PCB v2 trace layout, 70 mm x 50 mm.	54
3.22	Driver PCB v2 3D preview, 70 mm x 50 mm.	54
3.23	Positioning stencil for solder paste on driver PCB.	56
3.24	Picture of an improperly soldered MAX4940 driver.	56
3.25	Power distribution to system components, example of 8 Tx array.	57
3.26	Power supply assembly	58
3.27	Picture of FPGA PCB with optical transducer board attached.	60
3.28	Register-transfer level diagram for an array with 2 TxS.	61
3.29	Register-transfer level diagram for an array with 2 TxS.	62
3.30	Transducer1.v : example of a transducer verilog file.	62
3.31	Timing diagrams to show wrapping effects of phase.	63
3.32	Pulse_Controller.v : structural section of verilog pulse controller module.	64
3.33	Example of ModelSim code and simulated waveform.	65
4.1	3D Visualization of focal point and grating lobe.	68
4.2	Demonstration of layout for heterogeneous medium.	72
4.3	normalized intensity (), 4 points-per-wavelength (PPW) : comparison of homogeneous and heterogeneous mediums.	73
4.4	, 6 PPW : comparison of homogeneous and heterogeneous mediums.	74
4.5	Normalized intensity example in heterogeneous medium.	75
4.6	Heterogeneous heating simulations using kWaveDiffusion.	76
4.7	Group A : S11 magnitude at all 3 resonances around 1 MHz with 10 TxS.	79
4.8	Group A : overall array electrical efficiency () vs. effective power delivered to load () of 10 TxS.	79
4.9	Group A : vs. of 9 tx	80
4.10	Group A, =976 kHz : of 8 TxS.	80
4.11	Group A, =976 kHz : of 8 TxS.	81
4.12	Group A, =976 kHz : of 5 TxS.	81

4.13	Group A,	=976 kHz :	of 5 TxS.	82
4.14	Group A,	=976.5 kHz, DC voltage of the qDE driver ()=60 V:	of 5 TxS.	82
4.15	Group A,	=976.5 kHz, =60 V :	of 5 TxS.	83
4.16	Group A,	: S11 magnitude of 9 TxS.		83
4.17	Group A,	=1070 kHz :	of 7 TxS.	84
4.18	Group A,	=1070.2 kHz :	of 5 TxS.	84
4.19	Group A,	=1070.2 kHz :	of 5 TxS.	85
4.20	Group A,	=1070.2 kHz, =60 V :	of 5 TxS.	85
4.21	Group A,	=1070.2 kHz, =60 V :	of 5 TxS.	86
4.22	Picture of group B TxS.			86
4.23	Group B: wide S11 magnitude of 7 TxS.			87
4.24	Group B: wide S11 magnitude of 7 TxS.			87
4.25	Group B,	: S11 magnitude of 6 TxS.		88
4.26	Group B,	: S11 magnitude of 6 TxS.		88
4.27	Group A,	=294.5 kHz, : overall array electrical efficiency () of 4 TxS, T001 T002 T007 removed.		89
4.28	Group A,	=294.5 kHz : effective power delivered to load () of 4 TxS, T001 T002 T007 removed.		89
4.29	Picture of group C TxS.			90
4.30	Group C : S11 magnitude of 31 TxS.			90
4.31	Group C : S11 magnitude of 26 TxS.			91
4.32	Group C :	vs. of 26 TxS.		91
4.33	Group C : S11 magnitude of 23 TxS.			92
4.34	Group C :	vs. of 23 TxS.		92
4.35	Group C,	=977 kHz, : of 11 TxS.		93
4.36	Group C,	=977 kHz : vs. of 11 TxS.		93
4.37	Group C,	=976.6 kHz, : of 10 TxS.		94
4.38	Group C,	=976.6 kHz, : of 10 TxS.		94
4.39	Group C,	=976.6 kHz, 60 V : of 10 TxS.		95
4.40	Group C,	=976.6 kHz, 60 V : of 10 TxS.		96

4.41	ModelSim : waveform plot with 8 signals from first 4 Tx.	98
4.42	ModelSim : waveform plot with phase of first Tx at first steering position.	99
4.43	ModelSim : waveform plot with phase of 2nd Tx at 2nd steering position.	100
4.44	ModelSim : waveform plot with phase of 3rd Tx at 3rd steering position.	101
4.45	ModelSim : waveform plot with phase of 3rd Tx at 3rd steering position.	101
4.46	Normalized intensity comparing 25 % phase resolutions.	103
4.47	Normalized intensity comparing 50 % phase resolutions.	104
4.48	Pictures of phantom on MRI table with FPGA attached.	105
4.49	Pictures of phantom on MRI table with FPGA attached.	105
4.50	Arbitrary driver parameters a 0 V state in place of the high-impedance state.	107
4.51	time constant () measurement of driver PCB output when loaded with resistor.	108
4.52	No-load driver output voltage with high-impedance state.	109
4.53	No-load driver output voltage with measured phase shifts.	110
4.54	Driver output voltage with Tx's connected, showing a ratio of voltage difference () V measurement.	110
4.55	Driver output voltage with 4 Tx's connected.	111
4.56	Picture of driver output voltage testbench.	112
B.1	FUS_Array_Prime.m : Find prime numbers for grid sizes.	131
B.2	FUS_Array_GenRandSpherical.m : Searching for valid tx positions.	132
D.1	Driver PCB v2 electrical schematic.	136
E.1	ModelSim waveform showing all 48 tx signals for 24 tx array.	138

List of Tables

2.1	MR electromagnetic systems.	13
2.2	Intensity measurement constraints	24
2.3	Average and approximate tissue properties related to HIFU [86]	26
2.4	Ultrasound Simulation Methods	29
3.1	Driver PCB components.	55
4.1	FUS_Array_RUN_Batch.m Batch 1: Homogeneous Results	70
4.2	FUS_Array_RUN_Batch.m Batch 2: Homogeneous Results	71
4.3	Transducer group design criteria	78
4.4	Each Tx's driving parameters for phased array driving frequency ($f_{driving}$)=976.6 kHz at	95
4.5	Each Tx's driving parameters for $f_{driving}$ =976.6 kHz at 60 V.	96
4.6	qDE driving duty and phase combined with steering position phases.	100
4.7	Electrical testing programmed and measured driving parameters.	108
A.1	Extracted transducer characteristic from group A transducers, around	128
A.2	Extracted transducer characteristic from group A transducers, around	129
A.3	Extracted transducer characteristic from group B transducers.	129
A.4	Extracted transducer characteristic from 31 of 40 group C transducers.	130
C.1	Phases [degrees] exported from MATLAB for FPGA implementation.	134

List of Symbols

equivalent model parallel capacitance.

parallel capacitance.

switch paracitic capacitance.

adjustable external capacitance.

duty.

acoustic focusing gain.

intensity gain.

pressure gain.

intensity.

spatial-average pulse-average intensity.

spatial-average temporal-average intensity.

spatial-peak pulse-average intensity.

spatial-peak temporal-average intensity.

spatial-peak temporal-peak intensity.

grating lobe acoustic intensity level.

acoustic intensity level.

total power loss from the driver.

driver gate power loss.

effective power delivered to load.

driver resistive power loss.

estimated driver switching power loss.
average power delivered to each elements in array after
balancing.
power delivered to load.
minimum power delivered to load.
no-load power.
quality factor of the series resonant branch.
volumetric rate of heat deposition.

switch resistance.
average temperature.
DC voltage of the qDE driver.

transducer impedance.
phase.
attenuation.
attenuation coefficient.
ratio of voltage diference.
observed ratio of voltage difference.
overall array electrical efficiency.
acoustic conversion efficiency.
conduction angle.
density.
power law exponent.
sound speed.
frequency.
parallel-resonant frequency.
series-resonant frequency.
phased array driving frequency.
pressure.

p negative pressure.
 p_{sptp} spatial-peak temporal-peak pressure amplitude.

List of Abbreviations

	cumulative equivalent minutes at $^{\circ}$.
<i>in vivo</i>	within the living.
CMUT	capacitive micro-machined ultrasonic transducers.
FD	finite difference.
FDA	United-States food and drug administration.
FE	finite element.
FPGA	field-programmable gate array.
HIFU	high-intensity focused ultrasound.
IC	integrated circuit.
IE	integral equation.
INCS	iterative nonlinear contrast source.
MI	mechanical index.
MR	magnetic resonance.
MRgHIFU	magnetic resonance-guided high-intensity focused ultrasound.
MRI	magnetic resonance imaging.
MRT	magnetic resonance thermometry.
PCB	printed circuit board.
PS	pseudospectral.
PWM	pulse-width modulation.
PZT	piezoelectric.
qDE	quasi class-DE.
S11	scattering parameter reflection coefficient.

TID	thermal isoeffective dose.
Tx	transducer.
USgHIFU	ultrasound-guided high-intensity focused ultrasound.
VNA	vector network analyzer.
ZDS	zero derivative switching.
ZVS	zero voltage switching.

Chapter 1

Introduction

1.1 Motivations

Developing a magnetic resonance-guided high-intensity focused ultrasound (MRgHIFU) phased array device is a costly and time consuming endeavour. This is a result of both the technical complexity and extensive testing required for clinical approval. To justify this large initial investment, the potential applications of such devices must be sufficiently financially compelling. The most common application of HIFU has been tissue ablation, where a high-power device quickly heats a target.

As a result of these circumstances, most of today's MRgHIFU devices are designed as single-unit solutions, capable of high-power ablative therapies on numerous locations. This is achieved by employing a high number of independently driven piezoelectric ceramics to create a sufficiently large steering range, and to generate sufficient acoustic power.

1.1.1 Cost Considerations

The potential clinical applications of MRgHIFU technology are both numerous and rapidly expanding. Applications which cannot be tested with existing clinical devices run into a significant financial barrier in early-stage research. These potential applications then justify the financial investment required to develop new MRgHIFU devices.

To lower the cost of early-stage research, this thesis proposes a modular system and design process that can be used to rapidly design and develop MRgHIFU devices at low cost. Individual Tx's in an array can be reused on multiple arrays, allowing for rapid transitions between array geometries.

1.1.2 Conformal Array

The disadvantages of large multi-purpose MRgHIFU systems extends beyond the fiscal dimension. The first major disadvantage is their size. The required steering range and power of multi-purpose ablative systems results in a larger array geometry. They are often placed within an MR table, as empty space within the MR bore is limited. The patient must then be positioned in such a way that the clinical target is properly exposed to the table. This can make treatment of certain volumes challenging or impossible. For head and neck tumours in particular, acoustically sensitive boundaries, such as the throat, can be subjected to surface burning if the acoustic beams are not properly angled.

The second major disadvantage of traditional MRgHIFU array designs is the relative motion between it and the patient. Patient movement during sonication requires detection and compensation within magnetic resonance imaging (MRI), however MRI thermometry cannot immediately correct for patient movement.

1.1.3 Driving System

The electrical driving systems which power MRgHIFU arrays have predominantly relied on using LC matching networks to both compensate for individual piezoelectric Tx performance, and to match the driving network to high impedance piezoelectric Tx's. The driving system is often placed outside of the MR bore room, or are heavily shielded within the MR table due to the incompatibility of the inductors with the MR environment. As normally each Tx on the array must be independently driven, there is significant costs and inefficiency associated with these driving methods.

This thesis proposes a system integration which uses a qDE method to power the array. The qDE driving method allows for driving at high efficiency from directly within the MR bore, while ensuring equal acoustic power is delivered from each Tx. Gating signals are generated directly within the MR bore using a FPGA.

1.2 Objectives

The primary objectives of this thesis are:

1. to design a compact MRgHIFU phased-array system integration utilizing qDE driving, and
2. to tailor the array design for hyperthermia applications of head and neck tumours.

This thesis also aims to accomplish two secondary objectives in the interest of its long term impacts:

1. to ensure the design of the system, including the array, is modular such that elements can be reused on various array shells, and
2. to create and document a design process that facilitates use of the proposed system as a low-cost open-source platform.

1.3 Contributions

This thesis contributes to the field of HIFU by proposing and designing an MR compatible, compact, modular, and low-cost system integration for future use as an open-source platform. The proposed transducer array may facilitate HIFU applications not possible with existing clinical systems, such as challenging targets in hyperthermia applications for head and neck cancer.

Due to its low cost and modularity, the proposed system could make a significant impact in early-stage HIFU research. The array shells are 3D printed exactly as simulated due to the design process used. A threaded ceramic casing was developed to reliably and accurately hold a piezoelectric ceramic within a printed array shell. The threaded casings also allow those ceramics to be reused in various array bodies, and they are tuned independently of array geometry using a recently proposed qDE driving method. These features allow for rapid testing of various 3D printed array shells using the same set of elements. The rapid production process allows arrays to be designed on a case-by-case basis, customized to the unique features of a target. Cost is further reduced by using a FPGA to generate the driver gating signals from directly within the MR bore.

The results of this thesis demonstrate the potential of the proposed low-cost conformal phased array system integration for the application of head and neck hyperthermia. The proposed design and design process are estimated in both simulations and through electrical testing. Further work is needed in fully validating the system for use as an open-course platform, such as including hydrophone and MR imaging verification, however, the results documented in this thesis are encouraging. No results were found which would discourage the further pursuit of this work.

1.4 Thesis Structure

This thesis is structured into four chapters following the introduction. Chapter 2 reviews background theory and literature relevant to the system's unique components, design processes, and for MRgHIFU head and neck hyperthermia applications. Chapter 3 presents the proposed system integration and design process. Chapter 4 discusses simulation results for various design configurations, and electrical testing results for a prototype. Throughout Chapter 4 examples are provided to further explain and justify the design process proposed. Chapter 5 concludes the thesis by summarizing the results, discussing the difficulties encountered, and advises on the next steps required to further verify and advance this system integration as an open-source platform.

Chapter 2

Background and Literature Review

This chapter presents a combination of literature review and background information regarding the proposed MRgHIFU system integration. A vast amount of background information is applicable due to the interdisciplinary nature of the system. Due to this wide scope, the depth and completeness of literature reviewed and background information presented for each topic is limited.

The topics covered in this chapter focus on presenting the information required to understand and justify the novel aspects of the system integration. These topics include: providing a basic understanding of the intended application, MR compatibility concerns regarding the electrical systems, theory regarding piezoelectric (PZT) transducer characterizations and the qDE driving method, the physical configuration of the phased-array, and the simulation methods used to validate the array design.

The topics related to clinical application focus more heavily on literature review than theory, while topics related to the electronic subsystems focus more on theory.

2.1 High-Intensity Focused Ultrasound

This section contains a literature review and presents background information regarding MRgHIFU applications and technology. The review focuses on head and neck hyperthermia applications, and covers MR compatibly PZT Tx driving systems.

2.1.1 HIFU Image Guidance

HIFU devices can deliverer high levels of acoustic energy inside the human body, concentrating at the device's acoustic focal point. This energy results in local tissue temperature elevation, which is used for many non-invasive therapeutic purposes including hyperthermia and tissue ablation. HIFU is considered a disruptive technology with the potential to improve the treatment of numerous medical disorders [1]. The United-States food and drug administration (FDA) has approved HIFU in clinical treatments of uterine fibrosis, bone metastasis, essential tremor, Parkinson's disease, prostate cancer, and benign prostatic hyperplane. Many more pivotal trials are underway for HIFU including in treatments of breast cancer, hypertension, various musculoskeletal cancers, endocrine disorders, liver metastasis and tumours, various neurological disorders including depression, obsessive-compulsive disorder, neuropathic pain, and more.

HIFU was first proposed as a non-invasive alternative to surgery by Lynn in 1942 [2], [3]. The first clinical HIFU device was guided by x-ray in Jul. 1960 [4]. In 1988 the FDA approved the first HIFU device, the Sonocare CST-100 Therapeutic Ultrasound System, for the treatment of glaucoma [5]. HIFU was not widely accepted in clinical practices until the development of better imaging modalities occurring during the 1990's [6]–[8].

Variation and layers of tissues within the body create a heterogeneous path for ultrasound propagation. This distorts ultrasound beams which can induce unwanted lesions [9] and heating in surrounding tissue. This resulted in requiring extensive experimental studies to develop an effective treatment procedure [3]. To develop safe procedures and compensate for the unwanted lesions and heating effects, feedback imaging of the treatment volume is crucial [7]. HIFU was not combined with MRI until 1991, where Hynynen, Darkazanli, Unger, *et al.* proposed using MRI to evaluate tissue damage induced by the ultrasound [3], [8]. At that time, ultrasound imaging was used for imaging of lesions for feedback [10], but was not accurate enough to make noninvasive ultrasound surgery a reliable clinical tool [3].

In addition to detailed lesion detection, magnetic resonance thermometry (MRT) utilizes MRI techniques to monitor temperature coagulation during treatment, and has excellent soft tissue contrast for treatment planning and evaluation. Despite the advantages offered by MRgHIFU, ultrasound-guided high-intensity focused ultrasound (USgHIFU) is more widely used, with the primary advantages being: lower cost, more compact and portable, and has high temporal resolution [11]. The first MRgHIFU device was approved for clinical usage by the FDA in 2004 for the treatment of uterine fibroid [11], [12].

2.1.2 Hyperthermia Applications of Head and Neck Tumours

Hyperthermia is used in cancer therapy typically as an adjunct therapy in multimodal oncological [13], [14]. It has extensively been proven effective in clinical studies when combined with radiation therapy [15]–[19]. Interactions between hyperthermia and vascular disrupting agents such as chemotherapeutic drugs have also been shown to enhance thermoradiosensitisation [20], [21].

Hyperthermia Therapy

The effects of hyperthermia on cells structures and interactions between proven adjunct therapies is complex and still under investigation [22], [23]. One of the more widely accepted effects is due to the tumour's hypoxic cells, which reduce blood supply to the area. Through multiple studies hyperthermia has been shown to reduce tumour hypoxia and increase tumour sensitization to ionizing radiation [23], [24].

Localized hyperthermia therapy raises tissue temperature in a select volume to a fixed value, typically between 40° to 43° . The tissue is held at that temperature for a specified period of time determined based on a prescribed thermal dosage. In the early 2000s localized hyperthermia was typically induced using radiowave and microwave antennas and applicators [13]. The benefits of ultrasound frequencies, however, have long been known [25]. In comparison to radio and microwave hyperthermia, ultrasound benefits for hyperthermia applications come from its shorter wavelength and favourable acoustic absorption, allowing for smaller focal regions and better depth of penetration [26].

The optimum clinical dosages for temperature, radiation, and associated time intervals remains largely unknown, but more recently progress has been made in quantifying these relationships [14], [27]–[29].

Head and Neck Cancer

Cancer of the head and neck is the 6th most common form of cancer worldwide. Head and neck squamous cell carcinomas (HNSCCs) make up the majority of these cases, accounting for over 500,000 new cases annually [30], [31]. The common treatment options include multimodal uses of radiotherapy, surgery, and chemotherapy. These therapies are often ineffective, and severely reduce patient quality of life [30]. The overall 5-year survival rate of HNSCCs remains around 40–50% [31]. 20–55% develop local reoccurrence after initial treatments [32] with a median overall survival time in cases of reoccurrence of less than 1 year [33], [34]. HNSCCs can be highly hypoxic, limiting the effectiveness of radiotherapy. More recently, immunotherapy has also been approved by the FDA, with trials showing an improved overall survival rate [31], [35].

Localized hyperthermia as an adjunct treatment to radiotherapy and/or chemotherapy for treatment of head and neck tumours has been proven effective over a number of phase III trials. Reference [36] summarizes the results of four randomized phase III trials which used radioactive, capacitive, and conduction resistive wire localized heating technologies. The clinically significant results were undermined by limitations in the technology used to induce hyperthermia [36]. This technology made quantifying optimal thermal dosages unlikely, results too unpredictable, and/or was limited to superficial regions [34]. Paulides, Verduijn, and Van Holthe proposed using MR thermometry to guide an RF applicator called HYPERcollar [36].

Hyperthermia as an Adjunctive Therapy for HNSCCs

An *in vivo* study proposed using MRgHIFU as an adjunct therapy to radiotherapy for the treatment of recurrent head and neck tumours [37]. This study implemented proton resonance frequency shift-based thermometry using a pencil-beam navigator to compensate for respiratory motion. The level of noise was found to be reduced considerably using a multi-baseline technique, however, it was noted that this technique cannot compensate for out of plane artifacts, unpredictable motion, and requires a pre-fill time [37]. A pilot study was proposed in 2016 [38] to assess safety, toxicity, and feasibility of MRgHIFU induced hyperthermia as proposed in [37].

2.2 HIFU Phased Array Configurations

The operating environment within the MR bore imposes significant restrictions to the design and implementation MR compatible HIFU devices. Mechatronic equipment within or near the MR bore must adhere to strict design criteria, limiting implementation of typical mechanical solutions for steering single PZT ceramic TxS [39]. Because of these limitations, electronically steered arrays garnered attention as an MR compatible solution [40].

Electronically controlling the Tx's ultrasound pattern allows for adjustments of focal point position, shape, size, and number of points. In MRgHIFU systems, this allows for real-time guidance of heating patterns based on MRT feedback. Phased array Tx can be used in multi-focus, moderate focus, or sharp focus modes, which can considerably reduce treatment time when optimized for tumour geometry [41] [42]. For hyperthermia treatments, multi-focal HIFU has been shown to reduce peak acoustic pressure [43], more evenly distributing it across the heating area. This can reduce undesirable cavitation [44] and tissue ablation.

The major disadvantages of electronic steering is the formation of undesired secondary lobes and resultant near-field heating [41], [45], and the added complexity of driving and controlling the large number of TxS [26].

Selection of the ultrasound frequency is largely dependent on the clinical application. The coefficient of attenuation in soft tissues is typically around $0.3 \text{ dBcm}^{-1} \text{ MHz}^{-1}$ [46]. In applications requiring greater depth of penetration, the attenuation of higher frequencies can be prohibitive.

2.2.1 Array Geometry

In 1984 a planar stacked linear phased array was proposed as a HIFU hyperthermia applicator [26]. This configuration is able to electronically steer the focal point in all 3-dimensions, however it requires a large number of TxS to prevent the formation of secondary lobes.

Concentric-ring and sector-vortex configurations were evaluated in 1986 [47]. These configurations require fewer TxS to eliminate secondary lobes than stacked linear arrays, however they can only effectively steer along 1-dimension.

A cylindrical-section configuration was proposed in 1988 by Ebbini, Umemura, Ibbini, *et al.* [48]. The proposed configuration could only steer in 2-dimensions, however when compared to a comparable linear array, there were improvements in intensity gain and a reduction in secondary lobe magnitude.

Ebbini, Umemura, Ibbini, *et al.* later proposed a spherical-section ultrasound configuration [40]. The array was designed such that the natural focus of the Tx was at the geometric centre of the array's curvature. This configuration provided 3-dimensional steering with improved intensity gain and decreased secondary lobe magnitude when compared to a planar array of similar dimension.

In 1996 Fan and Hynynen noted geometry considerations for spherical-section arrays, determining that large f-number (radius of curvature / aperture) arrays were not optimal for ultrasound surgery. A low f-number can help to reduce near-field heating.

2.2.2 Transducer Distribution

The distribution configuration of individual Txs on the phased array surface has a significant effect on performance. Early HIFU phased arrays used in imaging were designed such that an inter-element spacing of $\lambda/2$ could be achieved, where λ is the ultrasound wavelength [50]. This restriction was employed to limit the formation of grating lobes. The intensity gain required for HIFU hyperthermia treatments require a larger aperture than imaging devices. As the wavelength of a 1 MHz ultrasound signal in water is around 2 mm, the number of Txs required limited practical implementation. The use of non-planar arrays reduced this restriction. In [40] a spherical-section array with $\lambda/2$ inter-element spacing was simulated in a homogeneous medium with shifted focus positions, showing sufficient performance for deep tissue penetration.

A sparse random distribution of circular Txs on a spherical-section array was evaluated in 1996 [50]. The proposed distribution was able to reduce the number of Txs and driving channels while maintaining intensity gain by increasing the Tx size. 64 circular 8 mm diameter Txs were randomly distributed on a spherical array with a aperture of 100 mm and a radius of curvature of 102 mm. The theoretical results were compared to a 108 Tx hexagonal array using regularly spaced Txs. The hexagonal array produced unacceptable grating lobes, while the random array did not with a steering range of up to 5 mm off axis.

In 2000 the relative performance of Tx distribution configurations for spherical phased arrays was assessed [51]. The cases of annular, hexagonal, square, and random distributions were explored for spherical arrays of 255 Tx with 5 mm. In both single-focus and multi-focus modes, the randomly distributed array demonstrated marked improvements in intensity distribution. In single focus mode, it was found that the sparseness of the random array needed to be within an active area of approximately 40 to 70% for the benefits of randomization to be achieved. For the random distribution in [51], a quasi-random distribution was used such that minimum separation between centres of Tx was 5.5 mm. Several quasi-random distribution patterns were investigated but yielded similar results.

A disadvantage for sparse random Tx distribution is that surface coverage is sparse, reducing the maximum power that can be delivered to the focal point. This can be a significant limitation for higher power applications such as deep tissue and ablation.

A single archimedean spiral distribution was proposed in [52], demonstrating its potential to increase surface density while maintaining the use of circular Tx, however, it was not been thoroughly compared to the performance of sparse random arrays.

More recently, methods of array Tx distribution and shape were proposed such that array surface coverage is fully populated, while maintaining comparable grating lobe performance when compared to a sparse random array [52], [53]. In [53], space-filling non-periodic tiling techniques using non-circular Tx were used to demonstrate the potential of these techniques. This technique was further improved in [52]. As hyperthermia applications can be less dependent on maximizing surface coverage of the phased array Tx, further exploration of these techniques will not be discussed as the required manufacturing techniques are sufficiently prohibitive.

2.3 MR Compatibility

MRgHIFU devices contain conductive, paramagnetic, and potentially ferromagnetic materials, and can emit or sink electromagnetic signals. Understanding of MR clinical practices, MR subsystem behaviour, and electromagnetic principles are important for the development of MR compatible electronic devices. Devices operating within the MRI bore should not be developed in isolation from electromagnetic considerations of MR subsystem behaviour. The MR subsystems are indirectly connected to electronic devices within the MR bore through electromagnetic interactions.

2.3.1 Definition of MR Compatibility

Most early literature focused on defining and qualifying MR safety [54] [55], [56]. Ensuring that a device placed within the MR environment is MR safe is critical from a clinical perspective, but does not fully encompass considerations that need to be made when designing a MRgHIFU device.

A device is MR safe when it does not add risk to human or equipment when in the MR environment [39]. An early definition of MR magnetic compatibility and the compatibility of various materials was presented in [57]. A more complete early characterization of MR compatibility was published by GE Medical Systems in 1997, as detailed and in [39]. In it, an MR compatible device is defined as a device that is MR safe, its use does not affect MR imaging quality, and it operates as intended in the MR environment.

Reference [58] summarized and connected practical aspects of risk management to fundamental electromagnetic principles. Draft guidance issued by the FDA in 2019 provides broad guiding the testing and labelling medical devices for safety in the magnetic resonance (MR) environment [59].

2.3.2 MR Subsystems and Electromagnetic Theory

The MR imaging systems use multiple electromagnetic subsystems. The interaction between these electromagnetic systems and devices placed within or near the MR bore can be understood through classical electromagnetism; Maxwell's equations and Lorentz force law. The basic systems that are part of a MR imaging machine are described in Tab. 2.1. The predominant electromagnetic interactions that should be considered between these systems and any electrical device placed within the MR bore will be described throughout the remainder of this section.

Table 2.1: MR electromagnetic systems.

MR Imaging Physics	Electromagnetic System
Spin Polarization	DC magnetic field augmented by shimming and fringe fields create the main magnetic field aligned along z-axis.
Spin Excitation	RF excitation coils introduce an oscillating field on the x-y plane, perpendicular to the field.
Spatial Localization	Magnetic field created by gradient coils impose sequenced spacial gradients to the field.
Spin Detection	RF receiver coils detect free induction decay (FID) and/or echo signals from magnetized protons within target.

Static Magnetic Field

The field is normally created using permanent magnets or resistive (air core) magnets for lower-field applications, and superconducting magnets for higher-field applications. Superconducting magnets paired with a cylindrical bore topology is the most common method of generating the field in hospital MRI systems [58], [60]. A stronger field strength is often desirable due to the the potential of increasing the signal-to-noise ratio [61], [62]. As the signal-to-noise ratio increases, the uncertainty of MR thermometry temperature measurements decreases.

A MR compatibility concern caused by the field is anticipated with the presence of ferromagnetic materials. These materials distort the field, which often result in image distortions. Paramagnetic materials such as copper and aluminum can also create relevant distortions in , especially when present near the target volume [39]. The field also induces a torque in ferromagnetic objects [63].

Gradient Fields G_x , G_y , G_z

The gradient fields G_x , G_y , G_z are magnetic fields generated by orthogonal gradient coils, superimposed over the B_0 field to create a spacial variation in magnetic field strength. The fields can be static during portions of an imaging sequence, but is not static when considering an entire imaging sequence. Rapid sequencing of G_x , G_y , G_z can result in a significant $\frac{dB}{dt}$ component. Based on the Maxwell–Faraday equation, the $\frac{dB}{dt}$ component could induce a varying electric field in conductors placed within the MR bore.

The gradient fields also pose another constraint on MR compatibility of objects placed within the bore. The variances they create in the B_0 field is the primary cause of displacement forces in ferromagnetic objects [58].

RF Excitation and Receiver Coils

The RF excitation coil(s) transmit RF pulses within the MR bore, typically between 3 to 100 MHz [60], depending mostly on the strength (Tesla) of the B_0 field. The magnetic component of the RF pulse (B_1) is what the MR system uses for imaging, however the electrical component can still adversely affect conductive materials inside the MR bore by inducing voltages in conductors.

2.3.3 MR Compatibility of Piezoelectric Drivers

The piezoelectric (PZT) ceramics used in HIFU phased array applications often have a diameter and operating frequency that results in an equivalent high impedance. This results in a large mismatch between standard driving systems [64], which are customarily designed with a 50 Ω output impedance [65]. These Tx's are also subject to manufacturing variance. This can come from multiple sources including the ceramics themselves and variance in the clamping forces imposed by their casing. Variance can also come from the medium acoustic properties and temperature the wave is propagating towards, but that will not be discussed as part of this thesis.

As a result of these requirements, matching networks are typically used in MRgHIFU systems to improve efficiency, prevent power from being reflected back into the amplifier, and ensure equal acoustic power is delivered from all elements. The matching networks typically require large inductors with ferromagnetic cores, which are generally incompatible with the MR environment.

With multiple FDA, CE, and Health Canada approved MRgHIFU clinical devices [66] containing around 1000 Tx, the matching networks required to independently drive each element of an array can be a costly, space consuming addition, and inefficient endeavour.

MR Compatible Driver Technology

Several methods of driving PZT Tx without inductors have been proposed. Use of a low output impedance amplifier was proposed in 2009 [65], however the solution results in square wave excitation of the piezoelectric ceramics. Maximum power delivered to the ceramic is good, but it does not consider the acoustic conversion efficiency of square wave excitation. In 2014 two new driving topologies were proposed. A push-pull design was proposed [67], but it did not consider efficiency or harmonic distortion performance. A high bandwidth low distortion linear amplifier was also proposed, but it resulted in low efficiency [68].

The efficiency of both the electrical drivers and acoustic conversion of the piezoelectric Tx are important considerations for MRgHIFU systems. Inefficiency in high-power HIFU devices results in significant heat, potentially limiting implementation near the patient. The MR bore imposes space and electromagnetic restrictions, limiting implementation of both passive and active heat removal solutions.

In 2016 a class-DE amplifier was proposed [69], [70] that offers inductorless matching, high efficiency, and may be MR compatible. This amplifier achieves high efficiency by minimizing switching losses through adherence to the zero voltage switching (ZVS) and zero derivative switching (ZDS) conditions. The proposed method of driving allows for operation between the series and parallel resonance frequencies, where the frequency of maximum acoustic conversion efficiency exists. Despite the most efficient acoustic conversion frequency being in this region, conventional driving topologies do not make use of it due to the inductive input impedance of the piezoelectric ceramic [71].

A quasi class-DE (qDE) driving method was proposed by Christoffersen, Ngo, Song, *et al.* in 2019 [72], which further improves class-DE driving methods of 2016 to compensate for impedance variations of each Tx. This method of driving is further discussed in Sec. 2.5.

A compact class-D driver was recently proposed for capacitive micro-machined ultrasonic transducers (CMUT) technology [73], however the output power and overall efficiency were low.

2.4 Piezoelectric Transducer Characterizations Theory

HIFU phased arrays typically require equal acoustic power delivered from each PZT ceramic. As such, each Tx should be individually electrically characterized in order to properly compensate for their individual variance with the driving system. This is often accomplished by two characterizations: by representing the PZT ceramic as a lumped element circuit, and measuring the acoustic conversion efficiency.

2.4.1 Lumped Element Circuit Representation

The impedance of a piezoelectric ceramic can be represented near isolated resonant frequencies by the lumped-parameter equivalent circuit shown in Fig. 2.1 [74], where L is the inductance of series resonant branch, R is the resistance of series resonant branch, C is the capacitance of series resonant branch, and C_p is the equivalent model parallel capacitance. This circuit is also known as a Butterworth Van Dyke (BVD) circuit.

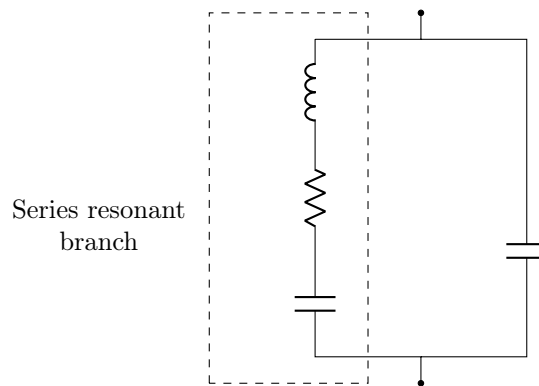


Figure 2.1: Piezoelectric ceramic equivalent circuit.

The magnitudes of these components are approximately independent of frequency on a narrow band near the resonant frequency [74], [75]. More complex equivalent circuit models exist [74] that account for transients, however these are not required for the purpose of this thesis. For this thesis, the Txs are characterized to the components of Fig. 2.1 in accordance with the process described in [76].

The circuit components can be calculated from the measured series-resonant frequency (f_s), parallel-resonant frequency (f_p), and impedance at the series-resonant frequency (Z_s). These measurements are found by recording then converting the scattering parameter reflection coefficient (S11) parameters to impedance form for a 20-100 kHz bandwidth around the selected resonant frequency. f_{maxG} is defined as frequency of maximum conductance (resistance), and Z_{min} is the impedance value as this frequency. f_{maxR} is defined as the frequency of maximum resistance.

This is derived based on the BVD model in [76] to the following equations:

$$\text{—————} \tag{2.1}$$

$$\text{—————} \tag{2.2}$$

$$\text{—} \tag{2.3}$$

$$\text{—————} \tag{2.4}$$

2.4.2 Acoustic Conversion Efficiency

The acoustic conversion efficiency of a Tx can be found using the radiation force method outlined in *IEC 61161:2013* [77]. *IEC 61161:2013* specifies a method of determining the total acoustic power of certain ultrasound Txs. This measurement is important as the acoustic power delivered from each Tx on an array should be equal. The acoustic conversion efficiency (η) is determined by comparing the acoustic power emitted from the Tx and electrical power delivered to it.

For this thesis the test was done with a perfectly absorbing target was considered, and the face of the Tx was placed as close as possible to the absorbing material to negate the effects of the water's absorption. The water was degassed to minimize the effects of cavitation on the radiation force measurements. As a result, the relationship between pressure and force can be simplified to $F = \frac{P^2}{\rho c}$, where P is the pressure, c is the sound speed in water, and F is the radiation force. The sound speed in water is calculated using the formula presented in [78] based on it's temperature

(T), as shown in the following equation:

$$c_{water} = 1402.736 + 5.03358 * T - 0.0579506 * (T^2) + 3.31636 * (10^{-4}) * T^3 - 1.45262 * (10^{-6}) * (T^4) + 3.0449 * (10^{-9}) * (T^5). \quad (2.5)$$

The force exerted on the absorbing medium is measured by a connected balance and measuring the difference with and without the Tx transmitting. The difference in weight is then converted to force depending on what the scale is measuring.

2.5 Quasi Class-DE Driving Theory

The quasi class-DE (qDE) driving method proposed [72] improves on the class-DE driving method by compensating for the impedance variations of each Tx. This ensures equal acoustic power is delivered from all Txs in an array. In similarity to the class-DE driving method, the quality factor of the series-resonant branch, shown in Fig. 2.1, must be high. In comparison to the standard class-DE driving method, for the quasi class-DE method the ZVS condition is relaxed. The compensation for variation in Tx characteristics is accomplished through use of a push-pull switch, an external capacitor, and fine control of the duty (D) of each Tx.

The capacitors in parallel shown in Fig. 2.2 can be grouped and described as the parallel capacitance (C_P), where $C_P = C_{ext} + C_{SW} + C_0$. When both switches are open, C_P supplies the load current to the Tx. The length of the signal path between the Tx and the driver should be small enough to ensure the transmission line effects between them are negligible. The circuit topology is shown in Fig. 2.2, where C_{SW} is the switch parasitic capacitance, C_{ext} is the adjustable external capacitance, v_O is the output voltage, and V_{DE} is the DC voltage of the qDE driver.

The waveform diagram in Fig. 2.3 describes the behaviour of the qDE push pull switching method. In this figure, ϕ is the conduction angle, ΔV is the voltage difference when the switch is turned ON, and t_{on} is the duration that the switch is on. The inductive reactance of the PZT ceramic is used to charge and discharge the parallel capacitors when both switches are off. This allows the switching voltage to be greatly reduced, improving the efficiency by minimizing switching losses.

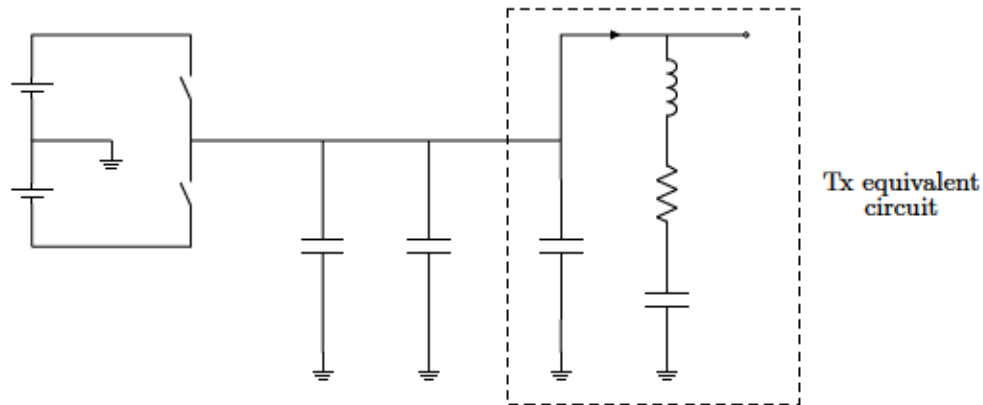


Figure 2.2: Quasi class-DE simplified amplifier schematic.

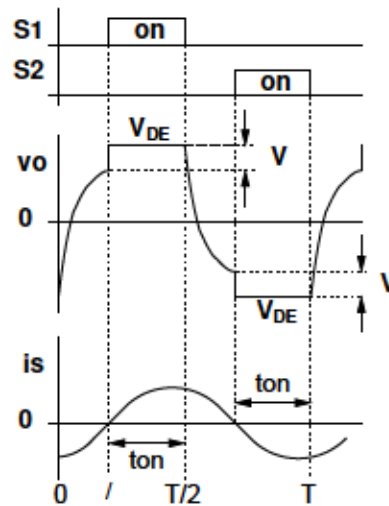


Figure 2.3: Quasi class-DE waveform diagrams from [72].

2.5.1 qDE Switching Conditions

The impedance conditions of the series resonant branch for ZDS are derived in [72] under the assumptions: (1) switch resistance () is negligible, (2) capacitors are ideal, (3) the quality factor of the series resonant branch () is high (normally 10 or more), (4) higher current harmonics are negligible, and (5) the transient state during charging () is negligible.

The switching scheme shown in Fig. 2.3 is used to define the conduction angle (θ), duty (D), and ratio of voltage difference (α) based on the following equations:

$$\text{---} \quad (2.6)$$

$$\text{---} \quad (2.7)$$

$$\text{---} \quad (2.8)$$

The conditions for ZDS for the circuit shown in Fig. 2.2 and defined by the waveforms of Fig. 2.3 are derived in [72] to the following equations:

$$\text{---} \quad (2.9)$$

$$\text{---} \quad (2.10)$$

where X_s is the reactance of series resonant branch, given by $X_s = \omega L_s - 1/\omega C_s$.

If the ratio of voltage difference (α) is equal to zero, the condition for ZVS is also met. If the ZVS is zero, then the Tx is operating in class-DE mode, and eqs. (2.9) and (2.10) become the same as the conditions derived in [69].

2.5.2 qDE Power Equations

The switching conditions eqs. (2.9) and (2.10) are used in conjunction with the lumped element circuit parameters derived in Sec. 2.4.1 to balance the power between Tx's in the array, provided a solution is available. As the phased array driving frequency (ω) and voltage of all Tx's in the array are constant for all elements, power must be varied for each Tx by varying the adjustable external capacitance (C_{ext}) and duty (D) for each Tx.

Not all arrays are guaranteed to be compatible with quasi class-DE driving, especially if parameter variance between Tx's is large and/or the quality factor is low. If the C_{ext} and D vary too greatly between Tx's, an Q may not exist. Additionally, the impedance of the series branch shown in Fig. 2.2 may not remain inductive enough to allow power balancing adjustments of C_{ext} while considering the overall value of Q .

The qDE method proposed partially considers I_{eff} by including it in power derivations. It is considered in calculating the effective power delivered to load (P_{eff}) by considering its effects on the peak current, as shown in the following equation:

$$P_{eff} = I_{eff} V_{peak} \quad (2.11)$$

where I_{eff} is the effective peak current. The I_{eff} is calculated by considering the average load peak voltage (V_{avg}). This is accomplished using the following equations:

$$I_{eff} = \frac{V_{avg}}{Z_{load}} \quad (2.12)$$

$$V_{avg} = \frac{V_{peak}}{2} \quad (2.13)$$

where I_{avg} is the average current through switch during the conduction interval.

The V_{avg} is also taken into consideration when calculating estimated driver switching power loss (P_{sw}) through finding the observed ratio of voltage difference (V_{ratio}) anew. This process is shown in the following equations:

$$V_{ratio} = \frac{V_{avg}}{V_{peak}} \quad (2.14)$$

$$P_{sw} = I_{avg} V_{ratio} \quad (2.15)$$

The total power loss from the driver (P_{total}) is the sum of power losses from each source considered: $P_{total} = P_{sw} + P_{res}$, where P_{sw} is the estimated driver switching power loss and P_{res} is the driver resistive power loss. For this section, power refers to the average power. P_{sw} and P_{res} are found using the following equations:

$$P_{sw} = I_{avg} V_{ratio} \quad (2.16)$$

$$P_{res} = I_{avg}^2 R_{driver} \quad (2.17)$$

where P_{sw} is the driver gate power loss, which can be measured from the driver.

The overall array electrical efficiency (η_{array}) is defined as the ratio between P_{array} and P_{in} :

$$\eta_{\text{array}} = \frac{P_{\text{array}}}{P_{\text{in}}} \quad (2.18)$$

2.5.3 qDE Power Balancing Procedure

The procedure for balancing a group of Tx's is described in [72] as follows:

1. Characterize the Tx's, as described in Sec. 2.4.
2. Select a frequency range to consider between the highest f_{max} and lowest f_{min} of all Tx's.
3. Set f for all Tx's, and for a number of frequency points within the range, solve for P_{array} in eq. (2.10). Use that value of P_{array} to solve for P_{in} in eq. (2.9). If $P_{\text{in}} > P_{\text{max}}$, obtain a new value for f by setting $P_{\text{in}} = P_{\text{max}}$ and solving for f and P_{array} in eqs. (2.9) and (2.10). Then use these values to calculate η_{array} from eq. (2.11).
4. Balance the power output of all Tx's to the lowest P_{array} found by increasing the f of each.
5. Calculate the final array power and efficiency, and redesign or bin Tx's as appropriate.

2.6 Acoustic and Thermal Characterizations

This section will discuss some of the governing equations used for simulating the acoustic and thermal effects the Tx, related acoustic and thermal variables are defined, and the tissue properties used are listed.

Ultrasound waves in a homogeneous lossless fluid can be described though the combination of 3 first order differential equations, and when combined, the resultant equation is known as the second order wave equation. Absorption and dispersion can be included in this model of wave propagation using the fractional Laplacian [79].

Prior to the fractional Laplacian method, typical methods of accounting for these parameters in the wave equation utilized convolution based time-domain fractional operators [79]. The proposed fractional Laplacian modelling represents the power law absorption and dispersion using two lossy derivative operators, allowing for incorporation into global Fourier transform computations using the k-space pseudospectral method. This method is further discussed in Sec. 2.7.

2.6.1 Acoustic Characterizations

Acoustic pressure (p) and intensity (I) measurements, and the associated methodology, are commonly documented in HIFU research publications [80]. Common measurements used to characterize Tx performance include the acoustic focusing gain (G), acoustic intensity level (L_I), intensity, negative pressure (p^-) and the mechanical index. This section will not focus on complete derivations regarding non-linear considerations, as they are not significant for the objective of the thesis.

Acoustic Intensity

Intensity values are directly dependent on density (ρ) and sound speed (c), while pressure (p) is not. When linear propagation is assumed, only the fundamental frequency is considered, and I can be described as:

$$I = \frac{p^2}{\rho_0 c_0} \quad (2.19)$$

where p is the pressure amplitude of fundamental wave, ρ_0 is the ambient density, and c_0 is the ambient sound speed.

Intensity measurements are often subdivided into categories such as spatial-peak temporal-peak intensity (I_{sptp}), spatial-peak temporal-average intensity (I_{spta}), spatial-peak pulse-average intensity (I_{sppa}), spatial-average temporal-average intensity (I_{sata}), and spatial-average pulse-average intensity (I_{sapa}) [81]. The subscript of these terms define time and space constraints to the measurements intensity, described in Tab. 2.2.

Table 2.2: Intensity measurement constraints

Name	Measurement Constraint
Spatial-peak (SP)	intensity at the location of maximum intensity
Spatial-average (SA)	average intensity of the focal area
Temporal-peak (TP)	measurement at the time of maximum pressure
Time-average (TA)	average over a specified period
Pulse-average (PA)	average over the pulse positive period

Slight differences occur in the definitions of I_{sptp} and I_{spta} due to different standards in definitions applied by governing authorities [81]. I_{spta} varies due to different standards in defining the focal area, which is further discussed in Sec. 2.6.1. I_{sppa} varies due to different standards in defining the pulse duration.

In continuous wave applications, pulse-average measurements are not considered, as is the case with this thesis.

The information revealed by intensity and pressure characterization differs depending on characteristics of the medium and the degree of non-linear propagation. When spacial variation of I_{spta} and I_{sppa} are minimal, or the medium is homogeneous, and linear propagation can be assumed, pressure and intensity gains can be equated as shown:

$$(2.20)$$

When spatial-peak temporal-peak pressure amplitude (p_{sptp}) is used in eq. (2.19), the I_{spta} is described as:

$$(2.21)$$

The intensity of the non-linear waveform can be represented by inclusion of the the harmonics [82]. By integrating the pressure waveform over an integer number of fundamental periods, an average pressure is attained. Thus, the same equation can represent both [83] and , depending on the time envelopes selected and waveform continuity. This intensity is described by the following equation:

$$\text{---} \quad \text{---} \quad (2.22)$$

where is the time varying pressure wave, is the carrier frequency of the pulsing envelope or continuous wave, is the integer number of cycles, and is the start time of period .

By considering the or over the area of the focal point, and are acquired respectively. is described as:

$$\text{-----} \quad (2.23)$$

Focusing Gain

can be described using intensity gain () or pressure gain () [6], [84]. This is described by the following equations:

$$(2.24a)$$

$$(2.24b)$$

where is the intensity at the focal point, is intensity at the surface of the source, is pressure at the focal point, and is the pressure at the surface of the source.

Secondary Lobe and Focal Area

For this thesis, a secondary lobe is a term used to describe a strong undesired pressure or intensity maxima that is not part of the main focal point. These secondary lobes can be composed of both grating lobes and side lobes [85]. Both types of lobes have different causes, however, they are similar in that both are undesirable. Grating lobes are related to the spacing and distribution of individual elements on the array, while side lobes are by the overall array geometry and are always present.

The criterion defining the acceptability of grating or side lobes varies [81]. In hyperthermia treatments, the relative magnitude of grating lobes may be judged differently than in high-power ablative therapies, as the risk of ablating surrounding tissue may be different.

In this thesis, the secondary lobes and steering range are defined at the acoustic intensity level boundary. If the intensity level boundary has a disconnected region, a side lobe is considered to exist.

2.6.2 Tissue Characterization

Soft tissue target volumes can be composed mostly of fat and muscle, making them relatively homogeneous in comparison to other HIFU targets. The space within the array curvature, between the array and the patient, is often filled with water or similar liquid. From Tab. 2.3, when compared to the properties of bone and air, low variability between water, fat, and muscle can be observed in both and .

The numbers presented in Tab. 2.3 are averages extracted by the IT'IS Foundation from multiple, primarily *in vivo*, studies [86]. The value of these tissue properties are still being investigated, and they can vary significantly from the values listed in Tab. 2.3.

Table 2.3: Average and approximate tissue properties related to HIFU [86]

Tissue	Density ()	Specific Heat	Thermal Conductivity	Sound speed ()	Attenuation coefficient ()	Power law exponent ()
Water	994	4178	0.6045	1482	0.02533	1.000
Skin	1109	3391	0.3722	1624	21.16	1.000
Muscle	1090	3421	0.4950	1588	7.109	1.083
Fat	911	2348	0.2115	1440	4.358	1.086
Cortical Bone	1908	1313	0.3200	3515	54.55	1.000
Air	1.16	1004	0.02738	343.0	0.03914	2.000

2.7 Ultrasound Time-Domain Simulation

Over the last few decades, advancements in computational power and HIFU medical applications has resulted in significant advancements in methods of ultrasound simulation. Simulation of acoustic and thermal affects of phased array Tx's is an integral part of their engineering. In the design phase, parameters must be swept such that a solution is found which results in sufficient performance for the application.

Simulations of the proposed Tx can also provide unique performance insight unavailable otherwise. Simulation can approximate how the ultrasound beam patterns and thermal responses will behave within a realistic volume. The human body is spatially heterogeneous in ways that significantly affect device performance for HIFU therapeutic applications. Among these effects is the resultant ultrasound refractions, reflections, and non-linearity. Uncompensated ultrasound refractions can decrease intensity gain and create undesired secondary pressure areas not normally observed in homogeneous mediums, such as those during hydrophone testing. The non-linear effects of ultrasound propagation have been shown to have significant relevance in ultrasound medical applications [87]–[89].

Finite element (FE), finite difference (FD), pseudospectral (PS), and integral equation (IE) methods are the most common methods applied for ultrasound simulation. The method should be selected based on application properties including the degree of heterogeneity, source geometry, frequency, and the relevance of non-linear ultrasound propagation.

The k-space PS method is a FD that improves on early FD methods correcting for phase-error caused by discretizations approximations, eliminating numerical dispersion in homogeneous mediums, and significantly reducing it in heterogeneous mediums [90]. FD methods of time-domain simulation replace the mathematical differentiation with discretized derivative approximations. Traditionally, FD methods apply these discretizations, and acquire solutions for each grid point. In the PS method, FD derivative approximations are solved for a finite sum of functions, rather than for each grid point. These functions are then applied globally over the grid. This effectively reduces the total number of points-per-wavelength (PPW) required for simulation.

In early HIFU phased array designs, methods of calculating the ultrasound field and its effects on biological tissue were applied using analytical methods. One of the first HIFU phased array devices, a cylindrical phased array design [48] proposed in 1988, was evaluated using the Rayleigh-Sommerfeld diffraction integral equation using the method of rectangular radiators. The heating effects were solved using a 3-dimensional bioheat equation using a finite difference method with successive over-relaxation.

2.7.1 Simulation Implementations

In 2014 [91], Verweij, Treeby, Dongen, *et al.* reviewed prominent implementations of methods used for ultrasound simulation. Tab. 2.4 lists some of the relevant software and methods described. FE simulation methods generally provide very flexible techniques to adapt to complex applications, however they are often much more computationally intensive than alternative methods for time-domain analysis [92].

The degrees of acoustic heterogeneity in localized volumes varies throughout the human body. These volumes allow for accurate k-space PS simulations with reasonably low points per wavelength. In [91] a k-space PS simulation was compared under similar conditions to the iterative nonlinear contrast source (INCS) FE method in a tissue-realistic heterogeneous volume. The results showed good agreement between both methods of simulation.

Many of the soft-tissue targets for MRgHIFU head and neck hyperthermia applications may be considered low enough in degree of heterogeneity for sufficiently accurate and time efficient k-wave pseudospectral simulation methods. In treatment volumes that are considered highly acoustically heterogeneous, such as in transcranial MRgHIFU therapies, FE simulation methods may yield more accurate results.

Table 2.4: Ultrasound Simulation Methods

Method	Type	Distinctions
Field II Software	IE	Homogeneous medium, linear ultrasound, linear attenuation.
FOCUS Software	IE	Homogeneous medium, linear ultrasound, linear attenuation, higher near-field accuracy than Field II, cannot compute pulse-echo signals.
Finite Difference	FD	Heterogeneous medium, linear ultrasound, potentially unstable, large phase error at Nyquist limit, unavoidable numerical dispersion.
Pseudospectral Time-Domain	PS	Heterogeneous medium, linear ultrasound, potentially unstable, exponential convergence, phase error eliminated at Nyquist limit, unavoidable numerical dispersion.
K-Space Pseudospectral	PS	Heterogeneous medium, nonlinear ultrasound, potentially unstable, exponential convergence, phase error eliminated at Nyquist limit, improved numerical dispersion in heterogeneous mediums, zero numerical dispersion in homogeneous mediums.
Split-Step and KZK	FE	Heterogeneous medium, non-linear ultrasound, potentially unstable, not bound by Nyquist criteria, requires directivity, reflections not considered, very low numerical dispersion in heterogeneous mediums without significant increase in points per wavelength.
INCS	FE	Heterogeneous medium, non-linear ultrasound, potentially unstable, very low numerical dispersion in heterogeneous mediums without significant increase in points per wavelength.

2.7.2 k-Wave Toolbox

k-Wave is an open source MATLAB toolbox providing tools for implementation of the k-space PS method [93]. It facilitates these acoustic time-domain simulation through a Matlab interface and optional c++ code integration.

Use of fast Fourier transforms (FFTs) to calculate spatial gradients results in waves reappearing on the opposite side of the computational grid [94]. To solve this problem the k-Wave toolbox utilizes perfectly matched layers at the boundaries of the computational grid to absorb waveforms that reach the edge, which mostly cancels the waves.

The k-Wave simulation code consists primarily of FFTs and element-wise matrix operations [94]. Up to 14 FFTs are executed at each time step. MATLAB executes code line-by-line and therefore limits how well operations can be combined for maximum computational efficiency. As such, a standalone C++11 code, part of the k-Wave toolbox, is utilized to increase GPU computational efficiency.

Domain Size

Memory usage and computational efficiency are key considerations for any 3D acoustic simulation. The advantage of parallel computing on a GPU can significantly increase computational speed, but present the challenge of limited memory. The FFT algorithms are also sensitive to grid sizes, with significant performance increases achieved using grid dimensions of prime numbers.

The perfectly matched layer occupies 10 grid points inside the edges for 3D simulations. As such, the sources and sensors should not be placed within these volumes around the edges of the grid.

The Courant-Friedrichs-Lewy number (CFL) specified by the user is used to discretize the time domain during simulations. If a solution does not converge, the CFL number should be decreased. By default, a CFL value of 0.3 is recommended, as it normally results in a good balance between accuracy and computational speed in weakly heterogeneous mediums [94].

The size of temporal discretisation (Δt) is computed [94] from the CFL number, spatial discretisation (Δx), and maximum sound speed under consideration (c_{max}) using eq. (2.25).

$$\Delta t = \frac{\Delta x}{c_{max} \cdot CFL} \quad (2.25)$$

For linear simulations in a homogeneous medium, a points-per-wavelength (PPW) of at least 2, which is the Nyquist limit, is required. However, other sources of error, such as those related to the discretizations of the physical domain and the perfectly matched layer, can result in additional error [95]. As such, at least 3 PPW are used for homogeneous mediums, and at least 4 PPW for heterogeneous mediums.

A higher number of PPW does however adversely affect the amount of memory required for computation. As the PPW increases, so does the total number of computational grid points (), which adversely affects memory and computational speed.

Chapter 3

Proposed System

This chapter discusses the proposed system integration, and its fabrication and implementation processes. An important objective in creating this system integration was to ensure the platform could be used and developed as an open-source project. In furtherance of this, the chapter focuses on the design process more than it does on any single final solution.

3.1 Proposed System Overview

The proposed system integrates the driving system for the phased array transducer directly within the magnetic resonance (MR) bore. This is accomplished using a recently proposed high efficiency quasi class-DE (qDE) driving method and a field-programmable gate array (FPGA) controller placed directly within the MR bore. A picture of the system integration is shown in Fig. 3.1, and a schematic of the layout is shown in Fig. 3.2.

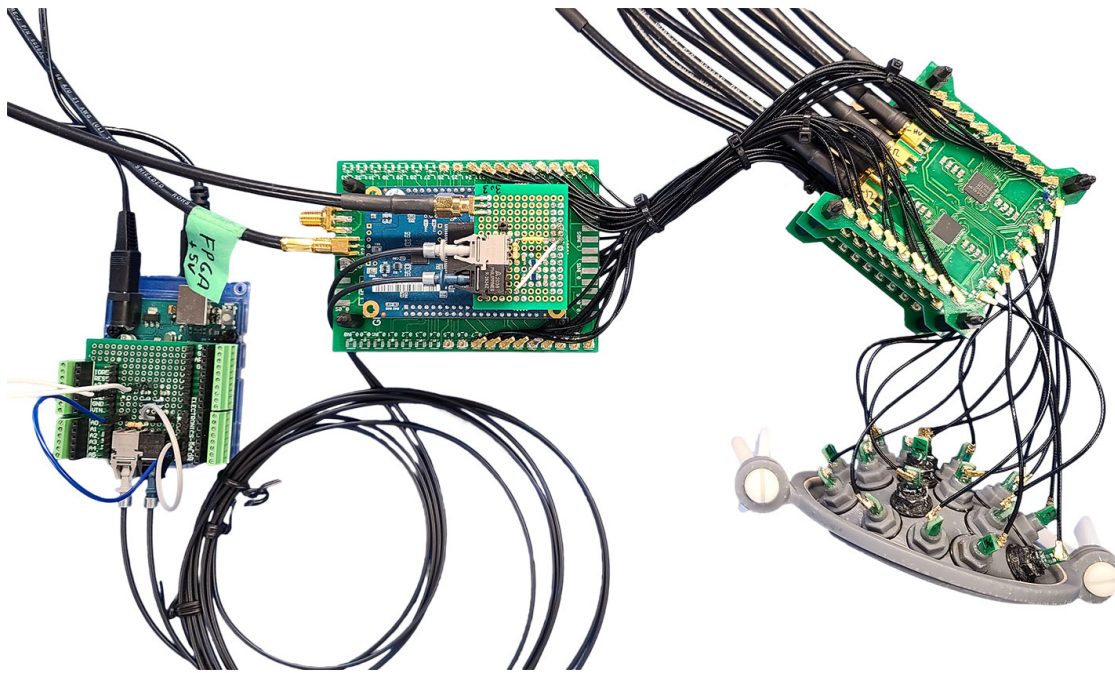


Figure 3.1: Components of proposed system that are placed within MR bore.

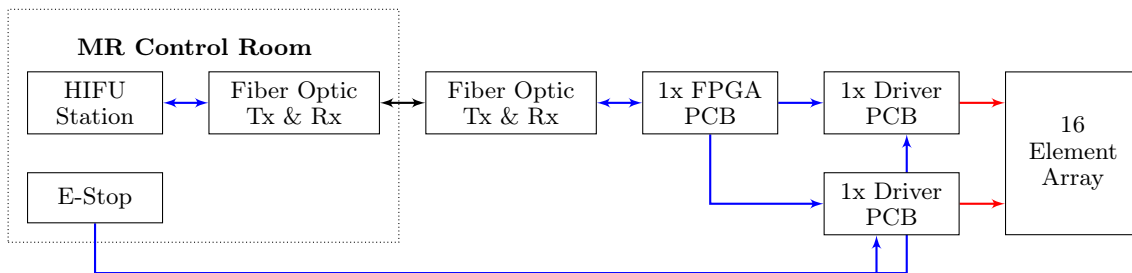


Figure 3.2: Example of system topology for a 16 Tx array.

The proposed system's driving system applies an MR compatible qDE driving method, and gating signal generation using a FPGA, directly within the MR bore. This removes the need for expensive and space consuming matching networks, which are normally positioned within the MR equipment room due to the ferromagnetic cores of their inductors. The portability, independence, and low-cost of this system may help streamline transitions from early design stages to MR testing, as the driving system remains paired with the transducer throughout development.

The array is produced using low cost 3D printed components. This allows for rapid production of various array designs, enabling the arrays to be built on a case-by-case basis. This allows array geometry and performance to be designed specifically for a target tumour size, depth, and nearby volume considerations. Small targets require less steering range, thereby reducing both the number of transducers (Tx) and overall size of the transducer. A small transducer better facilitates a conformal device; the transducer can be mounted directly on or in close proximity to the patient. A conformal device can better suit targeting challenging locations. If mounted directly on the patient, a conformal device may also reduce the amount of steering correction required, as the relative motion between the patient and the array are reduced during patient movement.

3.1.1 System Integration

The system integration is not reliant on partial incorporation into the MR scanner equipment room. The proposed system is shown in Fig. 3.3, and a more common layout for MRgHIFU systems is shown in Fig. 3.4.

The power required for the proposed hyperthermia array is significantly less than large transducers intended for tissue ablation. Small DC power supplies are run in isolation from a 120 V AC supply. The six power supply coaxial cables can be passed through the anaesthesia port fitted between most MR control and magnet rooms.

The high-intensity focused ultrasound (HIFU) planning station communicates power level and focal position to the FPGA through 3.3V GPIO ports. The small amount of data communicated to the FPGA allows for modular integration into most front-ends with as few as two communication cables. Optionally, the FPGA could be used to monitor skin and water temperature, or other metrics, and incorporate two way communication schemes to pass information from back to the HIFU control station.

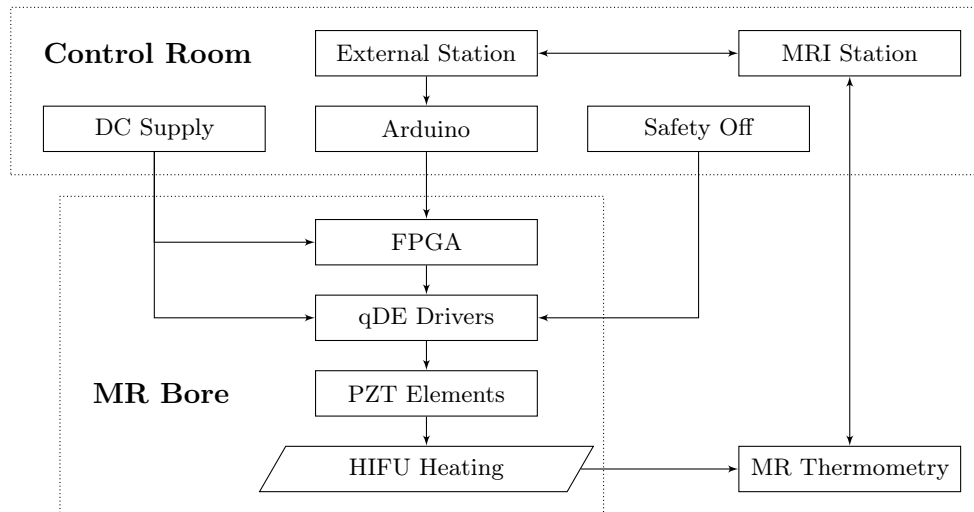


Figure 3.3: Proposed layout for MRgHIFU system integration.

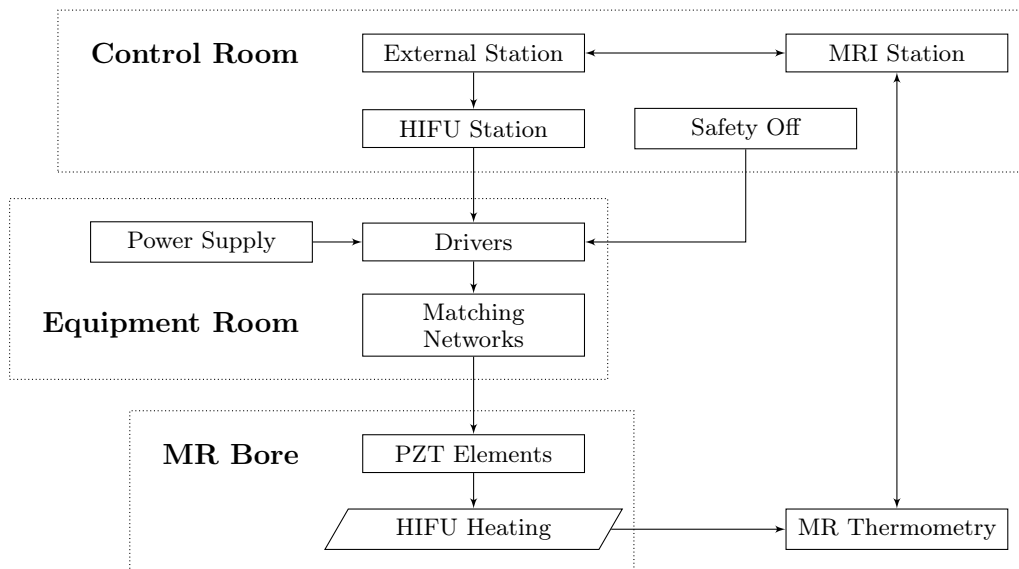


Figure 3.4: A layout often used in existing clinically approved MRgHIFU systems.

The FPGA generates the pulse-width modulation (PWM) signals for each Tx based on the desired steering position and power level. The PWM signals are sent to the nearby drivers, where the transducers are driven in qDE mode. A superseding 2 Hz PWM signal is used to regulate the power level, as the qDE solution does not account for PWM variations. A simplified layout of the driving signals path is shown in Fig. 3.5 for a 16 Tx array.

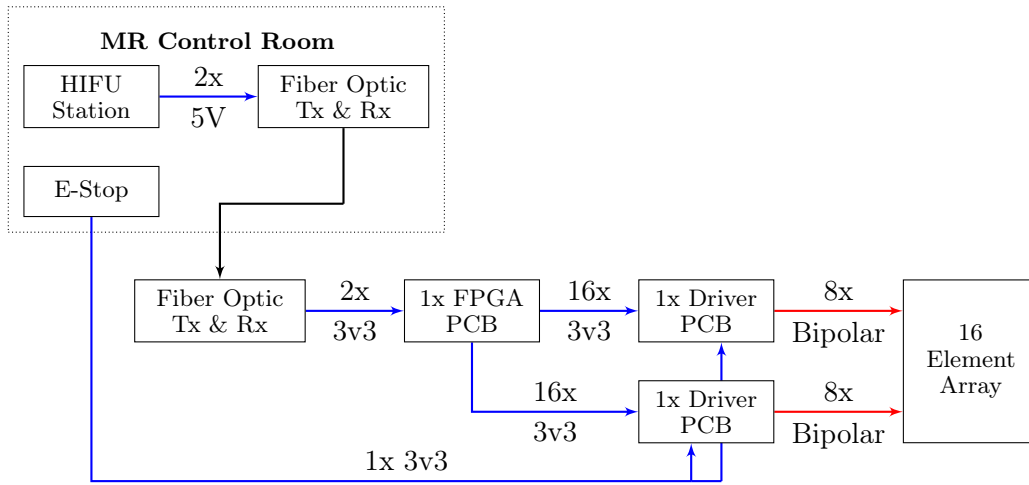


Figure 3.5: Signal flow overview, example of 16 Tx array.

3.1.2 Design Process

The design cycle of a MRgHIFU devices using the proposed system integration is described in Fig. 3.6. Piezoelectric (PZT) Txs are manufactured independently of the array. Reusing existing PZT Txs on new array shells provides a reduction in assembly time for case-by-case applications.

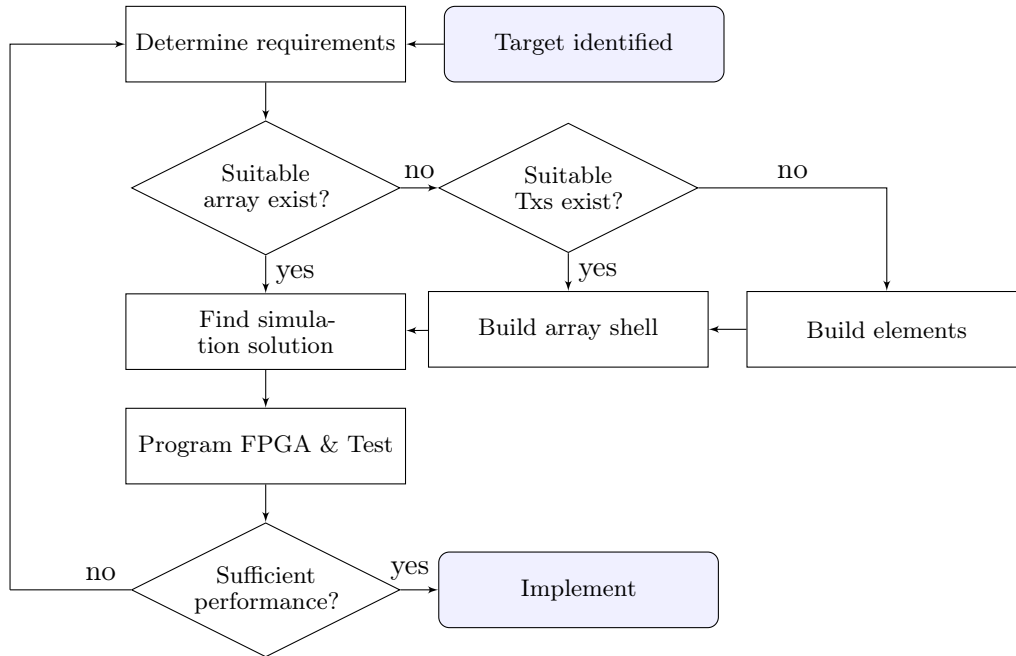


Figure 3.6: High-level design flow of proposed MRgHIFU modular platform.

3.2 Acoustic and Thermal Simulations

This section covers the basics of the MATLAB code developed to sequentially execute 3D acoustic simulations using the k-Wave toolbox. A series of functions generate array geometry and pseudo-random element positions for low-sparsity arrays that yield the required acoustic and thermal performance.

Potential solutions are simulated until one is found that yields no secondary lobes for all steering positions. A potential solution consists of a unique combination of array geometry size and pseudo-random Tx positions. The Tx positions are varied by increasing the seed number of the randomization function that is used to generate them. After every simulation, the 3D volume mapping the acoustic intensity is scanned for the presence of unwanted secondary intensity regions cause by the secondary lobes. If no disconnected intensity regions above θ_{max} are present, the solution is considered valid for only that steering position. Once all steering positions are proven valid for a particular solution, a fully valid solution is found. It can then be verified in thermal simulations. This process is illustrated in Fig. 3.7.

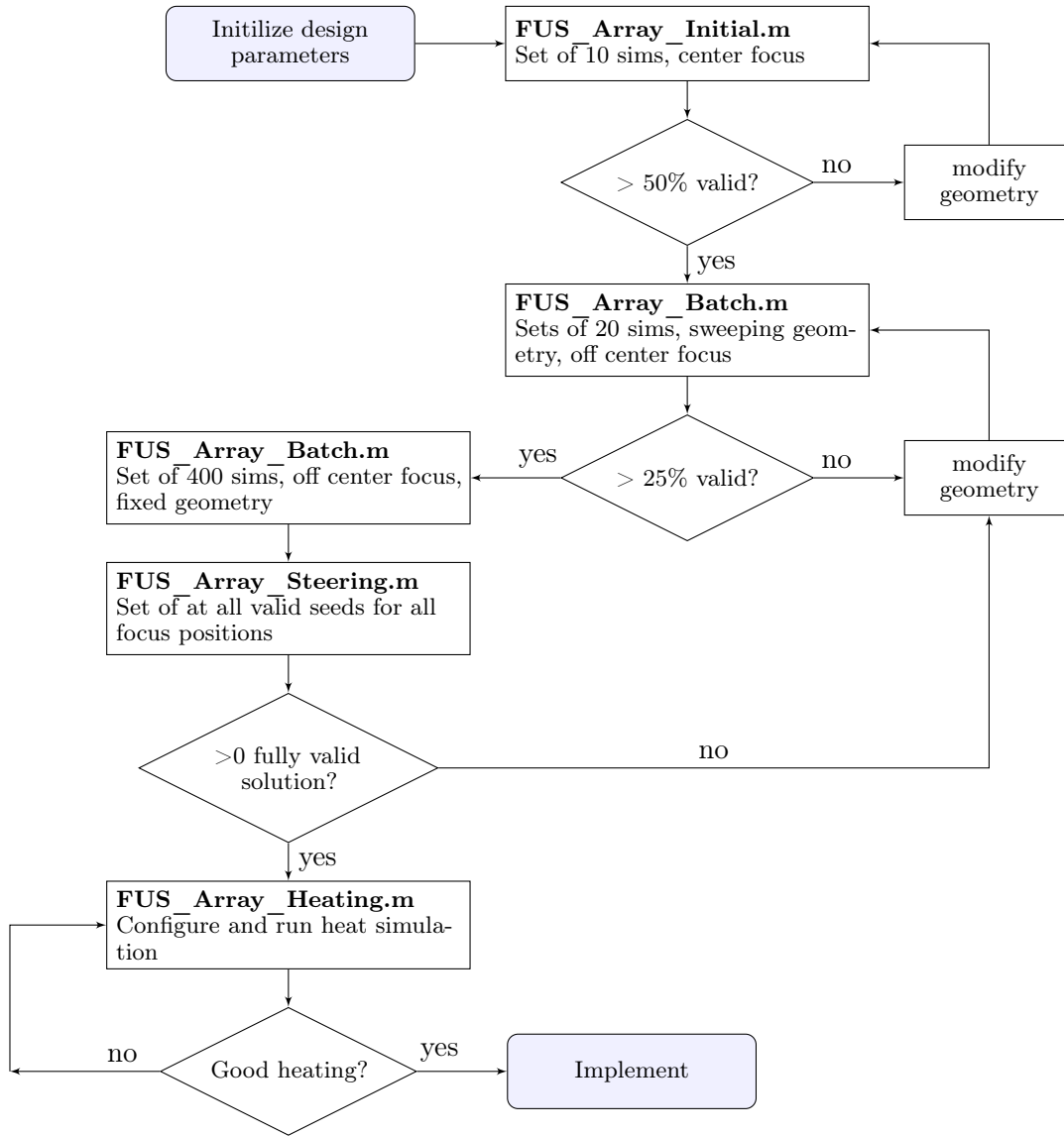


Figure 3.7: High-level flow of solution finding process using MATLAB functions.

Multiple simulations are run in sequence, then their results are compiled and characterized to gauge the performance of that particular array geometry. This is referred to as a "set" of simulations. Within a set, usually only the "seed" that generates the pseudo-random element positions are varied between simulations.

3.2.1 Acoustic Simulation: Initialization & Sequencing

The first function used, `FUS_Array_RUN_Initial.m`, handles running a single set of simulations for a single focal point during the initial design stages. The function is used to initialize basic array design variables, while more intricate parameters are defined in the function `FUS_Array.m`. The function returns the performance of the set and a list of seeds that were valid, meaning seeds in which no secondary lobes are present.

The second function, `FUS_Array_RUN_Batch.m`, handles running multiple sets of simulations, varying the array geometry between sets based on what was specified to be swept by the user. The function returns the performance of each set and a list of seeds that were valid for each set.

`FUS_Array_RUN_Steering.m` simulates all the required focal positions for each valid seed generated by `FUS_Array_RUN_Batch.m` or `FUS_Array_RUN_Initial.m`. No new seeds are found or generated with this function. In addition to sequencing and verifying the steering simulations, the function also exports the required Tx driving phase for each steering position for each seed. The Verilog files required for FPGA programming are generated directly from this function using the function `FUS_Array_Verilog.m`. If heating simulations are required, `FUS_Array_RUN_Steering.m` also saves the appropriate acoustic pressure recordings and variables for later use in `FUS_Array_RUN_Heating.m`.

3.2.2 Acoustic Simulation: Main Function

The `FUS_Array.m` function contains most of the core simulation functionality and additional initialization parameters. Each time `FUS_Array.m` is called an array is generated based on a specified random seed or random seed starting point. Using this generated array, a single 3D acoustic simulation is executed. The functions also generate plots to visualize the performance, and exports the Tx positions in Cartesian coordinates so the array can later be reconstructed in CAD software for 3D printing.

User Defined Parameters

The additional parameters must be defined by the user within this function normally remain fixed throughout the entire design process. For this thesis, the computational grid volume is segmented into 3 regions: 1) water, 2) skin, and 3) muscle/fat. The user selects which properties to consider in terms of homogeneous or heterogeneous considerations. If a homogeneous medium is considered, by default the medium is considered to be entirely water.

In most soft-tissue use cases, a weakly-heterogeneous medium is considered. As such, the Courant-Friedrichs-Lewy number (CFL) is set to 0.3 and the points-per-wavelength (PPW) is set to 4 in accordance with the justifications provided in Sec. 2.7. The minimum inter-element spacing is the effective Tx diameter in terms of physical space requirement. This considers casing or fabrication limitations when generating the Tx positions.

Space and Time Discretizations

The maximum voxel size of the simulated volume is determined by phased array driving frequency (), PPW, the minimum sound speed of the medium, and the thickness of the perfectly matched layer. To get the total number of computational grid points () for each dimension, the grid size in meters is divided by maximum voxel size. As the perfectly matched layer is by default 10 units thick, 20 grid points are added to each dimension and rounded to the next next integer. The computational grid is then optimized so the number of grid points in each dimension is a prime number, as explained in 2.7.2, and further detailed in Appendix B.

Increasing the total number of computational grid points () to a prime number requires either the PPW to increase and/or the total computational grid size in meters () to increase. The FUS_Array.m function was designed to increase both the PPW and actual computational volume. must be increased to compensate for the 20 unit perfectly matched layer, as explained in Sec. 2.7.2. However, too big of a volume is a waste of computational power, as volumes not of concern would be considered. To utilize the computational opportunity, the PPW number is also increased. The PPW number is recalculated based on the voxel size determined by the new and values.

The number of points per period (PPP) is calculated from the PPW and the CFL number. The time vector is generated using the maximum sound speed in the medium (), the CFL number, and the minimum voxel size () using .

The simulation time vector is given a total simulation period equal to the duration it takes a wave to travel from one corner of the grid to the geometrically opposite corner, plus 3 fundamental periods. Once a wave travels from one corner of the grid to the geometrically opposite corner, the system should be at or near a steady state. Three fundamental periods are recorded once the system has reached steady state.

Generating Tx Locations

The 3D grid must now be populated with a sensor mask that replicates Tx positions. The mask must also describe time varying signals for each voxel of each Tx to replicate the intended focusing and steering position. Each voxel belonging to a single Tx must have the same time signal; they cannot vary over the surface of a single element. The overview of the process is shown in Fig. 3.8.

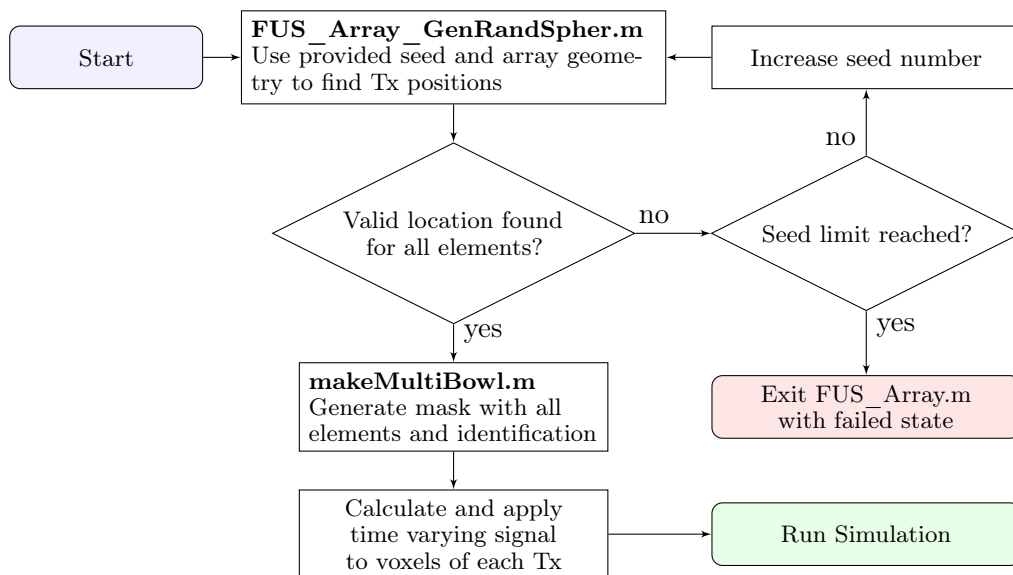


Figure 3.8: FUS_Array.m : flow of process for defining source mask.

The search of for valid Tx positions on the surface area of the array consists of repeatedly testing random seed values using function FUS_Array_GenRandSpherical.m until the function flags a seed that provides a valid position for each Tx. The function FUS_Array_GenRandSpherical.m is described in Sec. B.2 of Appendix B.

The voxels identified as part of the source mask now represent acoustic pressure sources. This is shown in Fig. 3.9, where the blue and red dots represent the focal point and geometric centre respectively. In this example, the array is steering 1.5mm off axis; the focal point is not at the geometric centre.

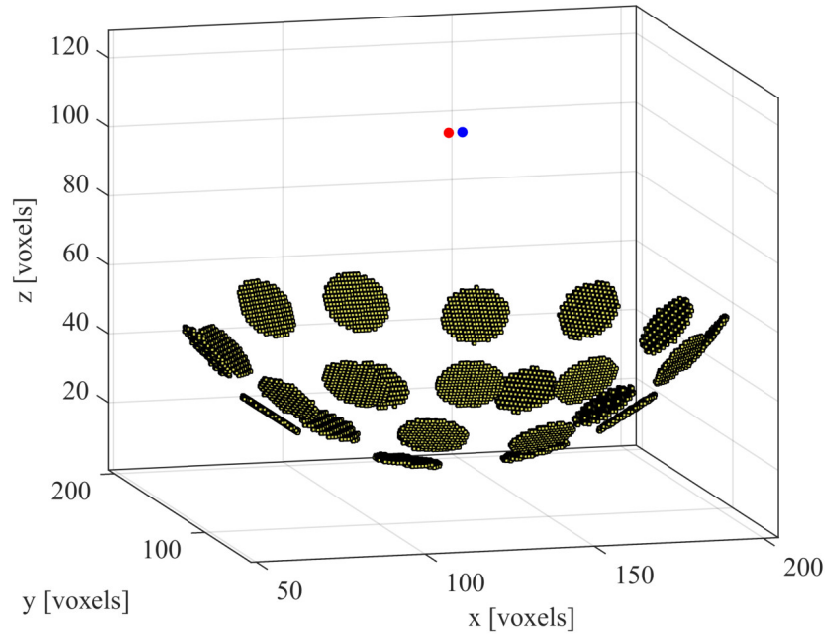


Figure 3.9: FUS_Array.m : Source mask in grid showing focal point (blue) and geometric centre (red).

Generating Tx Signals

The source pressure is calculated from the previously defined power of 1 Watt, the density and sound speed of the medium the array is located in, and the total surface area of the ceramics. The centre position locations for each Tx are generated using the function FUS_Array_GenRandSpherical.m, which returns the location of the grid points which represents the ceramic element.

If the array is not focused at its geometric centre, the electrical phase that must be applied to a Tx to steer the array is no longer zero. The phase is found by comparing the distance of a 0 phase reference signal to the distance between the centre of a Tx to the focal point. Based on the known wavelength, the difference in distance can be converted to a phase shift for the time varying signal. The phase is also stored for later use in verilog exporting. A cosine tapered up-ramp is applied at the beginning of the signal to minimize the effects of startup transients.

FUS_Array.m code can optionally read phases from an external file rather than calculating them. The functionality was added to gauge the effect of rounding the phases.

Running Simulation and Plotting Results

The entire 3D volume must be recorded so the search for secondary lobes can be executed outside of planar views. `kspaceFirstOrder3DG` calls the optimized C++11 GPU program to execute the acoustic simulation. Once the simulation is complete, the recorded maximum pressure is converted to intensity by taking into account the medium density and sound 3D grids, accounting for potential variations. Taking the maximum intensity value in the volume results provides the spatial-peak temporal-peak intensity () value. The medium's intensity is then normalized to this value.

The secondary lobe intensity level of -6 dB is converted from dB to linear and the volume is searched for disconnected regions around this linear secondary lobe boundary.

3.2.3 Heating Simulations

Once a solution is chosen based on its normalized intensity performance, the thermal effects for the proposed treatment should be observed. This is accomplished using the function `FUS_Array_RUN_Heating.m`, which applies the k-wave function `kWaveDiffusion.m` in logical sequence to control the heating.

The recorded pressure waves from each steering position's acoustic simulation are converted to the volumetric rate of heat deposition in . This is accomplished by extracting the phase and amplitude of the pressure throughout the volume, then making the appropriate versions based on the properties of the medium. This process is further detailed in Appendix B.

The acoustic power of the array must be considered for the heating simulations. As the acoustic simulations were executed for 1 Watt, to consider an array capable of delivering 12 W of acoustic power, the volume rate of heat deposition is simply multiplied by 12.

Heterogeneous properties of the mediums will be considered for the heating simulations, therefore the spacial variance of the medium properties are considered. Heterogeneous simulations are considered for this thesis. In addition to the medium's spatially variant thermal properties specified in FUS_Array.m, a blood perfusion coefficient of 0.01 1/s in the fat / muscle tissue volume was considered.

Heating Pattern and Control

The heating pattern used for testing was set to maximize the size of the heating volume by switching steering positions every 0.5 seconds in a repeating sequence. A period of 0.5 seconds was chosen somewhat arbitrarily, but it is reasonable in its effects as it ensures transients are unlikely to affect the qDE driving results, and provides sufficient heating simulation results.

The time domain was discretized to step sizes of 0.1 seconds for the simulations. The 0.5 second period for each focus position is segmented into two sections; "on" and "off". For the "off" period, the volumetric rate of heat deposition is set to zero, simulating an array with no power. Discrete temperature measurements are considered by updating the temperature measurements used for the proportional integral derivative (PID) control every 3 seconds.

The relative length of the "on" and "off" periods within the 0.5 second period is described by a PWM duty. It is determined by a PID control algorithm based on the temperature of each focal point location. To mimic the functionality of MR thermometry, the temperature feedback is discrete; measured every 3 seconds.

3.3 Array Shell and Transducer Fabrication

The array shell and PZT ceramic casings are 3D printed with both fused deposition modeling (FDM) polycarbonate and stereolithography (SLA) resin. For both the transducer casings and the array body, SLA produced superior results. The locations of the Txs are exported to an excel file by the MATLAB script `FUS_Array_RUN_Steering.m`. That file is imported into Autodesk Inventor to model the array geometry exactly as simulated. A picture of the assembled PZT Tx array is shown in Fig. 3.10.



Figure 3.10: Picture of assembled array shell and Txs.

3.3.1 Transducer Casing

The Tx casing was designed to screw into the array to create modularity in the system; the same tuned Txs can easily be re-used in various array bodies. The Txs are air-backed but the array can be fully submerged as the air is contained within the casing. To assist in assembly, a recess was created for the piezoelectric ceramic to sit in, centering it so the sides can be sealed with an even distribution of silicone. The remainder of the ceramic's side is not tight and has sufficient space for silicone to seal the ceramic to the casing without clamping. The casings were printed and testing with both FDM polycarbonate and SLA resin, shown in black and grey respectively in each Fig. 3.11.



Figure 3.11: Picture of Tx casings, where the black casings on the far left and right are polycarbonate.

A small amount solder paste was used to solder the stripped micro-coax to the ceramic. Once the wire is soldered onto the the ceramic, it is placed inside the casing and sealed using silicone. To keep the ceramics from floating during assembly, they are held in place by tensioning screws. This is shown in Fig. 3.12.

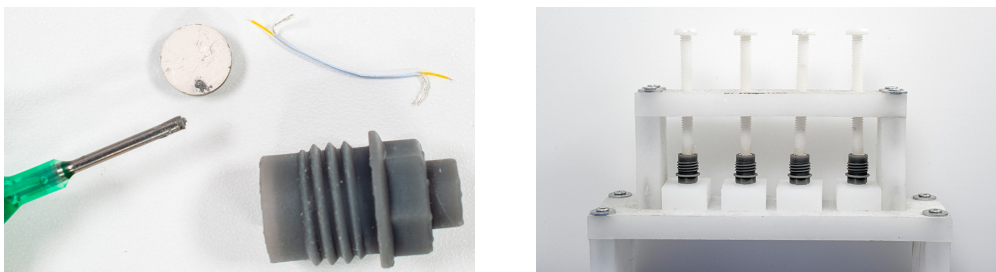


Figure 3.12: Tx casing assembly process.

Once the silicone is dry, the process is repeated for the mini printed circuit board (PCB) that holds the U.FL connector and capacitor pads, as shown in Fig. 3.13. The added parallel capacitors are required for qDE power balancing. Silicone is again used to seal the PCB into the end of the casing. Fig. 3.13 shows a Tx with an o-ring and U.FL cable assembly attached.



Figure 3.13: Picture of PCB mounted in casing.

An o-ring is added to better seal the inner and outer sides of the array, which are normally water and air backed respectively. Additionally, the O-ring allows for minor depth adjustments and applies a consistent force to the threads to prevent the Tx's from loosening during operation. A picture of the array holding water is shown in Fig. 3.14



Figure 3.14: Picture of assembled array shell and Tx's.

3.3.2 Array Shell

The array shell was also printed in both FDM polycarbonate and SLA resin, however the polycarbonate print required significant post processing. The SLA and the FDM arrays are shown in Fig. 3.15.

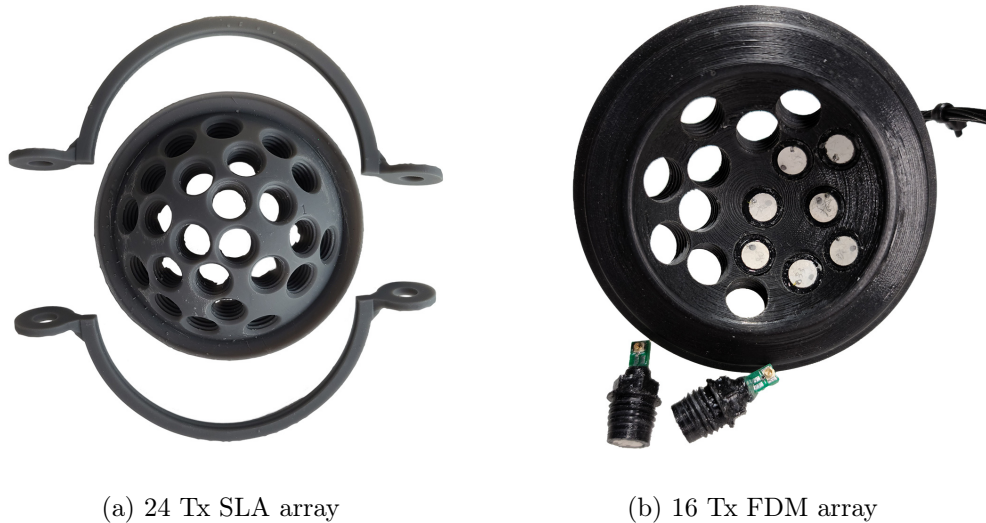


Figure 3.15: Picture of array shells.

Support structures are required when printing the FDM polycarbonate array. These support structures tend to bond to the polycarbonate due to its high printing temperature. As a result, the threaded holes cannot be printed directly in the array with FDM polycarbonate, and must be drilled and tapped using additional equipment after printing. A picture of the FDM printed polycarbonate shell before post-processing is shown in Fig. 3.16.



Figure 3.16: Picture of FDM printed polycarbonate shell before post-processing.

3.4 Quasi Class-DE Power Balancing

After the Tx's are fabricated, they must be binned and tuned for qDE driving. Binning is the process of selectively removing some of the manufactured Tx's based on their parameter or performance variance. To drive the array in qDE mode, the techniques outlined in Sec. 2.5 are applied using a series of python scripts. The use of these techniques balances the acoustic power delivered from across all Tx's at a common frequency. A flow chart of the qDE solution finding process is shown in Fig. 3.17.

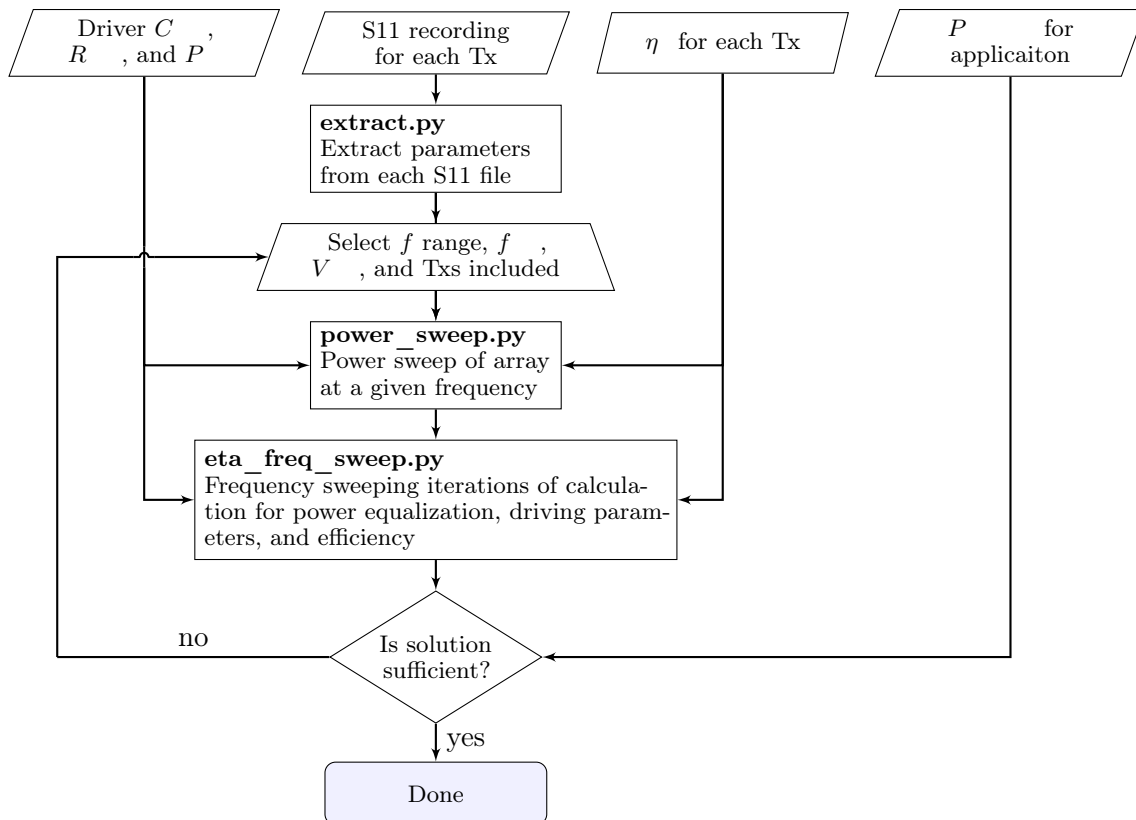


Figure 3.17: Python script qDE solution solving process.

The Tx equivalent parameters can be extracted by a single parameter touchstone file (s1p) for each Tx. The s1p files are generated by measuring and recording the S11 waveforms across the resonant frequency of interest using a vector network analyzer (VNA). Once each Tx is electrically characterized, they are selectively removed (binned) until the required overall array electrical efficiency (η), V , and number of Tx are met.

3.4.1 Transducer Electrical Characterization

Measurements of a Tx are taken while it is affixed to a jig to hold it in deionized water. Acoustic absorbing material placed at the bottom and sides of the containment vessel. Each Tx is tested for leaks by fully submerging it for more than 5 minutes. If the S_{11} response noticeably changes after 5 minutes, and temperature changes are not suspected, then a leak is assumed. The testing setup using a NanoVNA-F is shown in Fig. 3.18.

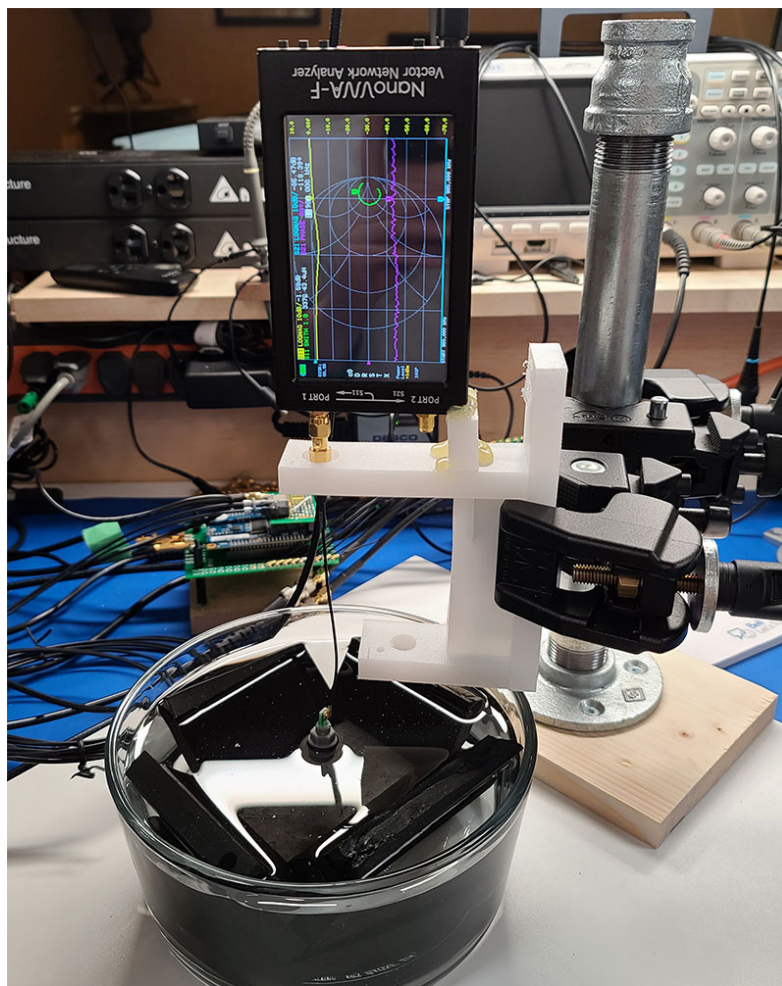


Figure 3.18: NanoVNA-F measurement setup

The python script `extract.py` is responsible for extracting the Tx parameters to create the equivalent electrical circuit. The method and equations used to extract the equivalent parameters are detailed in Sec. 2.4.1. The values of series-resonant frequency (), parallel-resonant frequency () and impedance of series resonant branch () are extracted to calculate the equivalent circuit component values.

3.4.2 Transducer Acoustic Conversion Efficiency

The acoustic conversion efficiency was measured by a radiation force method in accordance with the methodology presented in Sec. 2.4.2. The resonant frequency of interest was determined from the S11 plot. The efficiency was measured multiple times and the mean was taken to reduce the error on the scale readings due to varying air pressure changes in the room. The testing setup is shown in Fig. 3.19.



(a) on scale with Tx inside



(b) dissolved oxygen testing

Figure 3.19: Picture of measurement processes.

If the variance between Txs is very low, the process of measuring the for each Tx can be skipped, however this is discouraged as comparing values could identify a faulty Txs.

3.4.3 Calculating qDE Driving Parameters

Once the mechanical and electrical characteristics of each Tx are characterized, the process of binning the Tx's begins. The process of binning is further explained through demonstration in Sec. 4.2.

The minimum P_{min} should be known prior to binning to ensure that the array can deliver sufficient power to the focal point, and to select the appropriate value of P_{min} . The methodology for verifying P_{min} using heating simulations is introduced in Sec. 3.2.3.

The python code from [96] was modified to more quickly apply consecutive sweeps for transducer groupings and design parameters. The process consists of 3 feedback options to decide which Tx's to remove. Plotting the S11 parameters, sweeping the frequency and observing the array performance, and sweeping the power level at a fixed frequency and observing the performance.

power_sweep.py - Sweeping Power

The `power_sweep.py` script sweeps for a qDE solution to each Tx for a fixed frequency using the methods outlined in Sec. 2.5. The adjustable external capacitance (C_{ext}) is varied between its minimum and maximum value to regulate power, and the result for each Tx is plotted. As this script does not require a valid qDE solution to plot, it can be used to bin Tx's before a valid qDE solution is found.

eta_freq_sweep.py - Sweeping Frequency

The `eta_freq_sweep.py` script finds the array performance by attempting to find a valid qDE solution to the selected Tx's grouping for a range of frequencies. The methodology for finding a qDE solution is outlined in Sec. 2.5. If a solution is found, the overall array electrical efficiency (η) is plotted as a function of frequency. `eta_freq_sweep.py` prints relevant design parameters, such as the duty (D), ratio of voltage difference (V_{ratio}), and adjustable external capacitance (C_{ext}), for each Tx at each frequency step.

3.5 Driver Printed Circuit Board & Power Supply

The qDE driving system integration proposed transmits both power and signals to components within the MR bore through coaxial cables. The HIFU station in the MR control room, connected to an Arduino, sends sonication control information through optical isolation to the FPGA. Based on the received information and preprogrammed duty cycles and phases, the FPGA generates PWM signals for each Tx of the array. The 3.3V (3v3) PWM signals are sent through coaxial cable to the commercial driver PCBs. The higher-voltage bipolar PWM signals from the output of drivers are sent to each Tx through coaxial cables.

3.5.1 Driver Printed Circuit Board

A 4-channel commercial digital pulser integrated circuit (IC) is used to amplify the PWM signals generated by the FPGA. A 2-layer PCB was designed and assembled to hold two of these drivers. The MAX4940 can drive up to four PZT TxS each, requiring two input PWM signals per channel. Two pulsers were affixed per PCB, meaning each board can drive 8 TxS. Pictures of the initial prototype (v1) for an assembled driver PCB is shown in Fig. 3.20. The electrolytic caps shown in Fig. 3.20 were later removed as they contained ferromagnetic material. An electrical schematic of the second version (v2) is shown in Appendix D.

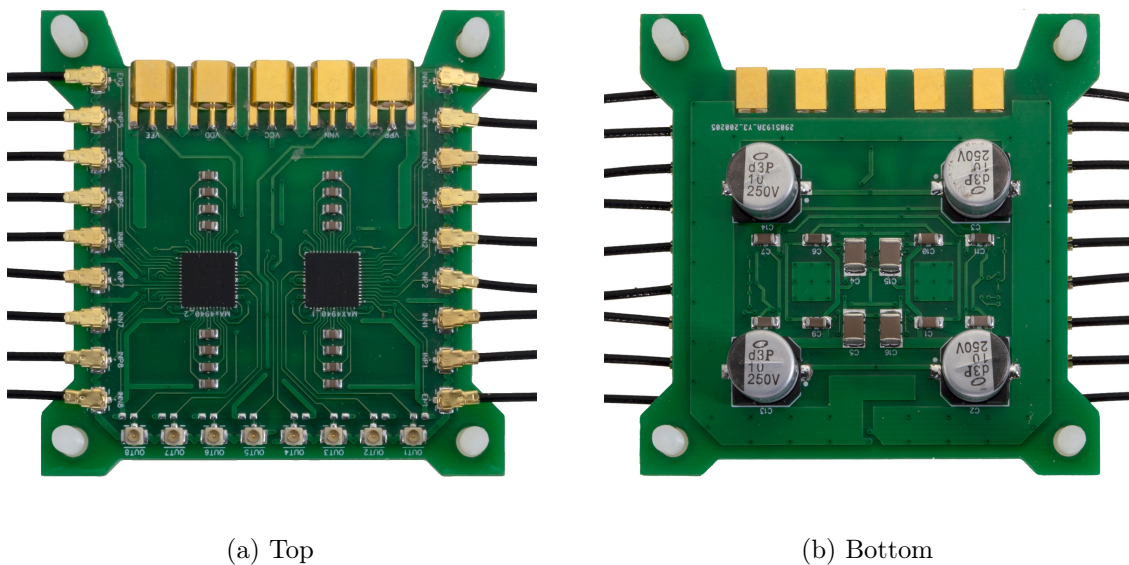


Figure 3.20: Pictures of assembled driver PCB v1, 70 mm x 70 mm.

The prototype was later re-designed with a 4-layer board to increase the MR compatibility by (1) reducing the size of the ground loops that form between the U.FL coaxial cables due to distance between U.FL receptacles, (2) reducing the trace length of both low and high voltage signals, and (3) reducing the overall footprint. The active area of the PCB was reduced by 51 %. The enable signal for E-Stop was disconnected from the FPGA and is communicated through an SMA connector. A probing port was added to output 8 using an SMA connector for signal troubleshooting when the board is in the MR bore. An image of the redesigned board's top and bottom layers are shown in Fig. 3.21. A 3D model of the redesign is shown in Fig. 3.22.

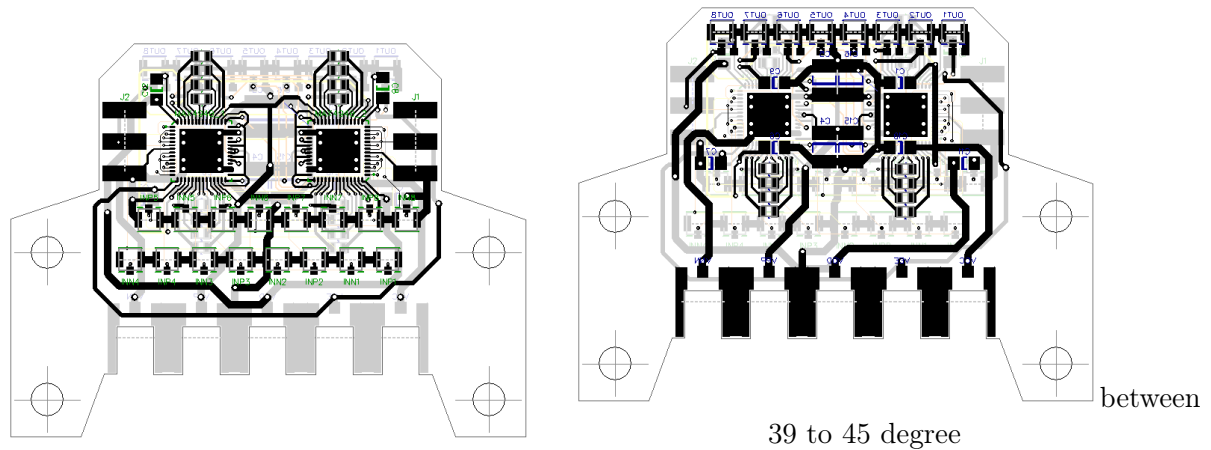


Figure 3.21: Driver PCB v2 trace layout, 70 mm x 50 mm.

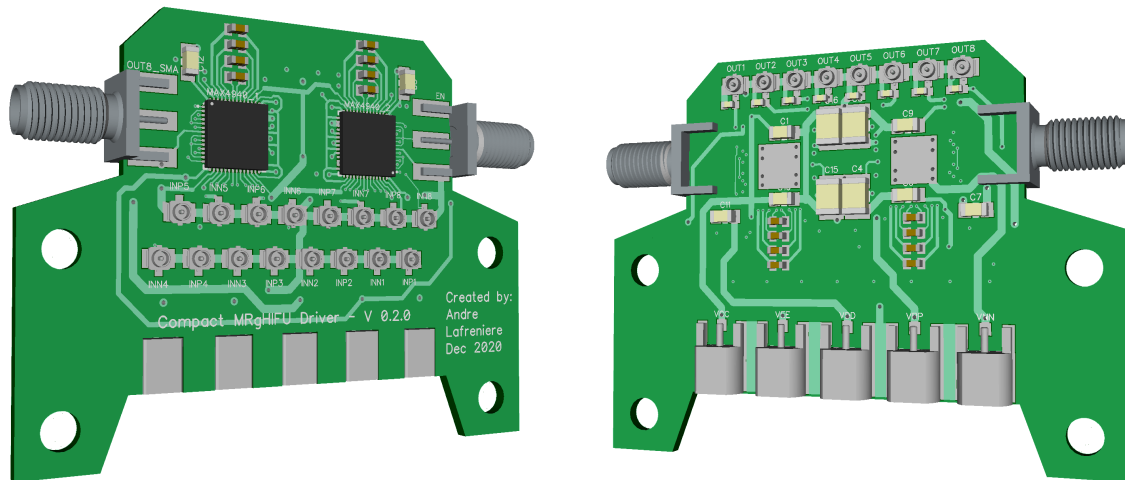


Figure 3.22: Driver PCB v2 3D preview, 70 mm x 50 mm.

To increase MR compatibility, only components with little to no listed ferromagnetic materials were used. The most relevant components and their relevant characteristics are listed in Tab. 3.1. U.FL connector coaxial cable assemblies are used to connect the PWM input to the driver PCB and the amplified PWM signal to each PZT Tx. RG58A coaxial cables and MCX connectors deliver DC power to the driver PCB at five voltages.

Table 3.1: Driver PCB components.

Type	Product	Description
Driver	MAX4940	<ul style="list-style-type: none"> • quad channel • up to bipolar output • PWM input • independent enable input • integrated active clamps and blocking diodes • very low concentration of ferromagnetic material iron ()
Coax Cable for Power	9058AC BK005	<ul style="list-style-type: none"> • RG58A coaxial with copper braid shield • 19 strand / copper(tinned) conductor
MCX Socket	0734151061	<ul style="list-style-type: none"> • brass body, gold finish
Coax Cable for Signal	252180	<ul style="list-style-type: none"> • U.FL coaxial assemblies with female sockets • 7 strand / conductor • diameter, and long • silver-plated copper braid conductor & shield
U.FL Jack	1909763-1	<ul style="list-style-type: none"> • copper alloy body, copper alloy contact, gold finishes

3.5.2 Driver Board Assembly

The PCB boards were assembled using an electropolished stencil and solder paste. To ensure the stencil remained fixed and flat during assembly, all components were temporarily glued to the work bench. Extra PCB boards were hot-glued to a table around driver board to level the surface to the thickness of the driver board. This process is shown in Fig. 3.23.

A re-flow oven was not available at the time of production therefore heat was applied using an infra-red board heater and heat gun. The 56-TQFN package of the MAX4940 was challenging to assemble and solder due to insufficient PCB quality on the initial prototype. The initial prototype shown in Fig. 3.21 was not ordered with precision manufacturing, used a FR4-Standard Tg 130-140



Figure 3.23: Positioning stencil for solder paste on driver PCB.

board, and used a HASL lead finish. The boards were ordered from the manufacturer JLCPCB. To be more compatible with the 56-TQFN package, the board should have been ordered as a FR-4 Tg 155 board, an ENIG-RoHS surface finish, and higher precision manufacturing to reduce soldering faults. As a result of the low quality PCB ordered, the pins were inspected prior to testing.

Another issue with the v1 design was that the through holes below the pad of the MAX4940 were not wide enough to allow for good solder flow between sides of the board. As a result, getting the correct amount of solder on the centre pad such that the driver sits flush on the board is challenging. This issue compounded with problems caused by the soldering methods used, which resulted in inconsistent heat distribution. A picture of a soldered driver with too much solder on the centre pad is shown in Fig. 3.24.

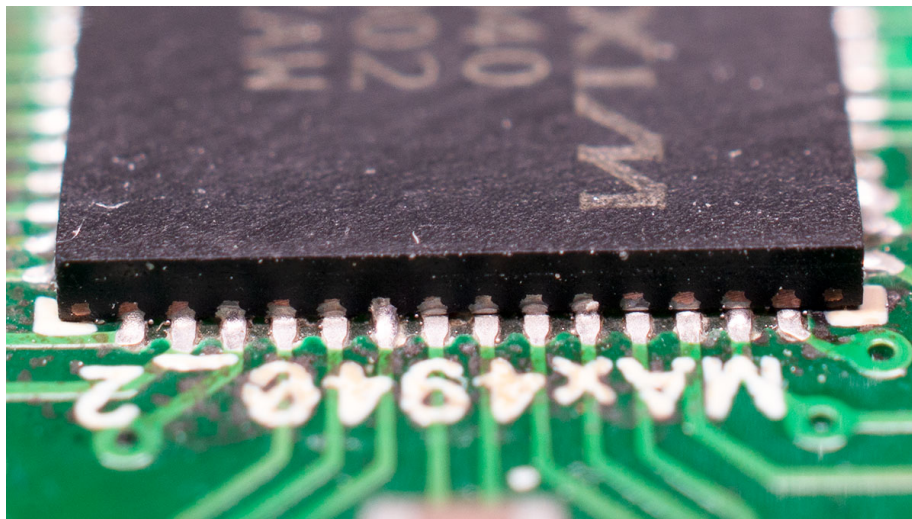


Figure 3.24: Picture of an improperly soldered MAX4940 driver.

3.5.3 Power Delivery

Power is delivered from the MR control room to the FPGA and driver PCBs within the MR bore through RG58A coaxial cables. Independently isolated and floating AC/DC converters allow the system to be tied to ground at a single point in the MR bore. This allows the coaxial cables providing power to be balanced, removes ground loops in the supply lines, and safeguards against any voltage difference between the patient and equipment. The Arduino / HIFU Station communicate to the FPGA through fibre optic cables. This provides electrical isolation and prevents electromagnetic interference in the signal path between the MR bore and the MR control room. A diagram of the power delivery and electrical connections are shown in Fig. 3.25.

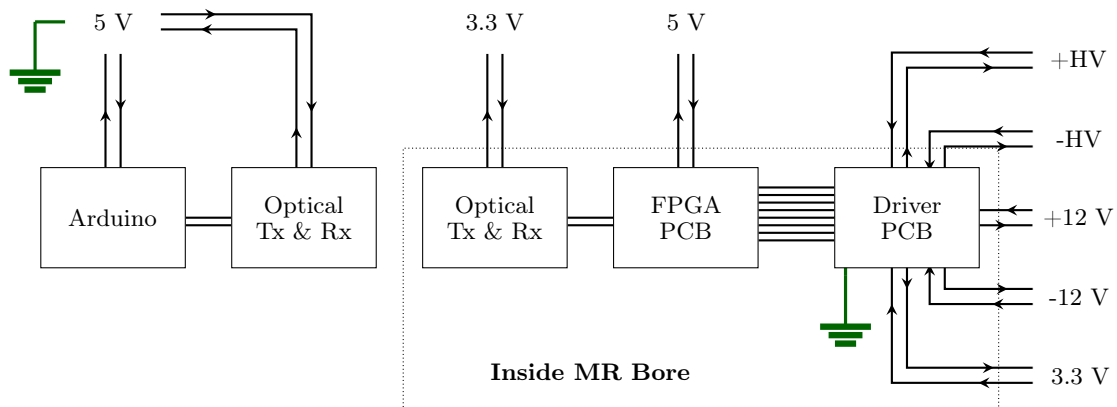


Figure 3.25: Power distribution to system components, example of 8 Tx array.

Fig. 3.25 shows all electrical connections, including the micro-coaxial cables connecting the FPGA to the driver PCB. Ground loops do exist between these parallel cables, and they should be as short as possible to ensure the low-voltage PWM signals are not affected by large changes in the magnetic field. Another problem with these numerous parallel connectors is that they are no longer balanced; the shielding of all connectors of a driver PCB are attached in parallel. Ideally the drivers should be placed directly on the FPGA breakout board to reduce the trace length of these low-voltage signals.

Commercial AC/DC converter enclosures were used to supply , , , and . They were placed within a computer power supply enclosure. Two external linear DC supplies were used to provide the higher voltage DC (+HV & -HV). A picture of the power supply assembly without independent isolation transformers is shown in Fig. 3.26.

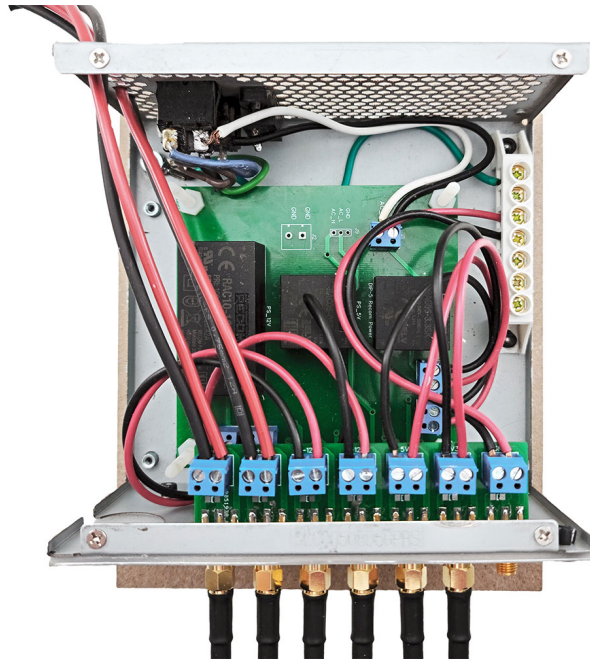


Figure 3.26: Power supply assembly

The power supply depicted in Fig. 3.26 was designed and used during initial testing but was eventually discontinued in favour of linear power supplies with good current limited capabilities, which helped prevent burnt chips during troubleshooting. Individual isolation transformers should also be added to the AC side of the power supplies shown in Fig. 3.26 to ensure independent isolation. Inline filters should also be added on each DC power supply line to filter noise from the switching power supplies, but this requirement has not been established through testing.

3.6 FPGA Controller

An FPGA was used to generate PWM signals for the qDE driving circuits. The PWM signals were shaped based on the desired focal point position and power level. Parameters stored within the FPGA prescribe the phase signal and duty cycle for each element and steering position. An FPGA was used due to its potential for numerous PWM signals, as each element requires at least two PWM channels for qDE driving.

A DE0-Nano Cyclone IV development board was selected as the prototype's FPGA. It is a relatively inexpensive board that meets all the requirements of the prototype while maintaining good usability. The most notable features of the DE0-Nano are the 72 programmable general-purpose input/output (GPIO) pins, the onboard re-programmable flash memory FPGA serial configuration device (EPCS), and up to 4 phase-locked loops (PLLs) running from a 50 MHz oscillator.

3.6.1 Printed Circuit Board

The DE0-Nano is mounted to a breakout PCB, as shown in figure Fig. 3.27. The FPGA is connected by the two 40 pin GPIO headers. The double sided board provides the 5 V power supply for the FPGA and links the GPIO pins to 72 U.FL connectors. Some of the GPIO pins are also connected to SMA connectors for the purpose of providing probing points through RG-58 coaxial cable for troubleshooting.

The optical transmitter and receiver used for communication to the Arduino controller are connected to the 3rd GPIO header on the other side of the DE0-Nano. The optical communication breakout board shown in Fig. 3.27 is an early prototype version not intended for MR environment use.

Despite the power supplies being routed to avoid ground loops in the MR environment, unfortunately it was not possible to avoid ground loops between the numerous micro coaxial cables connecting the driver PCBs to the FPGA PCB. As such, care should be taken in their routing to avoid large loops between each other.

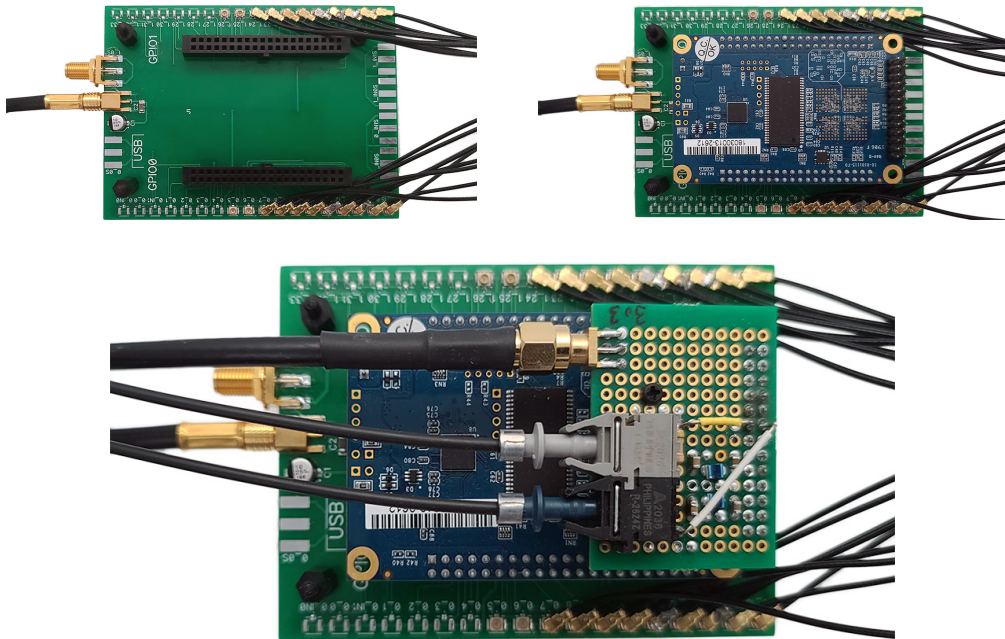


Figure 3.27: Picture of FPGA PCB with optical transducer board attached.

3.6.2 MATLAB Verilog Export

The FPGA logic is written in the verilog hardware description language. Once the MATLAB steering simulations are complete, the function `FUS_Array_RUN_Steering.m` generates the required verilog files for FPGA implementation with the exception of the top module using the function `FUS_Array_Verilog.m`. A file is generated for each Tx which contain the phase for each steering position, translated to the equivalent integer period.

Within the FPGA, a counter is used generate the driving frequency by counting each rising edge of the FPGA's PLL clock. The total count required to equal to one period of is referred to as `TTOTAL`. The PLL implementation is further discussed in Sec. 3.6.4. A verilog file is also generated for the `Main_Module.v`, adapting to the number of Tx's required on the array.

3.6.3 Verilog Code and Program Structure

Top Module

A top module is used to translate or generate the signals required for the main function. When programming the FPGA, this is where the physical signals of the device are assigned to the ports of the main module, Main_Module.v. The FPGA top module for this system also implements hardware specific modules to blink LEDs and create high-frequency clock signals using the FPGA’s PLL. This was not included in the main-module as it is more hardware dependent and not needed for simulation. A top-level view of the program is shown in the registry-transfer diagram of Fig. 3.28.

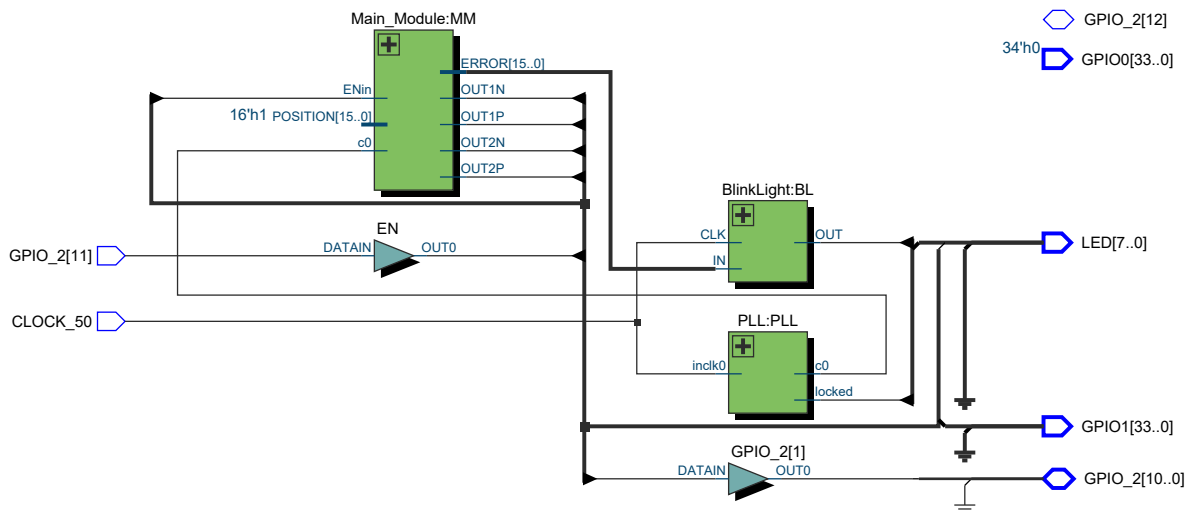


Figure 3.28: Register-transfer level diagram for an array with 2 Tx.

The diagram in Fig. 3.28 does not include the communication component for steering the array through optical transceivers, which is still in development. As such, the variable for controlling the steering position was not associated with any GPIO pins, and the steering position is selected when programming the array.

Main Module

The main module calls two different types of modules for each Tx and an imaginary reference Tx. The imaginary Tx, numerated zero, generates a zero phase reference signal for troubleshooting, and the transducer0.v file generated in MATLAB stores the value of TTOTAL. A registry transfer diagram showing the data-flow for an array of two Tx is shown in Fig. 3.29.

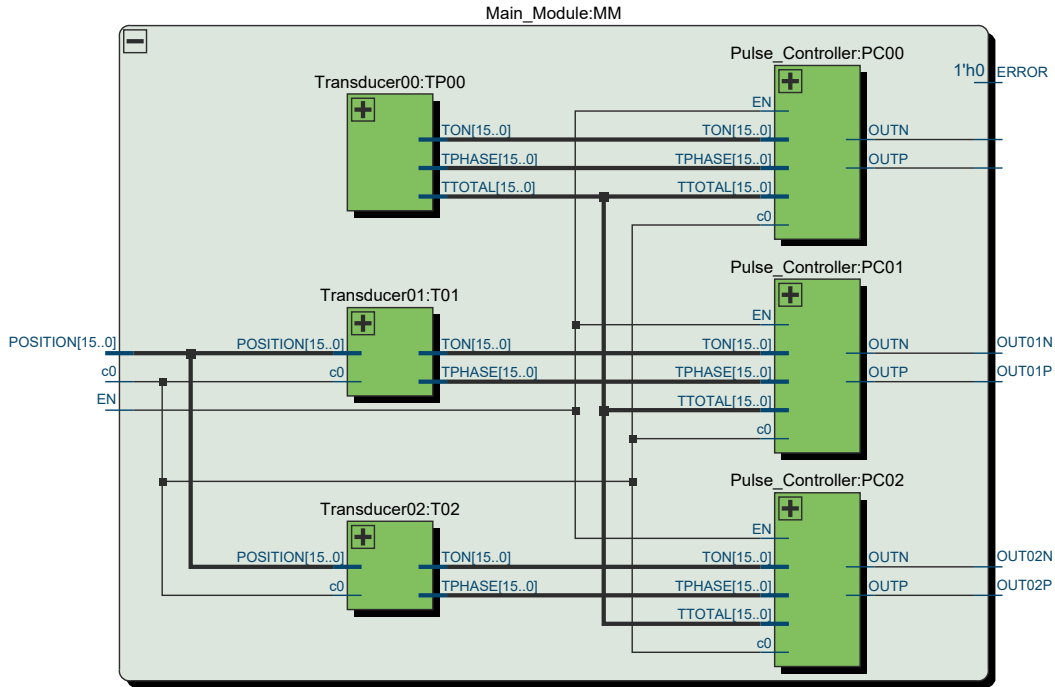


Figure 3.29: Register-transfer level diagram for an array with 2 Tx.

Transducer Data

The first module called within the main module is a Tx verilog file generated in MATLAB. An example of this module is shown in Fig. 3.30. The phase applied to a Tx phase is determined by the sum of the phase from the steering position and the phase from the qDE power balancing algorithm. The duty cycle is a result of only the power balancing algorithm. Both variables are dependent on the qDE simulations and must be entered manually by the user in each transducer file.

```

module Transducer1(
    input wire [15:0] POSITION, // Foc posn
    input wire c0, // Clock
    output wire [15:0] TON, // Phase of PWM
    output wire [15:0] TPHASE // Duty of PWM
);
// === Internal REG/WIRE Declarations ===
reg [15:0] PHASE_POWER =16'd0; // Phase from qDE
reg [15:0] PHASE_STEER;
//===== Structural Coding =====
assign TON =16'd0; // Duty from qDE
assign PHASE =PHASE_POWER +PHASE_STEER;

always @(posedge CLK_FPGA)
begin
case(POSITION)
16'd1 :PHASE_STEER <=16'd88;
16'd2 :PHASE_STEER <=16'd167;
16'd3 :PHASE_STEER <=16'd470;
16'd4 :PHASE_STEER <=16'd406;
16'd5 :PHASE_STEER <=16'd230;
16'd6 :PHASE_STEER <=16'd254;
16'd7 :PHASE_STEER <=16'd24;
endcase
end
endmodule

```

Figure 3.30: Transducer1.v : example of a transducer verilog file.

Pulse Controller

The second module, `Pulse_Controller.v`, handles the PWM generation for the Tx's based on the variables defined within the transducer files. Fig. 3.31 demonstrates how the sequence of the waveform will differ depending on the phase and duty cycle. To minimize the number of possible states during a counting sequence, each transducer runs for the sequence of zero phase but at independent internals. Each transducer has a unique count value, but increments from the same clock. This is achieved by delaying the first time the clock starts to count until it reaches the proper phase value. Once it reaches the required phase, it resets to zero, providing the correct phase relative to other clocks. This process repeats if the system is reset or the focal point is changed. This process repeats if the system is reset or the focal point is changed. The structural coding for this verilog module is shown in Fig. 3.32.

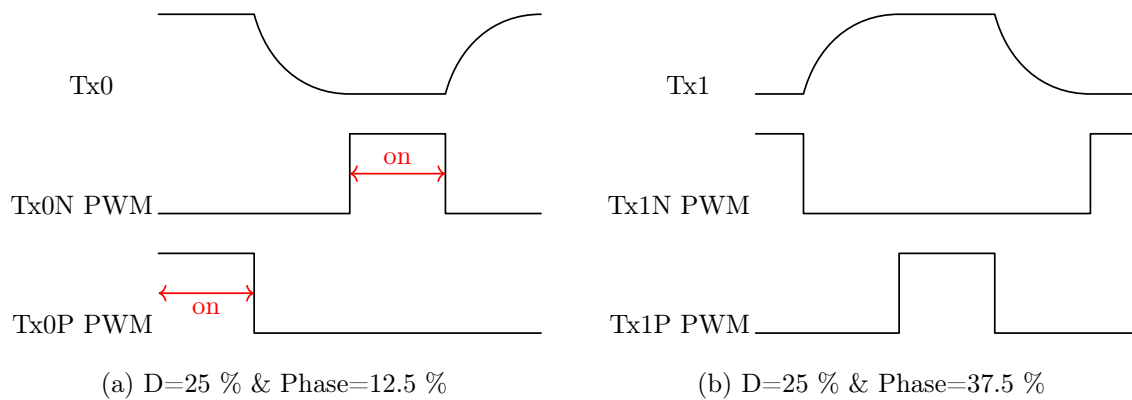


Figure 3.31: Timing diagrams to show wrapping effects of phase.

```

// calculate transition times
assign tON2 =TTOTAL -TON;
assign tOFF2 =TTOTAL / 2;
assign tON1 =tOFF2 -TON;

always @(posedge c0)
begin
  if (RESET) // full reset
  begin
    COUNTER <=0;
    RESET <=0;
    WAIT <=1;
    OUTP <=0;
    OUTN <=0;
  end
  else if (WAIT) // add phase shift
  begin
    COUNTER <=COUNTER +1;
    if (COUNTER >=TPHASE)
    begin
      WAIT <=0; // stop waiting
      COUNTER <=0;
    end
  end
  else if ( EN) // E-stop monitor
  begin
    OUTP <=0;
    OUTN <=0;
    RESET <=1; // full reset
  end
end
else
begin
  COUNTER <=COUNTER +1;
  if (COUNTER <tON1)
  begin
    OUTP <=0;
    OUTN <=0;
  end
  else if (COUNTER <tOFF2)
  begin
    OUTP <=1;
    OUTN <=0;
  end
  else if (COUNTER <tON2)
  begin
    OUTP <=0;
    OUTN <=0;
  end
  else if (COUNTER <TTOTAL)
  begin
    OUTP <=0;
    OUTN <=1;
  end
  else if (COUNTER >=TTOTAL)
  begin
    COUNTER <=0;
    OUTP <=0;
    OUTN <=0;
  end
end
end

```

Figure 3.32: Pulse_Controller.v : structural section of verilog pulse controller module.

3.6.4 Quartus and ModelSim

The verilog files are compiled and simulated in the ModelSim program for verification before FPGA implementation. The Quartus program is used after ModelSim verification for FPGA implementation.

ModelSim Simulations

The ModelSim simulation produces waveforms of the signals on a time-axis. A simulation top module file is created to generate the variables of the main module. This top module does not include the PLL module; it generates the higher frequency clock 250 MHz clock directly. This is achieved by setting the simulation step size to 1 ns in the verilog file with 'timescale and alternating c0 every two steps.

Parameters which normally require an external input, such as enable (EN) and the focus position identifier (POSITION), are generated within an initial block. They can be varied during the simulation for testing purposes by waiting a fixed number of time steps then declaring a new value. The relevant section of the code for this functionality and an example of the simulation output showing a 250 MHz clock (c0) is shown in Fig. 3.33.

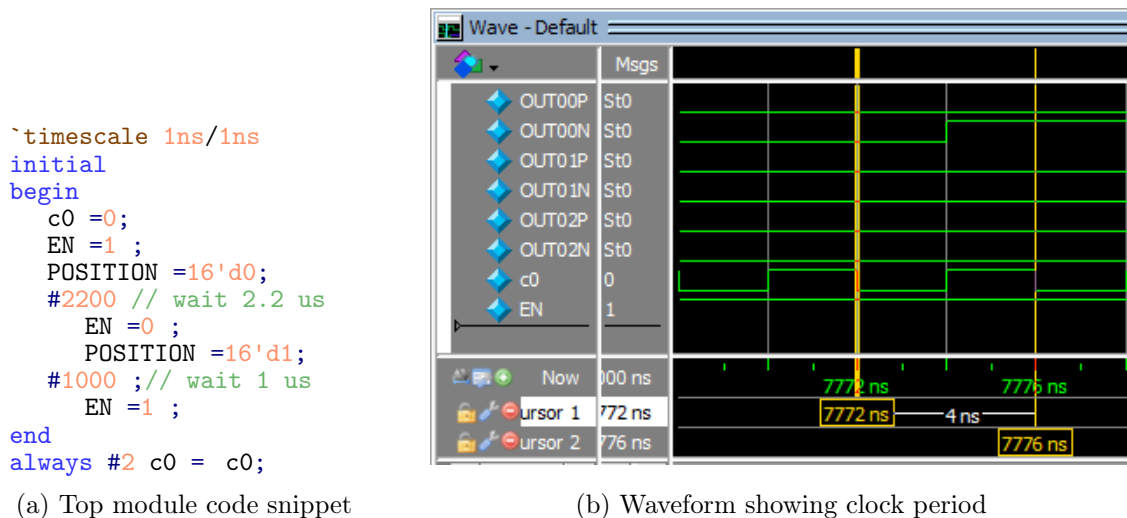


Figure 3.33: Example of ModelSim code and simulated waveform.

Quartus Programming

Quartus compiles the verilog code and verifies it's compatibility with the selected FPGA. Quartus is also used to create the PLL megafunction for the high-frequency clock. Once the code is compiled and verified, an .SOF file is created which can be used to implement the program into the FPGA's static random access memory (SRAM). Alternatively, Quartus can convert the .SOF file to a JTAG indirect configuration file, which is used to implement the program into the FPGA's EPCS. Programming into the EPCS allows the FPGA to maintain functionality after cycling power, whereas programming directly into the volatile SRAM does not.

The PLL clock count period must be known before the verilog files can be exported from MATLAB. This ensures the phases exported from MATLAB are integer equivalents. For example, if a PLL clock frequency of 250 MHz is used to generate an ultrasound frequency of 980 MHz, the counting period required would be rounded from 255.1 to 255. This design step was intentionally implemented to avoid any uncertainty with how the equivalent computations would be handled when compiling.

Two challenges arise when trying to achieve a targeted frequency: (1) the frequency changes due to the integer rounding of the counting period, and (2) the PLL clock usually does not end up being exactly the intended frequency. As a result, both the PLL ratio and clock count period must be fine tuned with trial and error testing to get to the targeted frequency, which includes exporting the integer phases again in MATLAB. The ratio of the PLL is determined by the multipliers and dividers when creating the megafunction in Quartus. This process is further explained through demonstration in Sec. 4.3.

Chapter 4

Evaluation

This chapter discusses the performance of the system through evaluation of various array designs for each stage of the design process, and by verifying functionality on electrical tests of a prototype. The first section walks through an example of the MATLAB k-Wave acoustic and thermal simulation design process proposed in Chapter 3 applied to a 24 Tx array. The next section covers the qDE design process by applying a binning process to three groups of Tx's. The third section presents an example of a solution implemented in an FPGA, verifying its functionality in ModelSim. Lastly, this chapter presents electrical testing results of a fabricated prototype, verifying both the FPGA implementation and driver circuitry.

4.1 Acoustic Simulation Results

The following simulations were conducted with the objective of creating a prototype that would be able to both prove quasi-class DE driving functional in an MR environment, while also demonstrating potential use of a compact array in head and neck hyperthermia applications. To prove qDE function, a noticeable steering would need to be demonstrated within the MR bore to prove the FPGA is able to sufficiently control the phase and duty cycle in such an environment.

A solution that could steer the focal point by a noticeable amount in each axis was found to require at least 24 Tx's. If the number of Tx's was increased to 36, the steering range doubled, however the added complexity was not necessary for the primary objectives of this thesis. The results of both the FUS_Array_RUN_Batch.m and FUS_Array_RUN_Steering.m simulations will be discussed in the context of a 24 Tx array.

4.1.1 Solution Validation

After each acoustic simulation is complete, the normalized intensity () volume is scanned for the presence of grating lobes. If there are no disconnected regions above -6 dB, no grating lobes are present and the solution is considered valid. Then, a final solution is found once each steering position for a particular solution is simulated and no grating lobes are detected.

An isometric plot can be generated to manually verify the 3D volume. An example of a focal point that has a grating lobe nearby is shown on an isometric plot in Fig. 4.1.

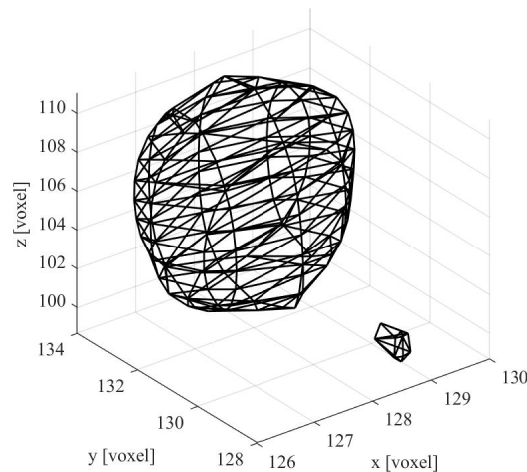


Figure 4.1: 3D Visualization of focal point and grating lobe.

4.1.2 FUS_Array_RUN_Batch.m Results

The FUS_Array_RUN_Batch.m function was used once reasonable array geometry was discovered. For the 24 Tx array used throughout this section, the starting geometry was defined as having an array geometry radius () of 25 mm, and an array geometry angle () of 60 degrees. Simulation results for this script are observed for both homogeneous simulations and heterogeneous simulations. For the homogeneous medium, it is considered as fully degassed and deionized water. For the heterogeneous medium, the volume is segmented into 3 rectangular regions: water, skin, and the average of fat and muscle.

Homogeneous Medium

This geometry results in a depth of penetration of 17.5 mm on a flat surface. For the first batch, was swept for 5 values, was swept for 4, each set was limited to 50 simulations, and the search for valid Tx positions was limited to 50000 seeds per simulation. This results in the batch executing 20 sets with up to a total of 1000 simulations. The focal point was selected at 1.5 mm off-axis in the x-direction. The PPW was set to 4.

To reduce the number of possible simulations, the execution of the set is terminated if the limit of 50000 seeds is reached for any simulation of that set. This was done to improve the overall efficiency of batch execution. It was found that if a simulation cannot populate the array with the required number of elements in 50000 attempts, then the array geometry would likely need to be changed. As a result of this conclusion, there is little reason to continue executing the set, as the geometry of a set remains the same for all simulations.

The first set took 5 hours and 20 minutes to execute 846 simulations using an NVIDIA RTX 2070 SUPER video card and AMD Ryzen 7 2700X CPU. The results are shown in Tab. 4.1.

Table 4.1: FUS_Array_RUN_Batch.m Batch 1: Homogeneous Results

Set #	[mm]	[deg]	# tx	Success [%]	Density [%]	avg. [dB]	Depth [mm]	
1	34.00	61.0	24	16	24.7	21.1	0.572	16.5
2	34.00	60.0	24	0	0.0	0.0	0.000	0.0
3	34.00	59.0	24	0	0.0	0.0	0.000	0.0
4	34.00	58.1	24	0	0.0	0.0	0.000	0.0
5	34.50	61.0	24	22	24.0	21.2	0.572	16.7
6	34.50	60.0	24	26	24.7	21.2	0.577	17.3
7	34.50	59.0	24	0	0.0	0.0	0.000	0.0
8	34.50	58.1	24	0	0.0	0.0	0.000	0.0
9	35.00	61.0	24	32	23.3	21.2	0.572	17.0
10	35.00	60.0	24	40	24.0	21.3	0.577	17.5
11	35.00	59.0	24	38	24.7	21.3	0.583	18.0
12	35.00	58.1	24	0	0.0	0.0	0.000	0.0
13	35.50	61.0	24	28	22.6	20.8	0.572	17.2
14	35.50	60.0	24	22	23.3	20.8	0.577	17.8
15	35.50	59.0	24	30	24.0	20.9	0.583	18.3
16	35.50	58.1	24	30	24.8	20.9	0.589	18.8
17	36.00	61.0	24	34	22.0	20.8	0.572	17.4
18	36.00	60.0	24	20	22.7	20.7	0.577	18.0
19	36.00	59.0	24	36	23.4	20.8	0.583	18.5
20	36.00	58.1	24	36	24.1	20.8	0.589	19.0
# of simulations per set = 50			total # of simulations = 846					

The results from Tab. 4.1 demonstrate that the initial geometry discovered ended up being a fortunate discovery because it had the highest success rate of any set. Recall, the success of a set is defined by the number of valid solutions simulated that do not have grating lobes over the total number of simulations of that set. These results also show the decision to cancel a set if the set limit of 50000 simulations is reasonable. The sets with a zero success rate indicate those that were cancelled due to meeting this criteria.

Tab. 4.1 also shows an improvement in success rate at a distance of 36 mm. The final two results on Set # 19 and 20 show a success rate of near that of set # 10. This indicates that the results beyond a distance of 36 mm should be verified with lower values of σ . The next batch was simulated accordingly, and the results are shown in Tab. 4.2.

Table 4.2: FUS_Array_RUN_Batch.m Batch 2: Homogeneous Results

Set #	[mm]	[deg]	# tx	Success [%]	Density [%]	avg. [dB]		Depth [mm]
1	36.50	60.0	24	24	22.1	20.6	0.577	18.3
2	36.50	59.0	24	38	22.7	20.7	0.583	18.8
3	36.50	58.1	24	18	23.4	20.6	0.589	19.3
4	36.50	57.1	24	32	24.1	20.7	0.595	19.8
5	37.00	60.0	24	24	21.5	20.5	0.577	18.5
6	37.00	59.0	24	18	22.1	20.5	0.583	19.0
7	37.00	58.1	24	24	22.8	20.5	0.589	19.6
8	37.00	57.1	24	30	23.5	20.6	0.595	20.1
9	37.50	60.0	24	34	20.9	20.5	0.577	18.8
10	37.50	59.0	24	28	21.5	20.4	0.583	19.3
11	37.50	58.1	24	20	22.2	20.4	0.589	19.8
12	37.50	57.1	24	28	22.9	20.5	0.595	20.3
# of simulations per set = 50			total # of simulations = 600					

Heterogeneous Medium

The layout of the heterogeneous medium is shown in Fig. 4.2. The skin layer, indicated by the vertical yellow line, is normally only a few voxels thick. The curved white line indicates the surface area of the array, and the red dot is the acoustic focal point.

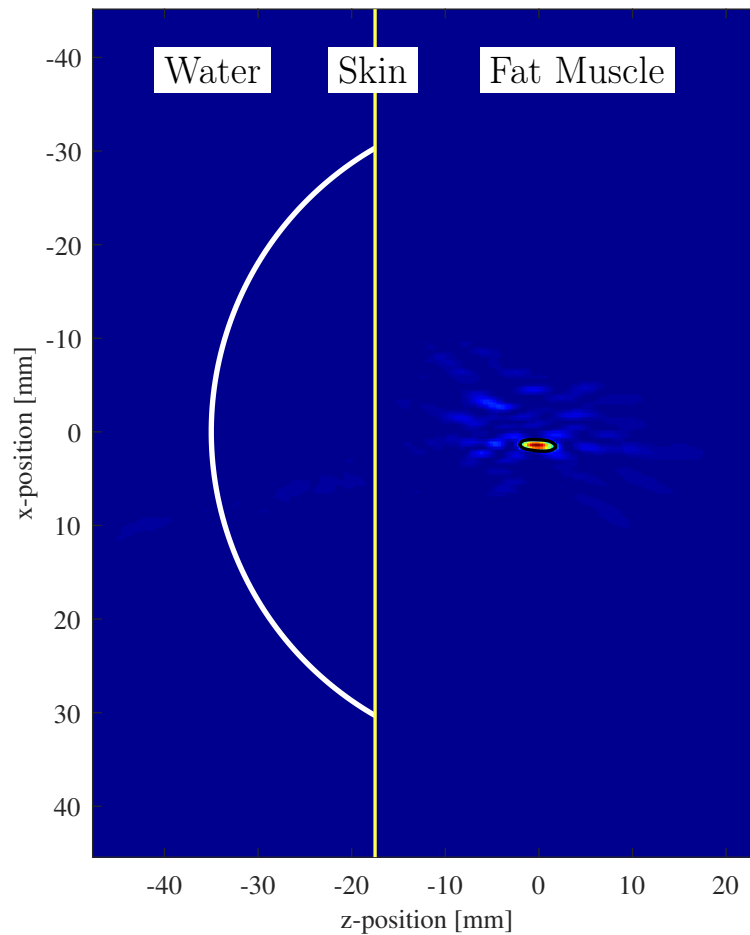


Figure 4.2: Demonstration of layout for heterogeneous medium.

The heterogeneous medium was first simulated with 4 PPW for consistency with the homogeneous simulation. As listed in Tab. 2.3, the acoustic properties of skin varies significantly from water and the average of fat and muscle in attenuation coefficient (). Unaware of how this could impact the accuracy of simulations, two versions were completed to assess the impact. The first version did not consider the variance of α , and only considered the variance of density () and sound speed (). The second also considered the variance of α . Planar views of the are shown in Fig. 4.3 with the array steering 1.5 mm off it's geometric centre.

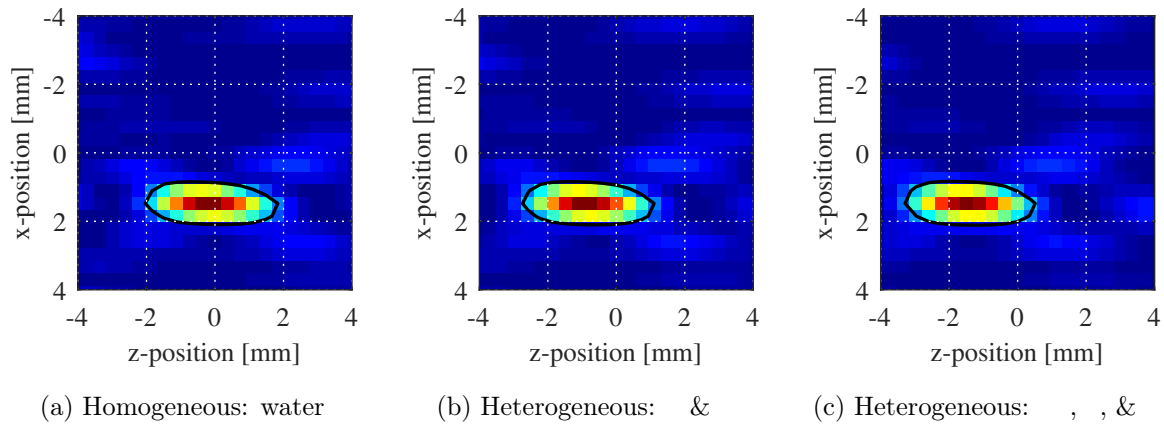


Figure 4.3: , 4 PPW : comparison of homogeneous and heterogeneous mediums.

The results from Fig. 4.3 show that, although the focal point continues to steer 1.5 mm off axis as intended, the heterogeneity causes the focal point to shift in the z -axis. The effect is magnified when the variance is considered. Although the focal point is shifted, there are no grating lobes detected for the same seed and geometry irrespective of the degree of heterogeneity considered.

To evaluate if the 4 PPW used for the previous simulations are sufficient, the number of PPW was increased and the results between homogeneous and heterogeneous were once again compared. The PPW was increased to 6, pushing the domain size used for simulation to $512 \times 512 \times 256$. In comparison, the domain size with 4 PPW was $256 \times 256 \times 162$.

For a 6 PPW domain size, the simulations needed to be run off of the CPU code rather than GPU due memory limitations. This resulted in a significant increases simulation time. The time required for a single CPU simulation was 125 minutes for heterogeneous, and 90 minutes for homogeneous. In comparison, the GPU simulation with 4 PPW took 66 seconds for both homogeneous and heterogeneous mediums.

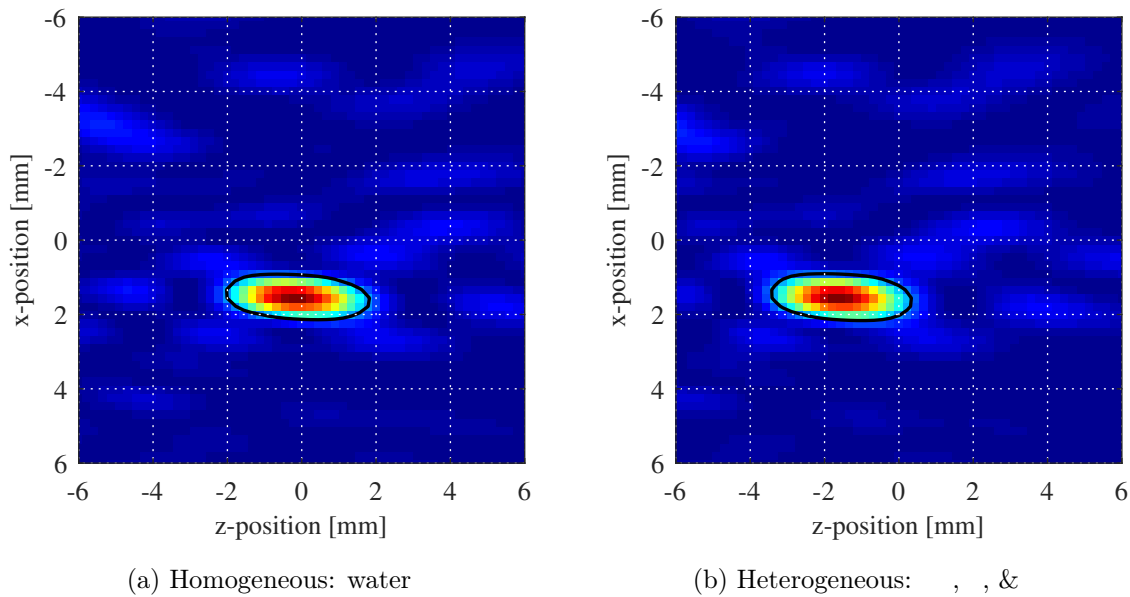


Figure 4.4: , 6 PPW : comparison of homogeneous and heterogeneous mediums.

4.1.3 FUS_Array_RUN_Steering.m Results

Now that the array geometry is selected, the steering position must be simulated to find a solution that is valid for all required positions. A larger list of seeds is required than those from the 50 iterations from selected set in Tab. 4.1.

FUS_Array_RUN_Initial.m was run with a homogeneous medium for the selected set for 675 simulations at a single off-centre steering position. The seeds were 31.1% successful, resulting in 210 seeds being searched for FUS_Array_RUN_Steering.m function.

From these 210 seeds FUS_Array_RUN_Steering.m found 18 seeds that were valid for six 1.5mm off-centre positions, and for the geometric centre. To reduce the number of valid seeds further, the 18 seeds were simulated once again but with the heterogeneous medium.

10 seeds of 18 were verified correct for the heterogeneous simulation despite the focal point moving about 1.7 mm in the z-axis. The results for one of the seeds for one off-centre steering position is shown in Fig. 4.5.

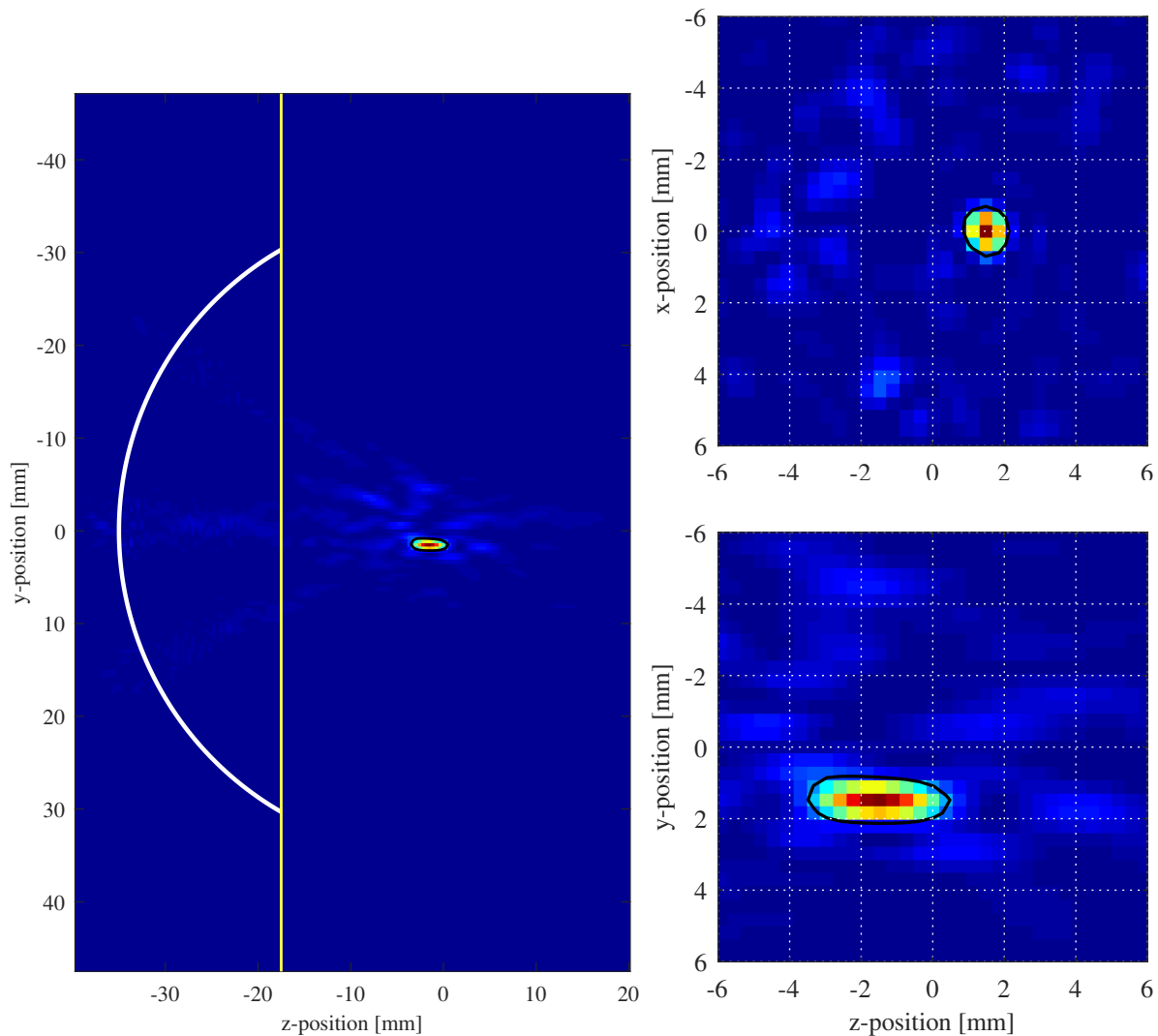


Figure 4.5: Normalized intensity example in heterogeneous medium.

4.1.4 FUS_Array_RUN_Heating.m Results

The heating simulations were executed using the recorded time variant pressure and the tissue properties from FUS_Array_RUN_Steering.m. These acoustic simulations were executed with the previously defined heterogeneous medium, which included the tissue attenuation coefficient. The power of the source was set to 12 W, which is approximately 50 % of power that 24 Tx's can deliver with a of 60 V and an of 100 %. Attaining this value of effective power delivered to load () will be shown in Sec. 4.2.

Simulating a 10 minute application took 3.3 hours to fully simulate, and a 30 minute application took 10 hours. The target temperatures were adjusted to better compensate for the offset. The target was first raised to 42.5° for the 10 minute test, then further to 43.5° for the 30 minute test. The resulting heterogeneous heating simulations are shown in Figure 4.6.

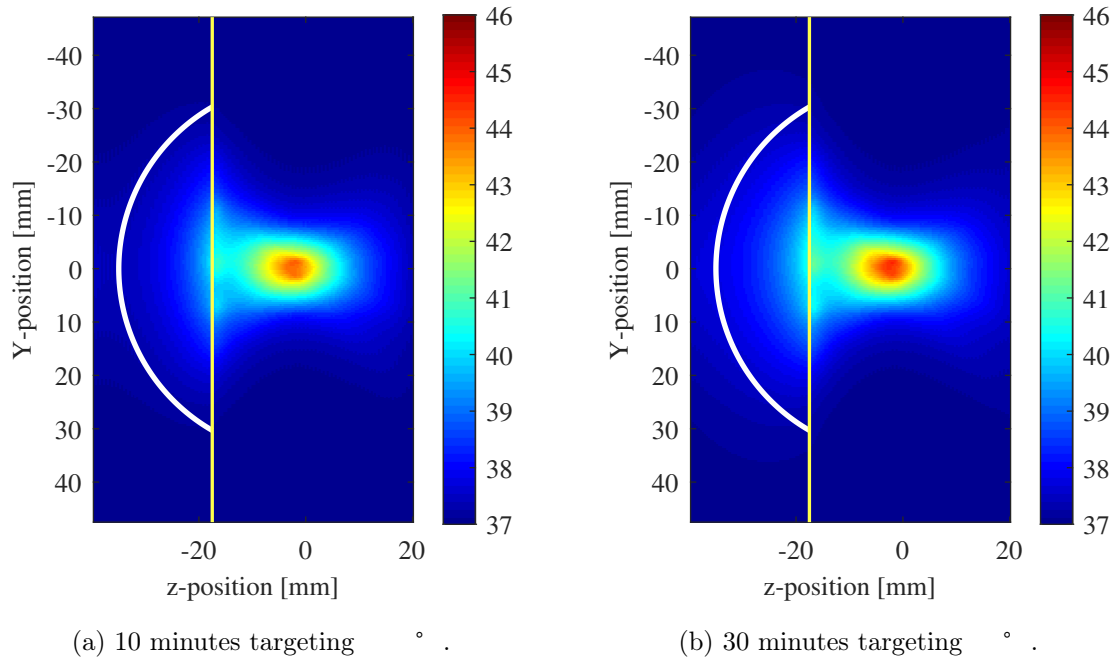


Figure 4.6: Heterogeneous heating simulations using kWaveDiffusion.

For the 30 minute test there is more heating on the skin observed, however, the water around that area is also warmer. This is an unrealistic scenario as the water within the array would likely be circulated, thus in reality the skin temperature may not have such a large variance between both tests.

4.1.5 Discussion

By simulating thousands of potential solutions, valid array solutions can be found with sufficient steering and performance which may not otherwise have been available with such sparsity and low number of elements. Over 1000 homogeneous simulations were complete to find 18 seeds that were valid for all steering positions, and 10 of those were valid for heterogeneous simulations. Using this broad search of pseudo-random element positions yielded good results in simulation for both homogeneous and heterogeneous mediums. It should be noted, however, that the heterogeneities varied symmetrically about the x and y axis. The spatial variance was only in the z-axis. Therefore, simulation alone, even with more variance, cannot replicate the real conditions in a human body. It cannot yet be known if these low sparsity arrays will work in reality as well as they do in simulations.

The heating simulations show that with 12 W of acoustic power a focal point is able heat a localized volume volume with sufficient power for maintained hyperthermia. The issue however is that due low depth of penetration, the small volume between the skin and the focal point is subject to heat buildup. Possible solutions would be cooling the water within the array to cool the skin, and building the array non-planar on the exposed surface. Building the arrays more elliptically with a non-planar surface that rests on the patient would allow both better depth of penetration and an increased conduction angle (ϕ) in at least some directions. This increased ϕ would likely shorten the focal point length, causing a lower amount of heat to be produced along the z-axis in unwanted volumes.

Overall, the results of the acoustic and thermal simulations show that a compact phased array with a low number of elements may provide sufficient performance for applications of hyperthermia, especially those of head and neck tumours where an alternative solution is lacking.

4.2 Quasi Class-DE Driver Power Balancing

Three sets of Tx's were fabricated, characterized, and simulated to assess compatibility with qDE driving. The piezoelectric elements were ordered from the manufacturer DeL Piezo Specialties LLC under different criteria, as per Tab. 4.3.

Table 4.3: Transducer group design criteria

Group	#	Material	Resonant	Diameter	Thickness	Measured
A	10	DL-47	1±5% MHz	7±0.05 mm	–	no
B	7	DL-47	–	7±0.05 mm	2.8 ±0.03 mm	yes
C	40	DL-47	1±5% MHz	7±0.05 mm	–	no

Variance in acoustic conversion efficiency () of each Tx was not considered. Though the algorithms used are capable of considering the individual , equipment for making these measurements was unavailable at the time of evaluation. For all solutions discussed in this section, the acoustic conversion efficiency is considered to be 100 %.

The following evaluations will demonstrate the effects of binning the Tx's on qDE driving, and present various solutions for driving. Binning is the process of selecting which of the fabricated transducers to include in the arrays. Solutions are considered at two DC voltage of the qDE driver () voltages: 30 V and 60 V. 60 V offers better efficiency and can deliver more power, however 30 V, is more practical for laboratory electrical testing. As such, 30 V solutions are more predominant than 60 V solutions in the results discussed in this section.

4.2.1 Group A Transducers

The scattering parameter reflection coefficient (S11) from each Tx in group A are shown in Fig. 4.7. 3 distinctive resonances around the intended phased array driving frequency () of 1 MHz are visible. There is a larger variance between elements observable in the left-most resonance. Due to this larger variance, only the 2nd and 3rd resonances will be considered for qDE driving. The middle and right-most resonances will be used to select and respectively.

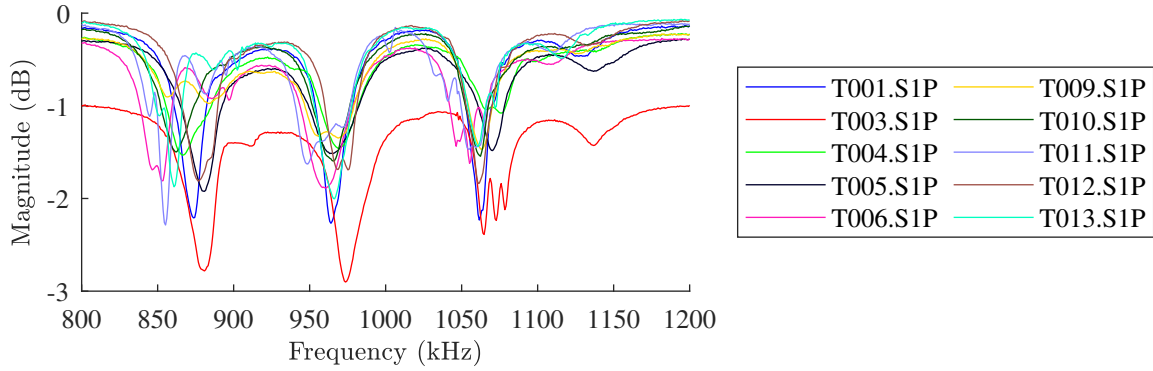


Figure 4.7: Group A : S11 magnitude at all 3 resonances around 1 MHz with 10 TxS.

There is a clear outlier shown in Fig. 4.7 at all frequencies. The unacceptability of this transducer is also confirmed when observing the efficiency of each transducer versus P_L , as shown in Fig. 4.8. This transducer was immediately removed from all future considerations.

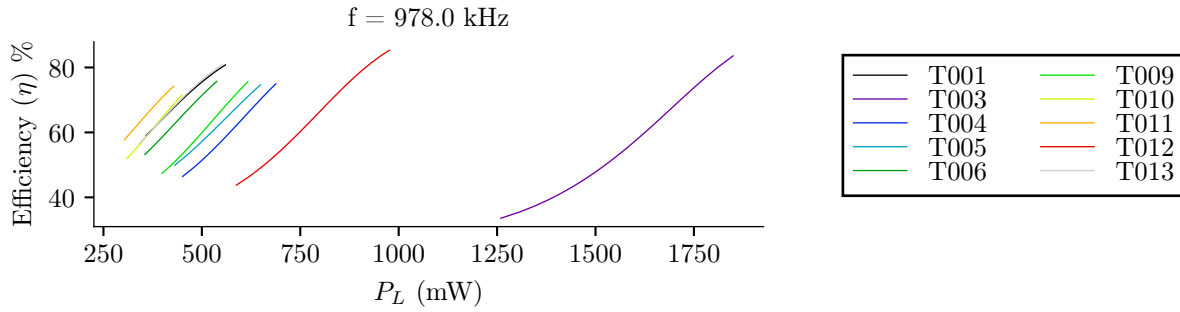
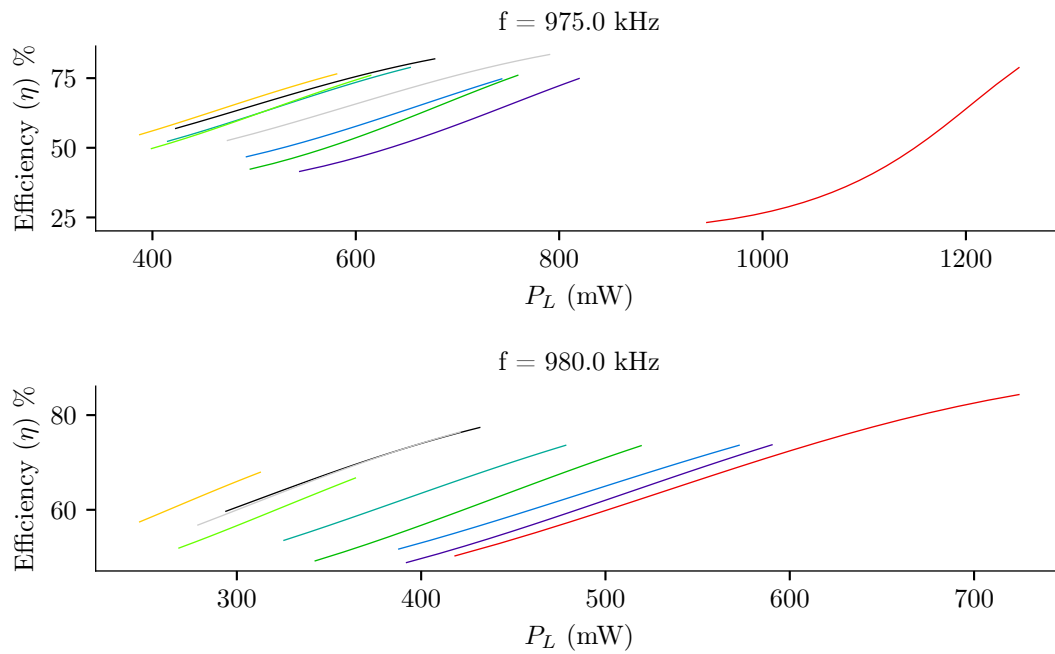


Figure 4.8: Group A : η vs. P_L of 10 TxS.

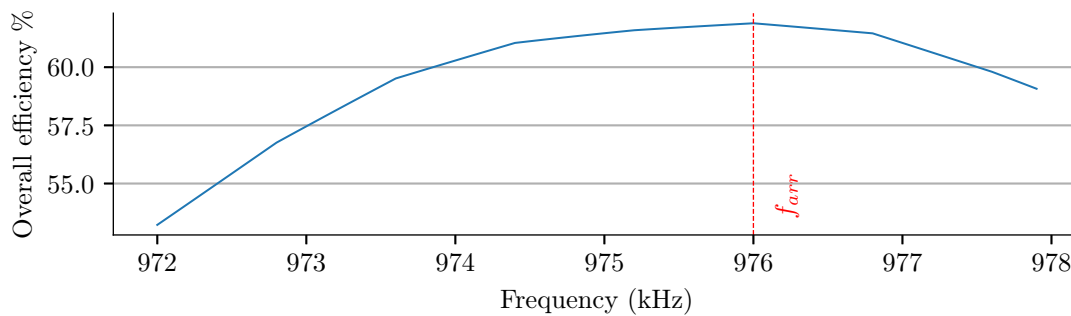
Group A: $f_{res,1}$ Solutions

This section investigates driving solutions around the first resonance ($f_{res,1}$). The S11 parameters extracted for each of the 9 TxS around $f_{res,1}$ are shown in Tab. A.1.

A solution was not found for qDE driving with this group of 9 TxS. TxS need to be removed to reduce the variance within the group. To select which element is removed next, 2 frequencies between the highest f_S and lowest f_P were simulated for η vs P_L plots, shown in Fig. 4.9. As power must be equalized, these plots hint at optimal groupings at each frequency, and therefore indicate which elements to remove next.

Figure 4.9: Group A : η vs. P_L of 9 tx

With the 8 remaining transducers, a solution was found for non-ideal qDE driving. The performance of the array was evaluated across range of frequencies to determine the optimal phased array driving frequency (f_{arr}). These results are shown in Fig. 4.10 and Fig. 4.11.

Figure 4.10: Group A, $f_{arr,1}=976 \text{ kHz}$: η of 8 Txs.

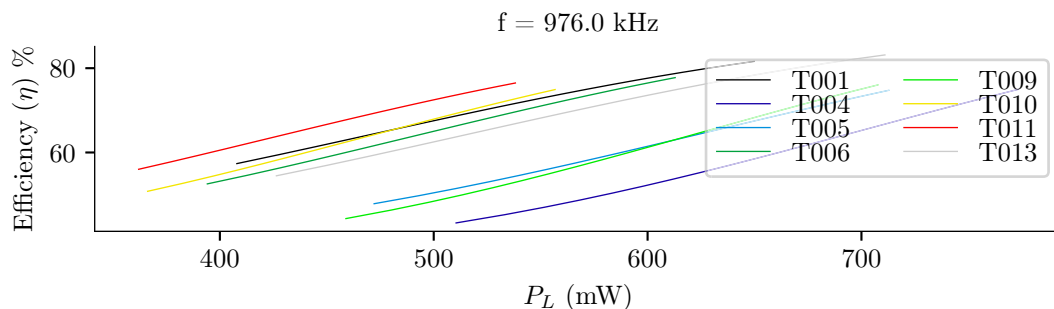


Figure 4.11: Group A, $f_{arr,1}=976$ kHz : P_L of 8 Tx.

In Fig. 4.10 it is observable that η appears to be relatively low, with a maximum of 62% at 976 kHz. f_{arr} was set to the point of maximum efficiency. Though a solution exists for these 8 Tx exists, an attempt was made to increase efficiency through further binning. The power sweep in Fig. 4.11 was observed for indication of which Tx to remove.

From Fig. 4.11 there appears two observable sub-groupings. T004, T005, and T009 were the least populated grouping, and as such, were removed from the next solution.

The results in Fig. 4.12 show an improved efficiency of 72%. Fig. 4.13 shows P_L is approximately 550 mW at the frequency of maximum efficiency.

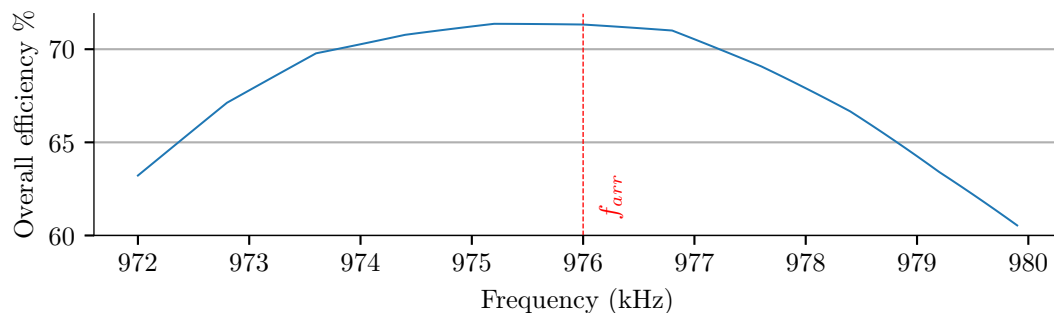


Figure 4.12: Group A, $f_{arr,1}=976$ kHz : η of 5 Tx.

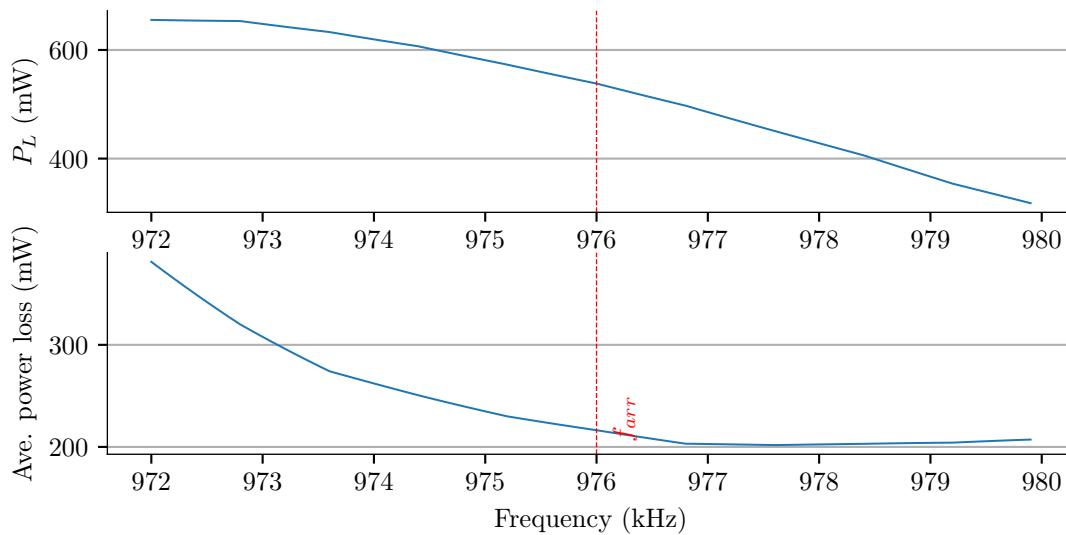


Figure 4.13: Group A, $f_{arr,1}=976$ kHz : P_L of 5 TxS.

Previous solutions were found using an arbitrary V_{DE} of 30 V. A method of increasing total power delivered to the array without increasing the number of TxS is by increasing V_{DE} . By obtaining the required power by adjusting V_{DE} rather than f_{arr} , f_{arr} can be set to the f of maximum η . The results of increasing V_{DE} in the figures Fig. 4.14 and Fig. 4.15 below show an increase in η but a 400% increase in P_L .

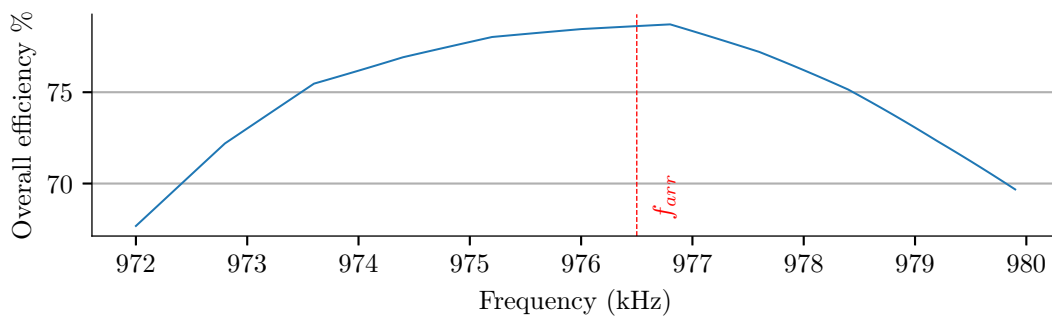


Figure 4.14: Group A, $f_{arr,1}=976.5$ kHz, $V_{DE}=60$ V: η of 5 TxS.

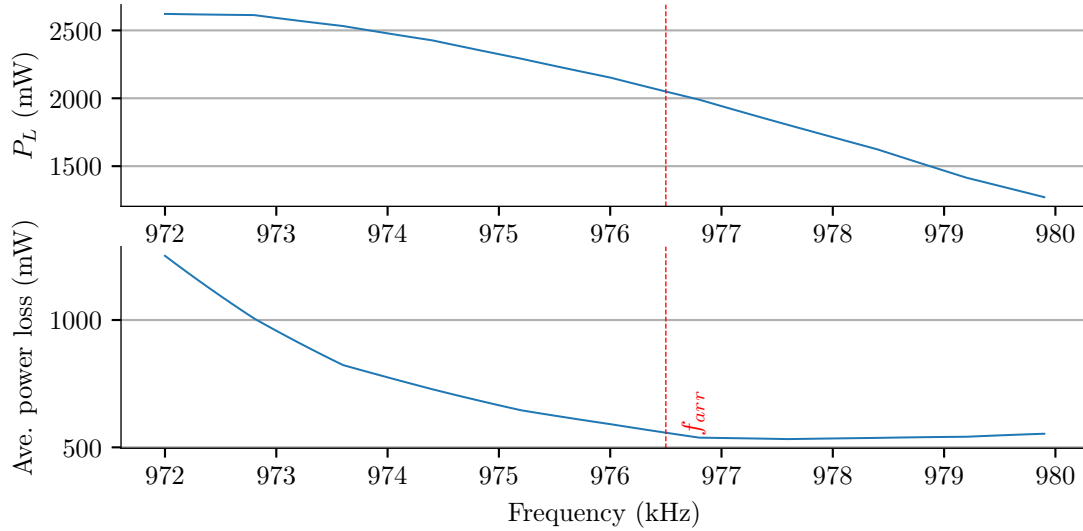


Figure 4.15: Group A, $f_{arr,1}=976.5$ kHz, $V_{DE}=60$ V : P_L of 5 TxS.

Group A: $f_{res,2}$ Solutions

The next resonant frequency, ($f_{res,2}$), is evaluated for compatibility with qDE driving using the same techniques presented in Sec. 4.2.1. The S11 parameters extracted from each of the 9 transducers are shown in Tab. A.1, and the magnitude of the reflections are plotted in Fig. 4.16.

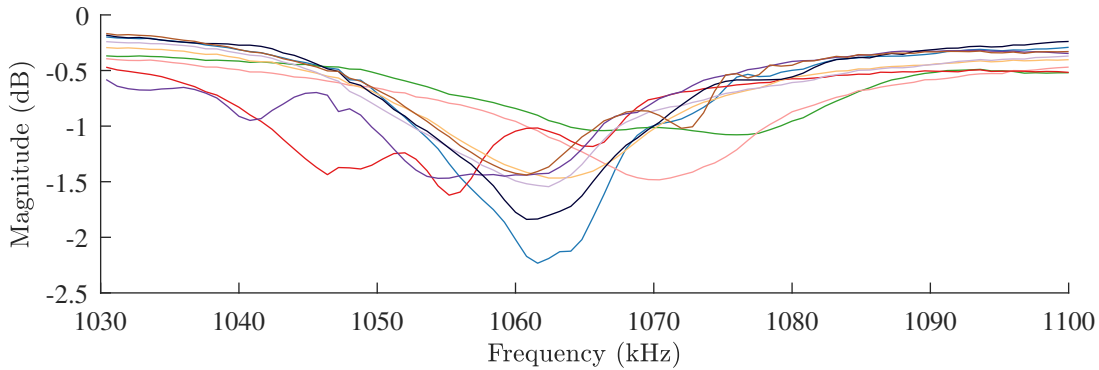


Figure 4.16: Group A, $f_{arr,2}$: S11 magnitude of 9 TxS.

A frequency roughly between f_S and f_P was selected from Fig. 4.16. The power was then swept at this frequency, 1070 kHz. A clear grouping at reasonable efficiency is observed in Fig. 4.17. From this sweep it is clear that T006 and T011 were next to be removed.

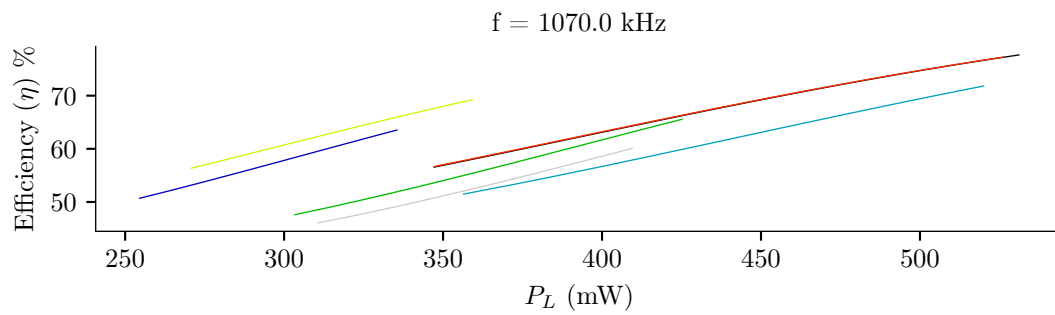


Figure 4.17: Group A, $f_{arr,2}=1070 \text{ kHz}$: P_L of 7 TxS.

The remaining 5 transducers yielded a reasonable solution with an efficiency of 63% at 1070.2 kHz. The results are shown in Fig. 4.18 and Fig. 4.19.

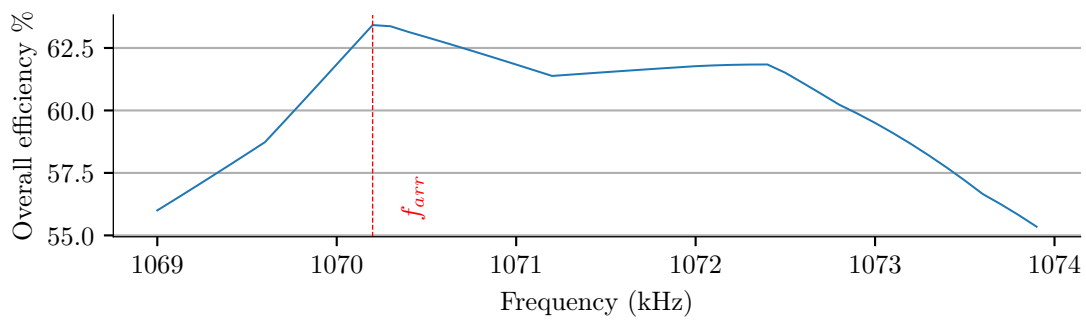


Figure 4.18: Group A, $f_{arr,2}=1070.2 \text{ kHz}$: η of 5 TxS.

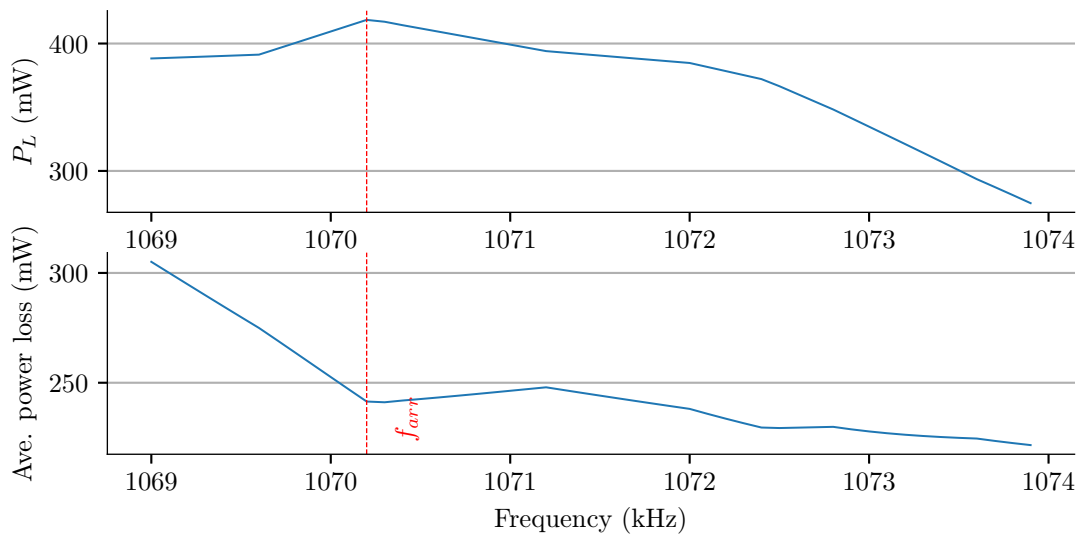


Figure 4.19: Group A, $f_{arr,2}=1070.2$ kHz : P_L of 5 Tx.

V_{DE} was increased to 60V for the selection of 5 Tx. The maximum η was improved by 9%, to 72%. The P_L of $f_{arr,2}$ was quadrupled in comparison to the 30 V solution, as shown in Fig. 4.21.

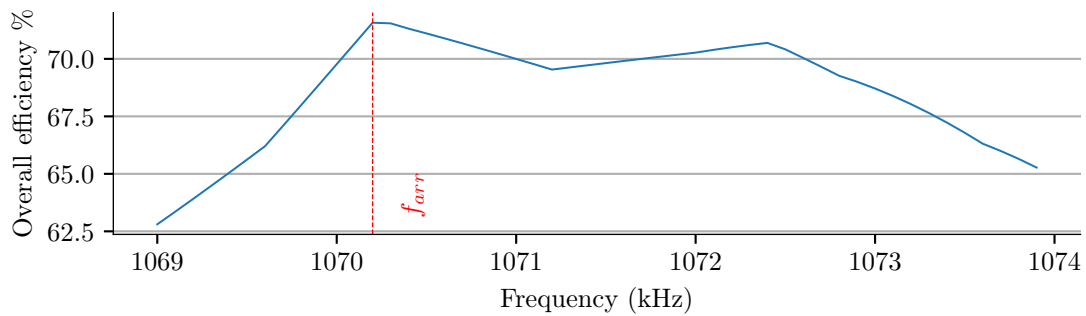


Figure 4.20: Group A, $f_{arr,2}=1070.2$ kHz, $V_{DE}=60$ V : η of 5 Tx.

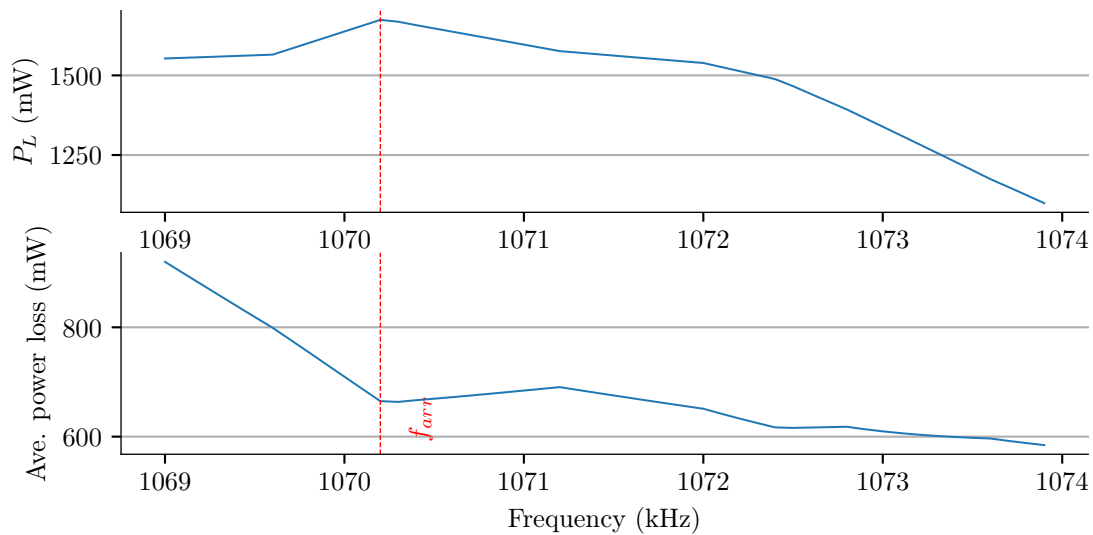


Figure 4.21: Group A, $f_{arr,2}=1070.2$ kHz, $V_{DE}=60$ V : P_L of 5 Txs.

4.2.2 Group B Transducers

The transducers in group B exhibited drastically different behaviour than those of group A or group C. This is due to their drastically different thickness, with the piezoelectric material being roughly twice that of the other 2 groups. They also do not use the same casing design, but this is much less relevant. They are shown in Fig. 4.22



Figure 4.22: Picture of group B Txs.

Acoustic Conversion Efficiency

The acoustic conversion efficiency () was unable to be considered for all Tx's due to restrictions in equipment availability at the time of evaluation. Only the acoustic conversion efficiency of one transducer, T001, was characterized at an earlier date, and the results are shown in Fig. 4.23.

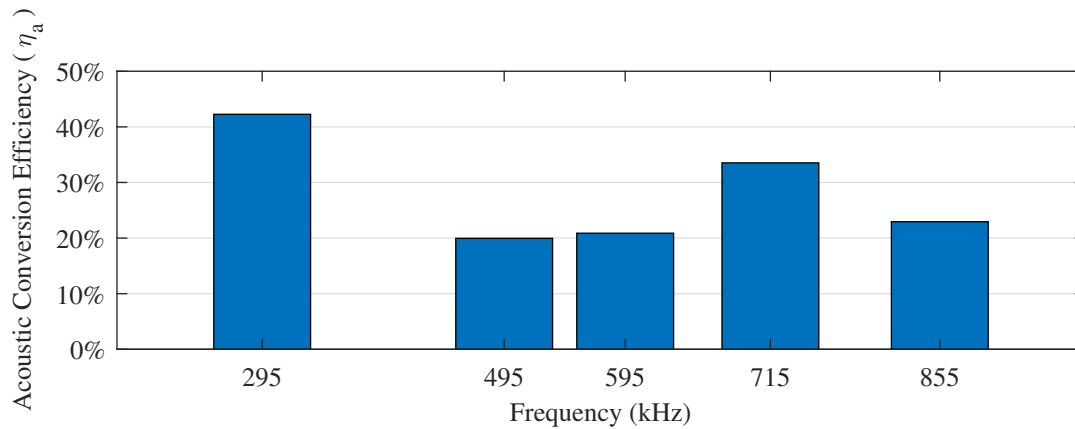


Figure 4.23: Group B: wide S11 magnitude of 7 Tx's.

S11 Transducer Parameters

The magnitude of S11 parameters of all 7 fabricated Tx's in group B are shown in Fig. 4.24. For this group of Tx's, there are multiple resonances, with two more prominent resonances around 290 kHz, and another around 700 kHz. These resonances also coincide with the highest , as shown in Fig. 4.23.

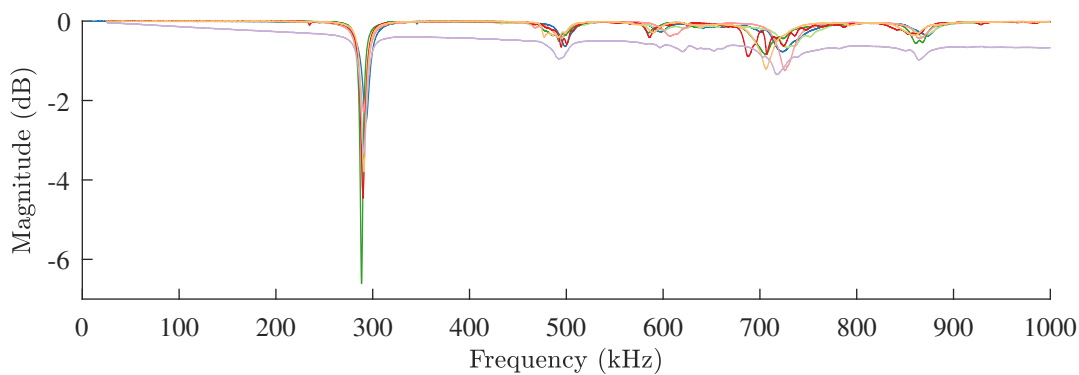


Figure 4.24: Group B: wide S11 magnitude of 7 Tx's.

There is an obvious outlying Tx in Fig. 4.24, which was immediately removed from all qDE solution considerations. The parameters extracted from S11 measurements are shown in Tab. A.3.

Narrow S11 magnitude plots around both ω_1 and ω_2 are shown in Fig. 4.25 and Fig. 4.26. ω_1 shows much less variance between elements, therefore only ω_1 will be considered for qDE solutions.

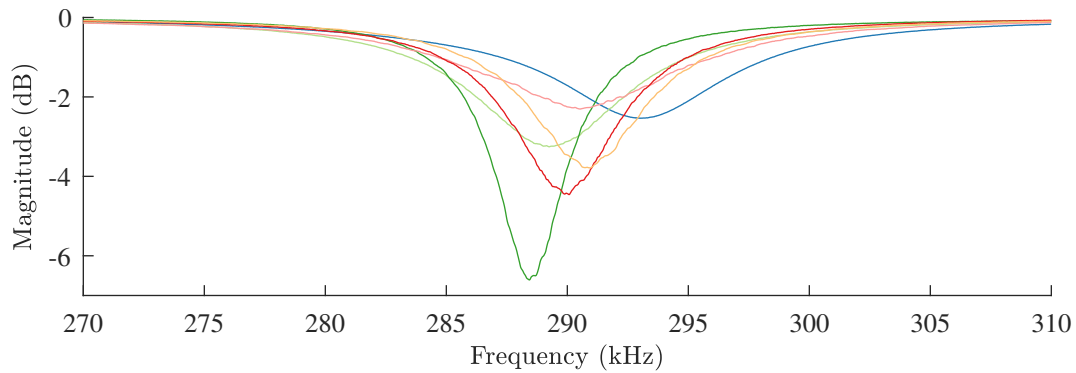


Figure 4.25: Group B, ω_1 : S11 magnitude of 6 Tx's.

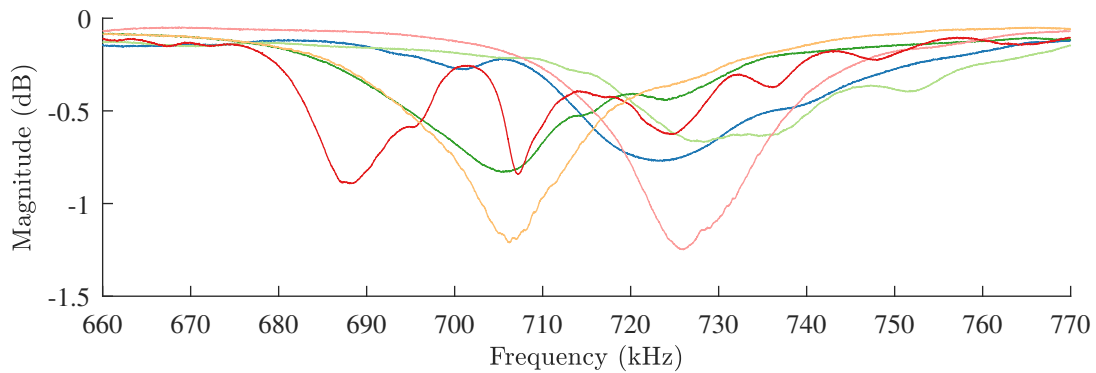


Figure 4.26: Group B, ω_2 : S11 magnitude of 6 Tx's.

A solution for qDE driving was found for all 6 Tx's. Tx's were binned in the same manner as explained for group A. The results are shown in Fig. 4.27 and Fig. 4.28.

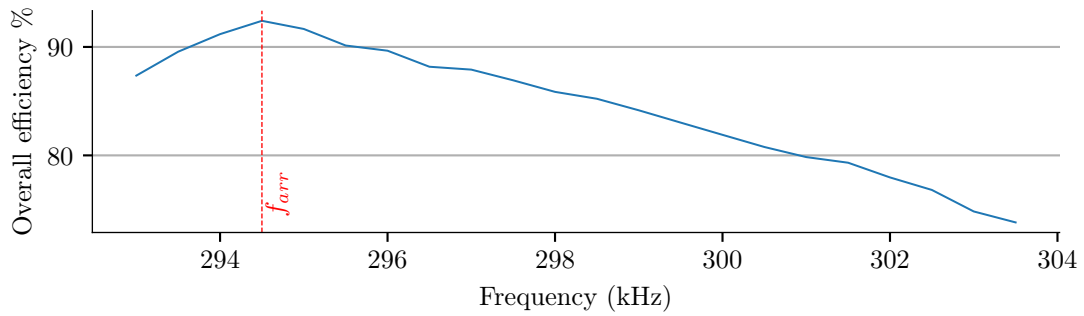


Figure 4.27: Group A, $f_{arr}=294.5$ kHz, : overall array electrical efficiency (η) of 4 Tx, T001 T002 T007 removed.

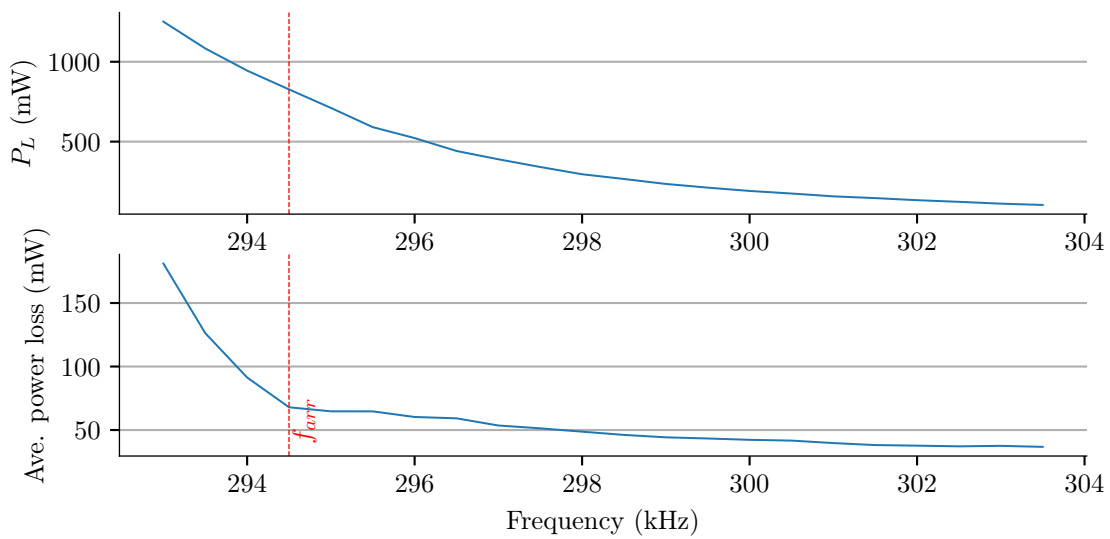


Figure 4.28: Group A, $f_{arr}=294.5$ kHz : effective power delivered to load (P_L) of 4 Tx, T001 T002 T007 removed.

4.2.3 Group C Transducers

Group C is an extension to group A; more Tx's were fabricated and added to group A, resulting in a total of 40 Tx's. Only the first resonance peak of the 3 resonances was observed. They are shown in Fig. 4.29 temporarily stored in a threaded board.



Figure 4.29: Picture of group C Tx's.

Group C Transducers at 30 V

9 Tx's were removed immediately due to unacceptable characteristics observed in both the S11 plots and after extracting the equivalent circuit parameters. 6 Tx's showed open circuit behaviour, and 3 elements resulted in a negative parallel capacitance (). The S11 parameters extracted for each of the 31 Tx's are shown in Tab. A.4. The S11 from 31 of 40 Tx's in group C are shown in Fig. 4.30.

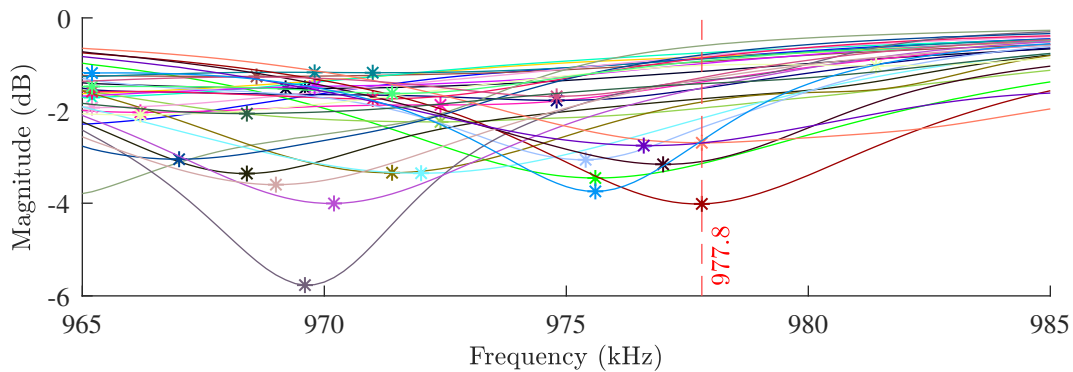


Figure 4.30: Group C : S11 magnitude of 31 Tx's.

No solution to qDE was found for these 31 elements. To further reduce the number of elements, Fig. 4.30 was observed to remove outliers. Some elements showed resonances of slightly higher frequency than the majority, as shown by the vertical marker at 977.8 kHz. As f_{arr} must be between f_S and f_P , the outliers to the far right were removed to widen the overall bandwidth between f_S and f_P . One element showed a second local minimum at around 981 kHz, and was also removed. The S11 from 26 of 40 Tx's are shown in Fig. 4.31, and the power sweeps for various frequencies shown in Fig. 4.32.

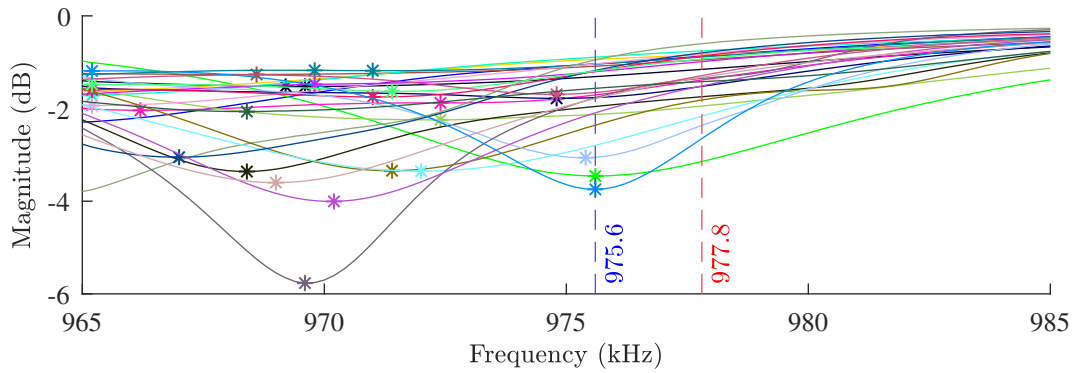


Figure 4.31: Group C : S11 magnitude of 26 Tx's.

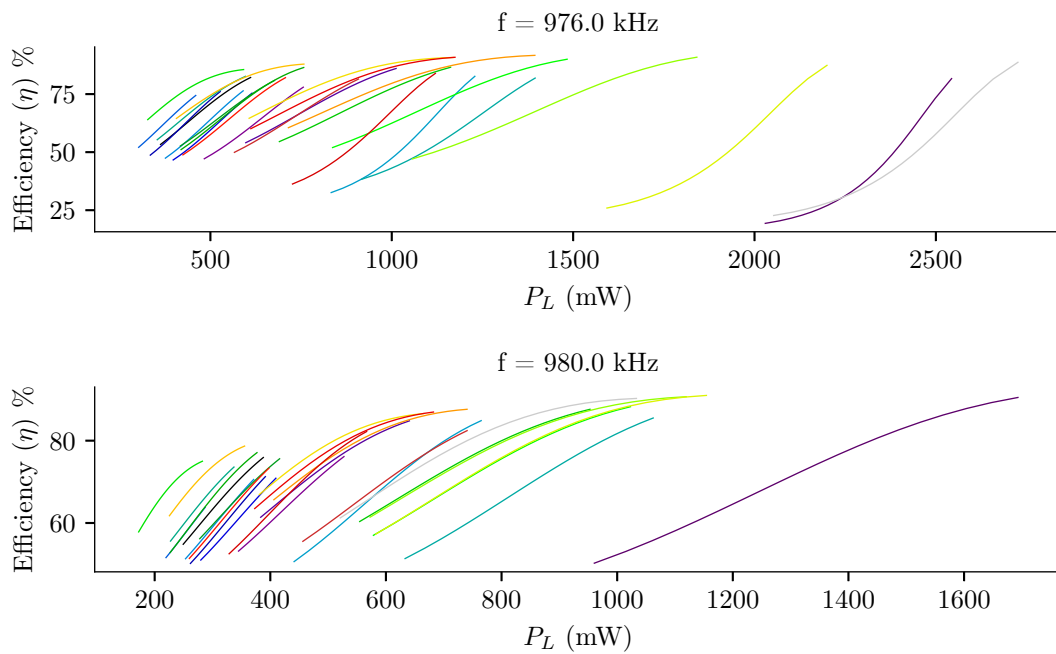


Figure 4.32: Group C : η vs. P_L of 26 Tx's.

As P_L must be set to a fixed value, Fig. 4.32 shows no value of P_L could be selected such that a majority of elements could be used at the same time. To explore if lower frequencies would result in better groupings, more Tx's with higher frequency resonances were removed. The results are shown in Fig. 4.33 and Fig. 4.34.

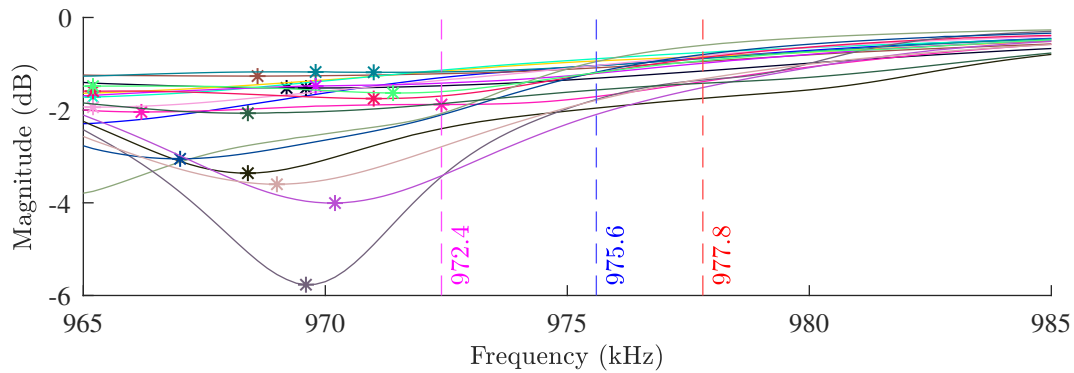


Figure 4.33: Group C : S11 magnitude of 23 Tx's.

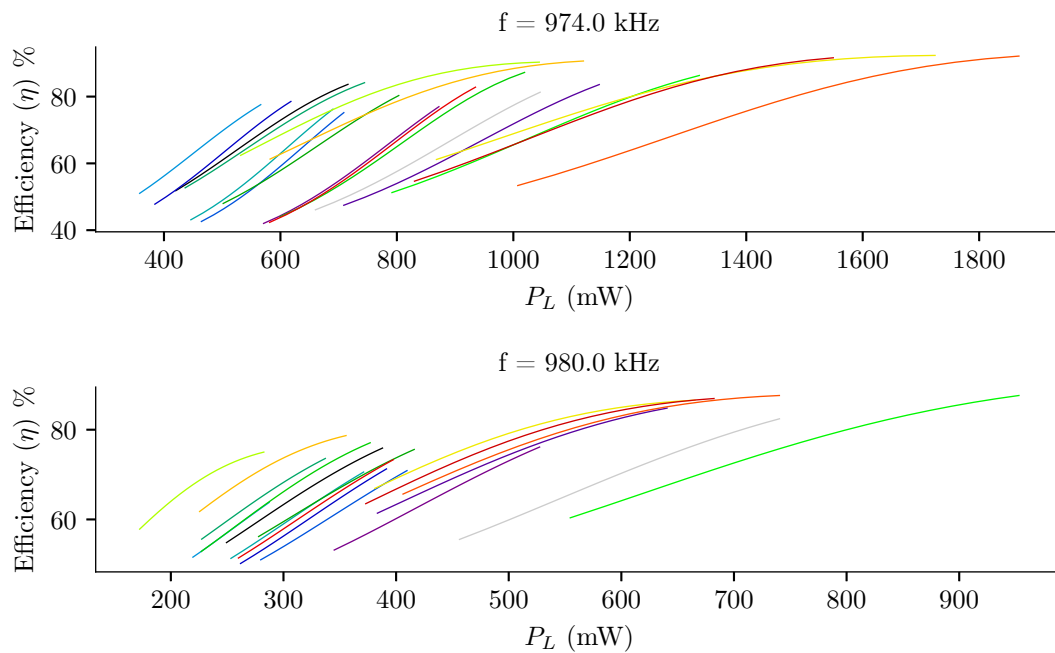


Figure 4.34: Group C : η vs. P_L of 23 Tx's.

As shown in Fig. 4.34, there were still no good groupings available. A frequency was selected that resulted in the best groupings, then the Tx's were further binned by removing the outermost Tx's on the power sweep curve at 977 kHz. The results of the remaining 11 Tx's are shown in Fig. 4.35 and Fig. 4.36

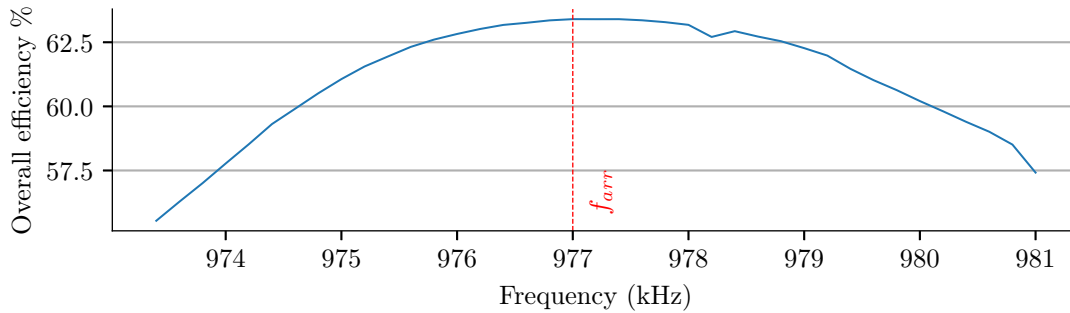


Figure 4.35: Group C, $f_{arr}=977$ kHz, : η of 11 Tx's.

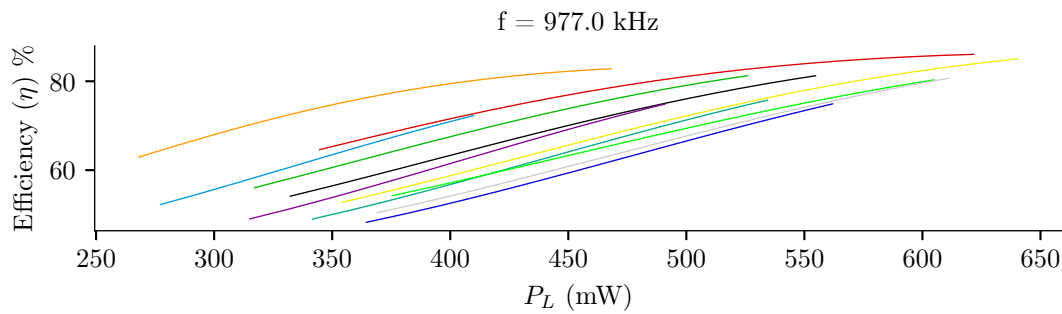


Figure 4.36: Group C, $f_{arr}=977$ kHz : η vs. P_L of 11 Tx's.

Although a solution for qDE is available for 11 Tx's, the peak efficiency is relatively low at approximately 63%. The efficiency can be further increased to approximately 72 % by removing a single Tx. This grouping of 10 Tx's will be used as the primary solution. The performance of the new grouping of 10 Tx's are shown in Fig. 4.37.

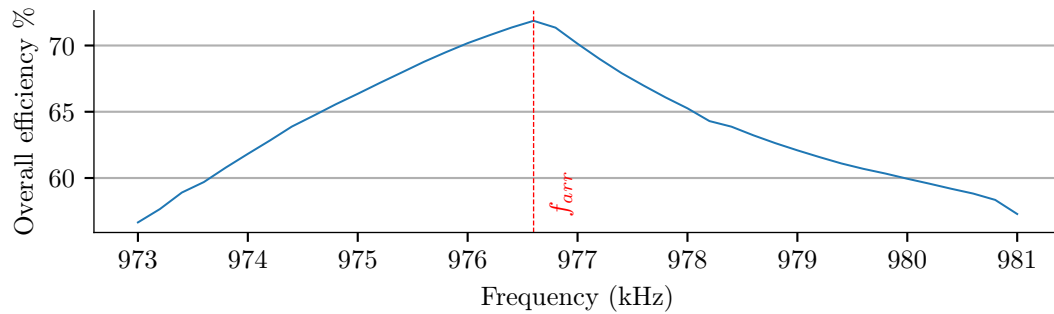


Figure 4.37: Group C, $f_{arr}=976.6$ kHz, : η of 10 Tx.

Fig. 4.38 shows the effective power delivered to load (P_L) was plotted over f_{arr} . At and f_{arr} of 76.6 kHz, the P_L was 500 mW considering 100 % acoustic conversion efficiency.

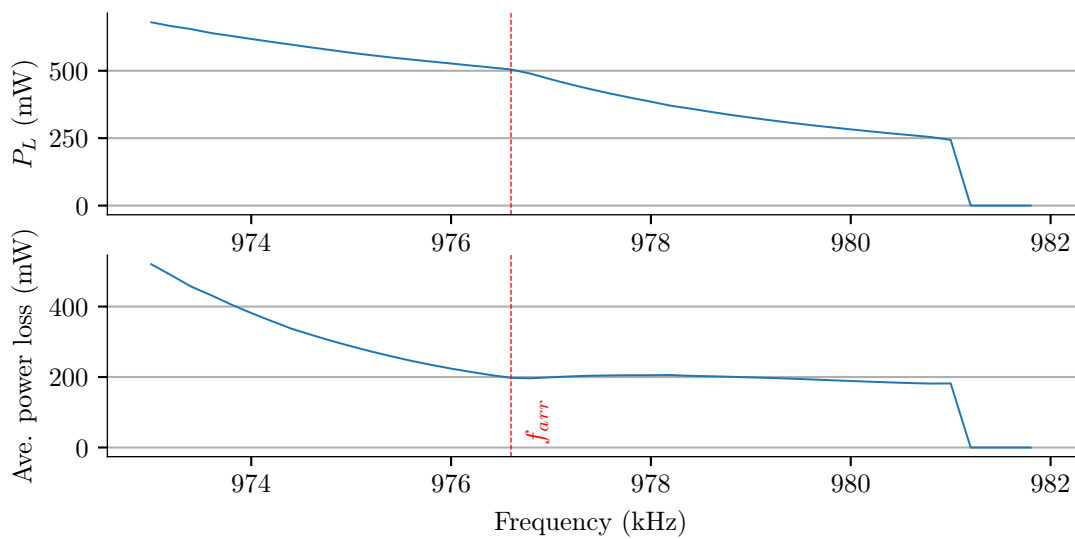


Figure 4.38: Group C, $f_{arr}=976.6$ kHz, : P_L of 10 Tx.

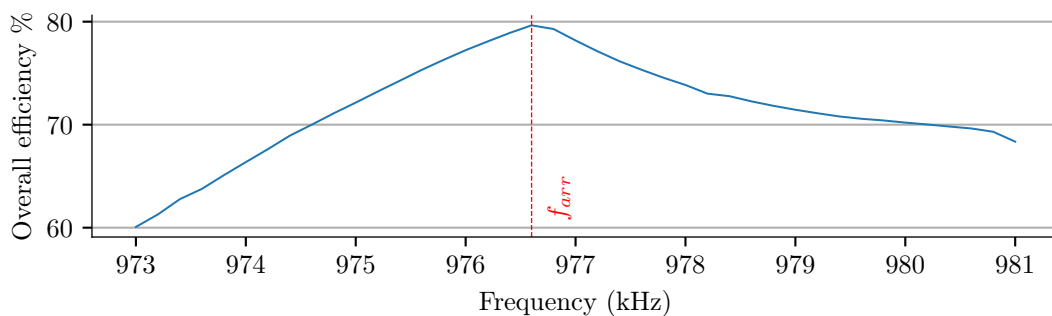
The results of the parameters needed for each Tx to drive the array based on Fig. 4.37 are shown in Tab. 4.4. The results of this table are scaled to the period count the FPGA will use.

Table 4.4: Each Tx's driving parameters for $f_{arr}=976.6$ kHz at .

Tx #	#01	#06	#09	#11	#14	#15	#17	#20	#28	#34
C_{ext} [pF]	52.89	0.00	71.06	46.35	33.25	94.70	135.08	67.21	106.59	119.22
Duty	0.20	0.23	0.19	0.20	0.20	0.16	0.18	0.20	0.16	0.17
Phase [deg]	109.4	97.7	112.9	107.0	108.4	122.3	114.4	107.0	123.2	117.0
Duty [scaled]	49	57	47	51	50	40	46	51	39	44
Phase [scaled]	76	68	78	74	75	85	79	74	86	81

Group C Transducers at 60 V

The voltage of the transducers from was increased to 60V to increase both the efficiency and P_L . As a superseding PWM signal is used to control the power, the high voltage offers the advantage of both a faster temperature ramp up time, and higher efficiency. The performance of the grouping of 10 Txs at 60 V are shown in Fig. 4.39 and Fig. 4.40. Doubling the voltage has the effect if increasing the efficiency by 8 % while increasing the power by a factor of 4.

Figure 4.39: Group C, $f_{arr}=976.6$ kHz, 60 V : η of 10 Txs.

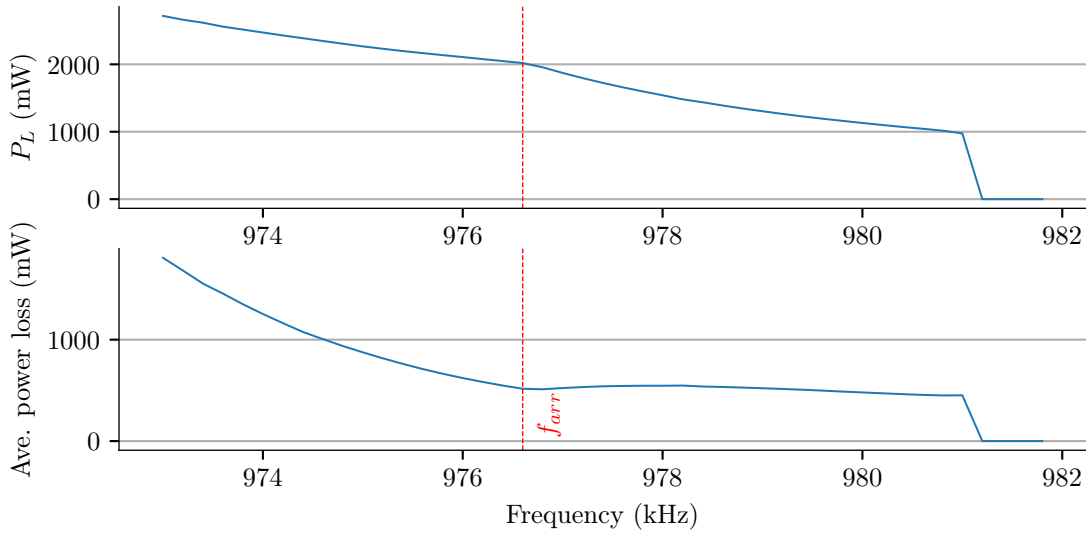


Figure 4.40: Group C, $f_{arr}=976.6$ kHz, 60 V : P_L of 10 TxS.

The results of the parameters needed for each Tx to drive the array based on Fig. 4.39 are shown in Tab. 4.5. They are the same as the values at 30 V from Tab. 4.4.

Table 4.5: Each Tx's driving parameters for $f_{arr}=976.6$ kHz at 60 V.

Tx #	#01	#06	#09	#11	#14	#15	#17	#20	#28	#34
C_{ext} [pF]	52.89	0.00	71.06	46.35	33.25	94.70	135.08	67.21	106.59	119.22
Duty	0.20	0.23	0.19	0.20	0.20	0.16	0.18	0.20	0.16	0.17
Phase	109.4	97.7	112.9	107.0	108.4	122.3	114.4	107.0	123.2	117.0

4.2.4 qDE Balancing Discussion

The results presented in Sec. 4.2 suggest that binning transducers based on their electrical performance is critical in driving an array using the proposed qDE methods. The largest batch of transducers considered consisted of 40 TxS. This batch needed to be binned down to 10 TxS.

An outstanding question remains on whether the variance between TxS is primarily a result of the assembly process of elements and casing, or if it is primarily a result of the electrical impedance variance of the ceramic itself. If the variance is a result of the assembly process, better assembly methods could be developed to reduce the percentage of TxS removed during binning.

The python scripts could be further improved by incorporating a process to bin the elements into good groupings, rather than the user have rely on trial-and-error methods based on plotted waveforms.

It may be possible to significantly improve the binning process by implementing more direct computations of Tx equivalent electrical impedance characteristics, rather than relying on more indirect methods using interpretations of the S11 magnitude and power sweep plots.

4.3 FPGA Simulation

The verilog program was verified in ModelSim simulations prior to implementation into the FPGA using Quartus software. Once the functionality of the steering positions were verified for correct phase, the qDE solution phase and duty cycle were also included and verified. The FPGA was tested for B0 inhomogeneity in a 3T MR scanner.

4.3.1 Steering Position Phases

The array generated in MATLAB for 24 elements was simulated in ModelSim for verification. A figure with all 48 Tx signals and the PLL clock is shown in Fig. E.1. For the remainder of this section only the signals of the first 4 Tx's, the imaginary reference Tx, enable (EN), and position (POSITION) will be shown. The phases used for the ModelSim simulation are the same phases that were exported from MATLAB, as shown in Tab. C.1.

Fig. 4.41 shows both PWM signals for each of the first 4 Tx's. The enable pin and steering position are toggled at 2500 ns. The steering position is once changed at 5500 ns.

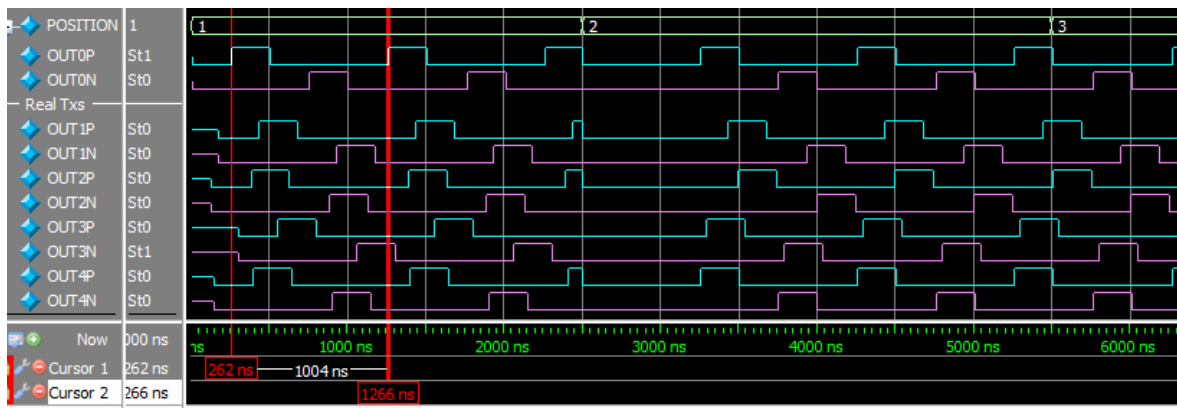


Figure 4.41: ModelSim : waveform plot with 8 signals from first 4 Tx's.

The duty cycle is determined by the qDE power balancing algorithm, not MATLAB. As such, they will all be temporarily set to 25% for the purpose of verifying the MATLAB steering phase shifts. Additionally, as the P and N gating signals are identical less the 180 degree phase shift, the N signals will no longer be shown in order to simplify the figures.

The phase shifts for the first 3 steering positions are verified by measuring the phase difference in time, then converting it to a phase shift based on the fundamental period. In this case, that period is 1000 ns. The focus position was changed every . The time delay between the reference Tx and the first Tx is shown between both cursors in Fig. 4.42.

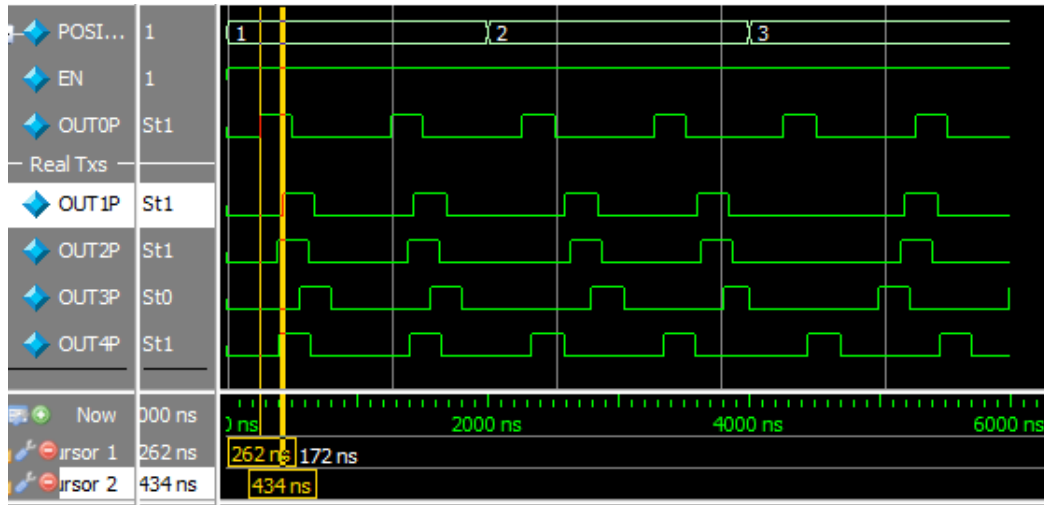


Figure 4.42: ModelSim : waveform plot with phase of first Tx at first steering position.

The delay measured in Fig. 4.42 is 172 ns; or 61.9 degrees. This is exactly the value indicated in Tab. C.1 for that Tx at that steering position.

The delay of the second Tx was verified at the second steering position, as shown in Fig. 4.43. The value of 360 ns results in 129.6 degrees, matching the value in table Tab. C.1.

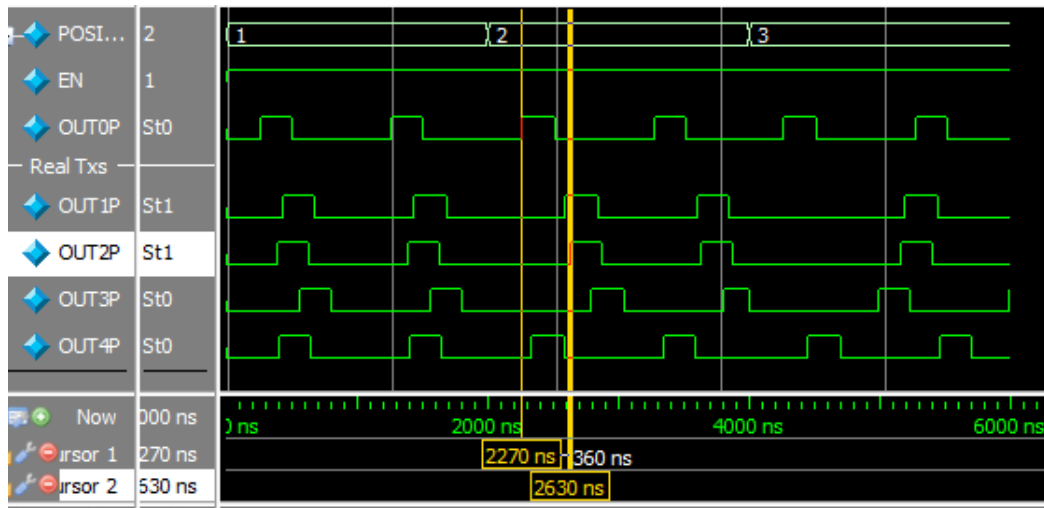


Figure 4.43: ModelSim : waveform plot with phase of 2nd Tx at 2nd steering position.

4.3.2 Combined Steering and Power Balancing

The qDE power balancing algorithm generates duty cycle unique to each Tx, and unique phases are calculated from these duty cycles. The evaluation of qDE derived a solution with a frequency of 976.6 kHz, as shown in Tab. 4.4. The MATLAB simulation generated a solution for 1 MHz. In reality, both the MATLAB simulations and qDE driving solutions would need to be redone at a frequency that is possible within the FPGA. The PLL limits the frequency resolution that is possible. In the interest of time, the qDE solutions will be applied to the MATLAB solutions regardless of the frequency difference. That would only show effect when hydrophone or MRI testing the array's performance.

The phases for the qDE solution found in was combined with the steering position phase shifts, the results of which are shown in Tab. 4.6.

Table 4.6: qDE driving duty and phase combined with steering position phases.

Tx #	#01	#06	#09	#11	#14	#15	#17	#20	#28	#34
Duty	0.20	0.23	0.19	0.20	0.20	0.16	0.18	0.20	0.16	0.17
Phase [Pos #1]	171.3	142.3	219.5	157.4	173.2	290.7	282.8	262.5	222.6	194.8
Phase [Pos #2]	227.5	227.3	303.0	132.9	405.1	315.2	472.9	380.6	424.2	307.1
Phase [Pos #3]	443.5	418.8	370.7	173.2	264.0	377.1	208.0	278.3	273.0	377.7

The values were added to the first 4 Tx and the phases and duty cycles were verified. The delay for Tx 1 was measured at 476 ns, providing a phase shift of 171.3 degrees for steering position 1. Tx 2 was measured at 632 ns, providing a phase shift of 227.5 degrees focused at steering position 3. Tx 3 was measured at 1028 ns, providing a phase shift of 370.1 degrees at the 3rd focus position. These values are exactly the same as those listed in Tab. 4.6, and the measurements are shown in Fig. 4.44. The duty cycles were also verified to be correct, with measurements shown in Fig. 4.45.

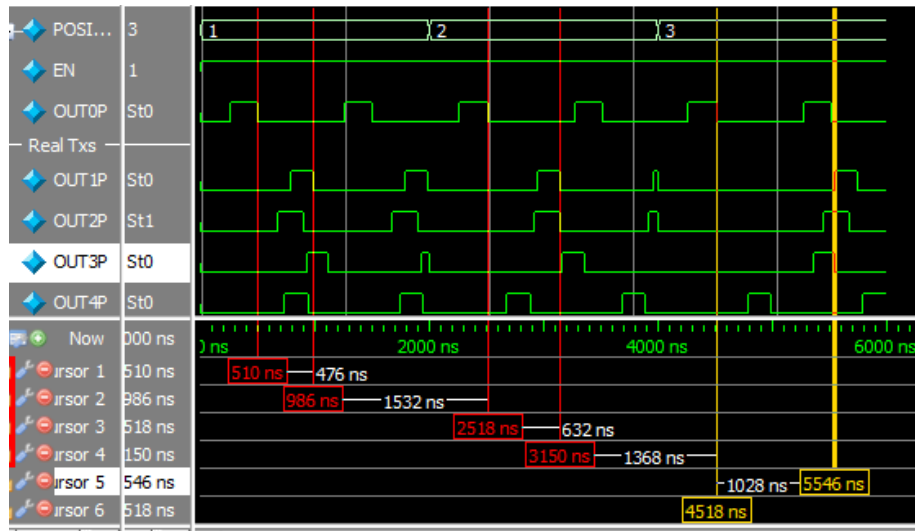


Figure 4.44: ModelSim : waveform plot with phase of 3rd Tx at 3rd steering position.

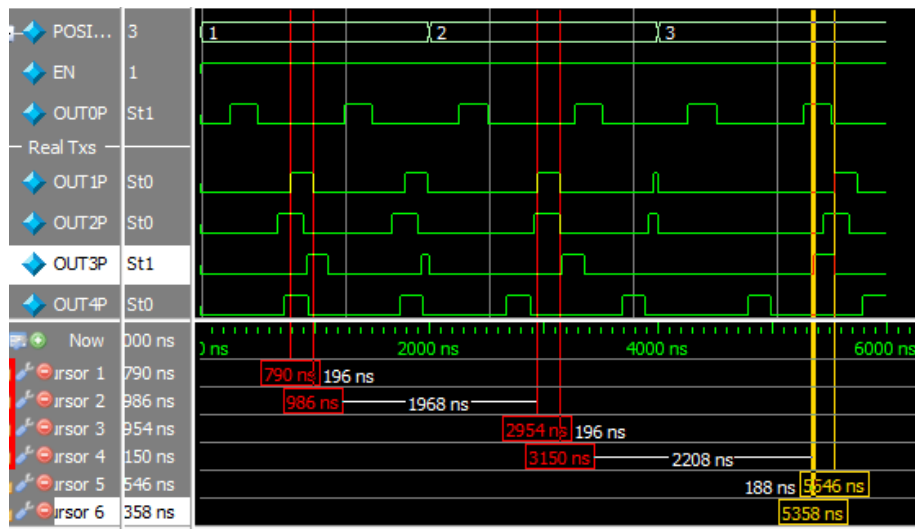


Figure 4.45: ModelSim : waveform plot with phase of 3rd Tx at 3rd steering position.

4.3.3 FPGA Discretization Limitations

The FPGA imposes hardware limitations that result in discretization of the phased array driving frequency () frequency, phase, and duty cycle. This section will attempt to determine the relative impact and consider the mitigating options available.

For the examples considered during the previous sections, a PLL clock speed of 250 MHz was selected as it was the highest frequency that was easily achieved on the DE0-Nano. To generate a of 1000 kHz, 250 steps are counted per period. To adjust to a lower value, the count period clock can be increased by an integer amount. If 251 steps occur per period, that results in a theoretical frequency of 996.0 kHz. In this case would have a step size of 4000 Hz, and the phase and duty cycle would have a resolution of 0.4 %.

Array Driving Frequency

Through the binning and design process of qDE driving shown in Sec. 4.2, is shown to be relatively sensitive to frequency changes. Fig. 4.37 shows that if changes by 500 Hz in either direction, the efficiency is decreased by 2 %. For functionality of transducer groupings, a frequency of at least 2000 Hz is advisable. As such, if efficient operation is a concern, could be considered to have a resolution requirement of 500 Hz.

Despite the resolution requirement of 500 Hz being much lower than the resolution of 4000 Hz previously shown, a more precise can be attained without increasing the number of steps per period by modifying the PLL ratio. For example, the PLL ratio was changed to have a 9x multiplier and 2x divider, resulting in a period count of 225 to generate 1 MHz. When it was increased to 226, the was changed to 995.6 kHz. This is only a 400 Hz difference from the generated previously of 996.0 kHz. therefore, by adjusting the PLL ratio, the effective frequency resolution can be drastically increased.

Phase Resolution

The consequence of lowering the value of the PLL frequency is that the total period count is lowered, which lowers the resolution of the phase and duty cycles. To test the tolerance for this resolution, acoustic simulations were executed in MATLAB with both the exact phases and the rounded phases. The resolution of the rounded phases was tested at both 25 and 50 %, meaning a period count of 4 and 2 respectively. The results showed a surprisingly high tolerance to phase resolution. Their results were compared, as shown in Fig. 4.46 and Fig. 4.47.

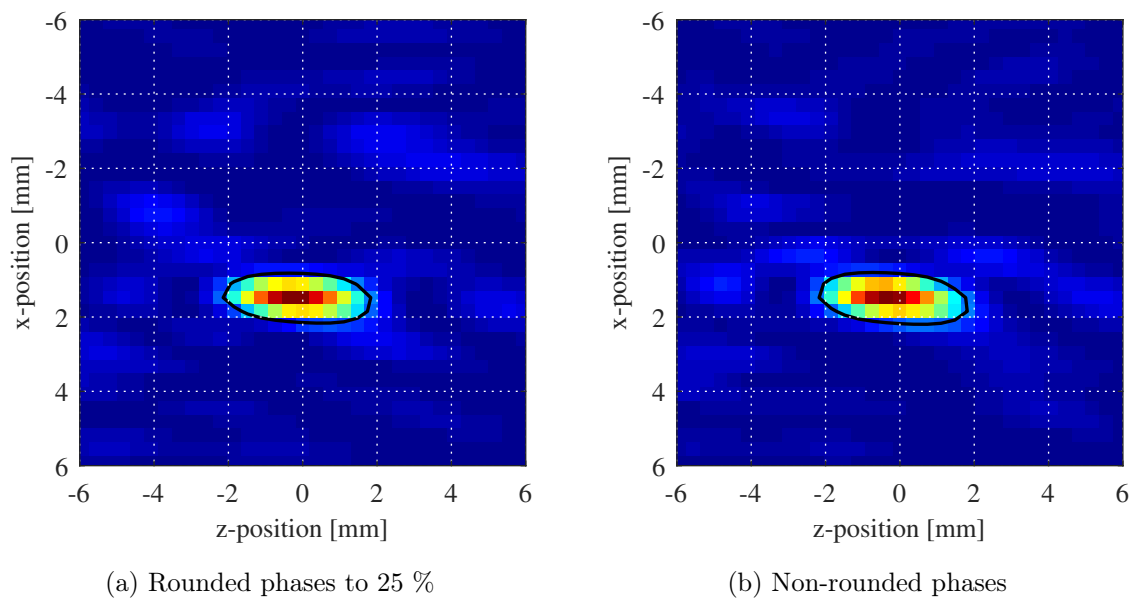


Figure 4.46: Normalized intensity comparing 25 % phase resolutions.

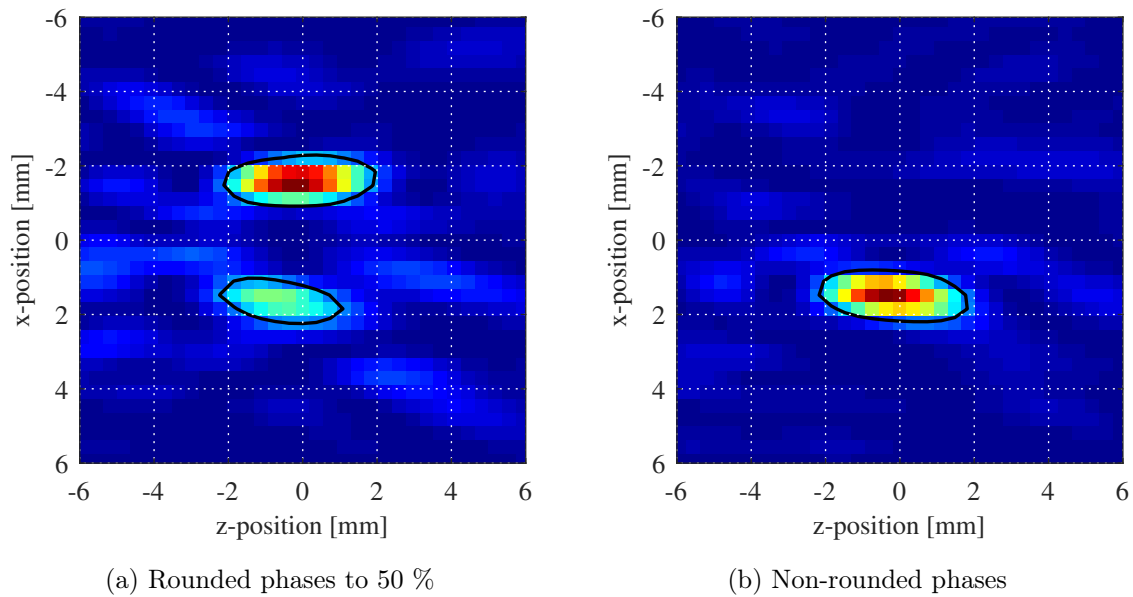
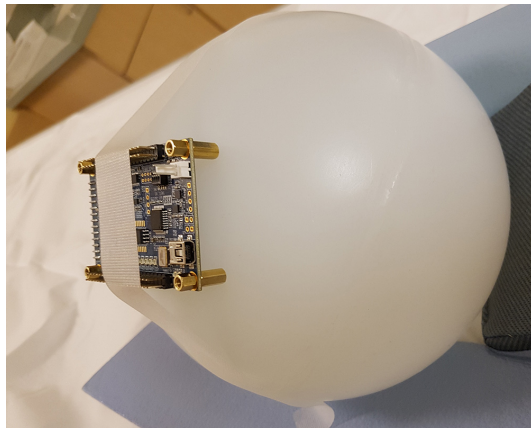


Figure 4.47: Normalized intensity comparing 50 % phase resolutions.

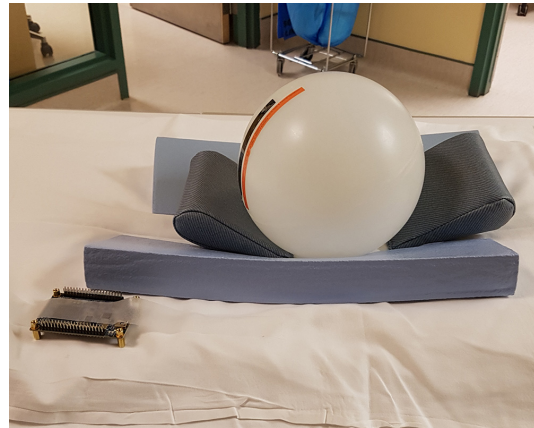
4.3.4 MRI B0 Field FPGA Testing

The FPGA was tested in a 3T MR scanner for its impact on field artifacts. The FPGA was placed at various distances from the phantom and the field was scanned to determine the distance at which interference was present. Before it was placed inside the MR bore, it was swiped with a magnet to ensure there were not strong magnetic forces, which would indicate the presence of relevant ferromagnetic materials. The USB connector was mildly attracted to the magnet, but it still deemed weak enough that it would be safe to proceed with testing.

The first test involved mounting the FPGA directly to the phantom, as shown in Fig. 4.48a. For the second test the FPGA was placed at a distance of about 10 inches from the phantom, as shown in Fig. 4.48b. The 3rd test done at an intermediate position between the first two.

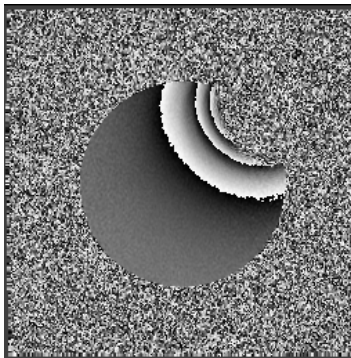


(a) On phantom

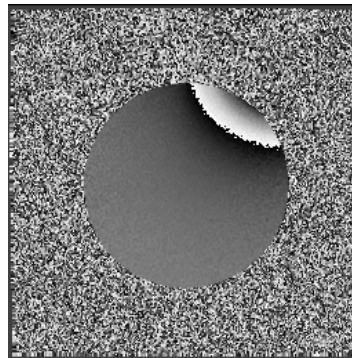


(b) 10" from phantom

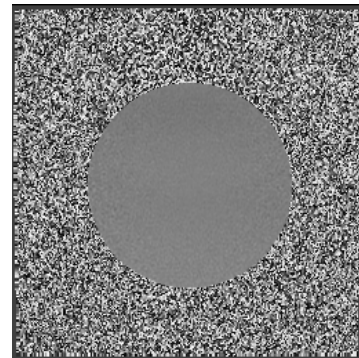
Figure 4.48: Pictures of phantom on MRI table with FPGA attached.



(a) On phantom



(b) 5" from phantom



(c) 10" from phantom

Figure 4.49: Pictures of phantom on MRI table with FPGA attached.

4.3.5 Discussion

The results from the ModelSim show the core of the verilog logic is correct; the phases and duty cycle are properly accounted for, and the FPGA can steer the array between known focal points on the fly with little computational effort.

Unfortunately active MR testing of the FPGA was not possible. Without verifying the functionality within the MR bore, nor its affect on MR imaging, the appropriateness of the system for MRgHIFU arrays cannot be concluded.

The appropriateness of the proposed system integration for non-MR compatible arrays is apparent. It is low-cost, can have a high number of PWM capable outputs, and provides sufficient resolution for phase, duty, and . Even the entry-level DE0-Nano's PLL clock with an upper limit near 250 MHz can likely meet the requirements for 2-3 MHz ultrasound signals, provided remains fixed during operation.

Fig. 4.46 shows that these arrays can have a surprising tolerance for phase resolution. A phase resolution of 25 % still showed sufficient performance, despite a slightly lower intensity gain.

If changing the without having to reprogram the FPGA is desired, it may be possible to change the PLL ratio on the fly based on the desired frequency and phase resolution tolerance.

4.4 Electrical Testing

A configuration of 4 Tx's was used to verify functionality and performance of the system. Prior to finding the qDE driving solution for this group of Tx's, the output capacitance of the drivers was measured and the capacitance of the oscilloscope probes. With this new value of parasitic capacitance a qDE driving solution was found, and the FPGA was reprogrammed accordingly. This ensures that measured results are fairly compared to expected results without distortion. The steering position was fixed to the centre position. The DC voltage of the qDE driver () was set to 30V.

The output voltage waveforms are composed of 3 states: (1) high voltage, (2) low voltage, and (3) high impedance. To demonstrate each state, the high impedance state is temporarily changed to a zero voltage state with low impedance, and the Tx's are disconnected from the drivers. The resultant voltage waveforms for arbitrary driving parameters are shown in Fig. 4.50.

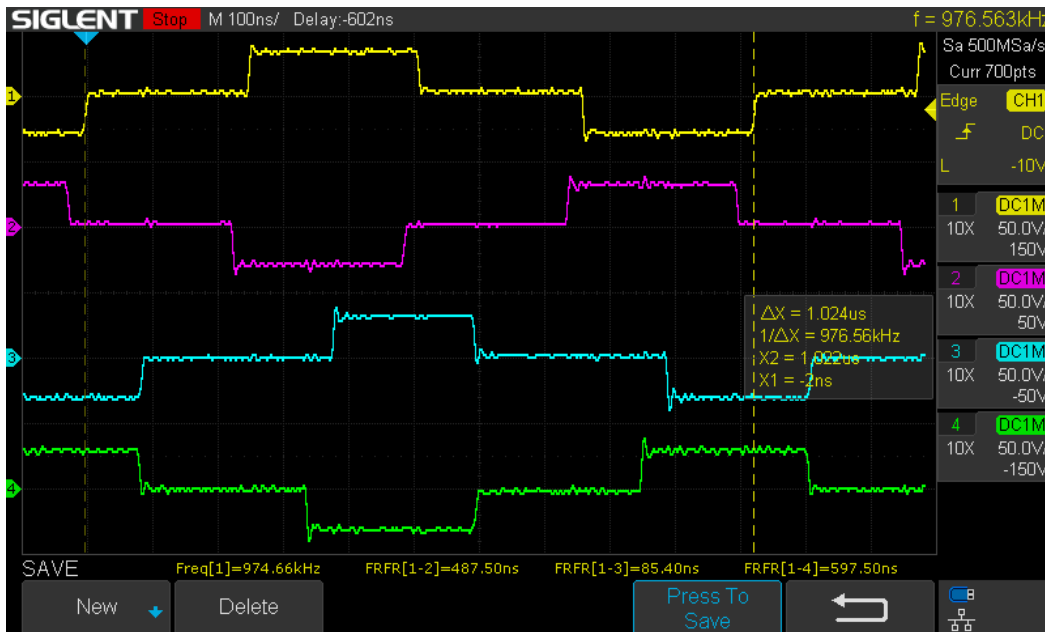


Figure 4.50: Arbitrary driver parameters a 0 V state in place of the high-impedance state.

The output capacitance of the drivers was estimated by measuring the output time constant () on an oscilloscope when a resistor was connected to an output. was measured after a 63.2 % change in value both exponential transitions, as shown in Fig. 4.51. The average was found to be 29.7 ns. The values of and the resistor are used to derive the capacitance:

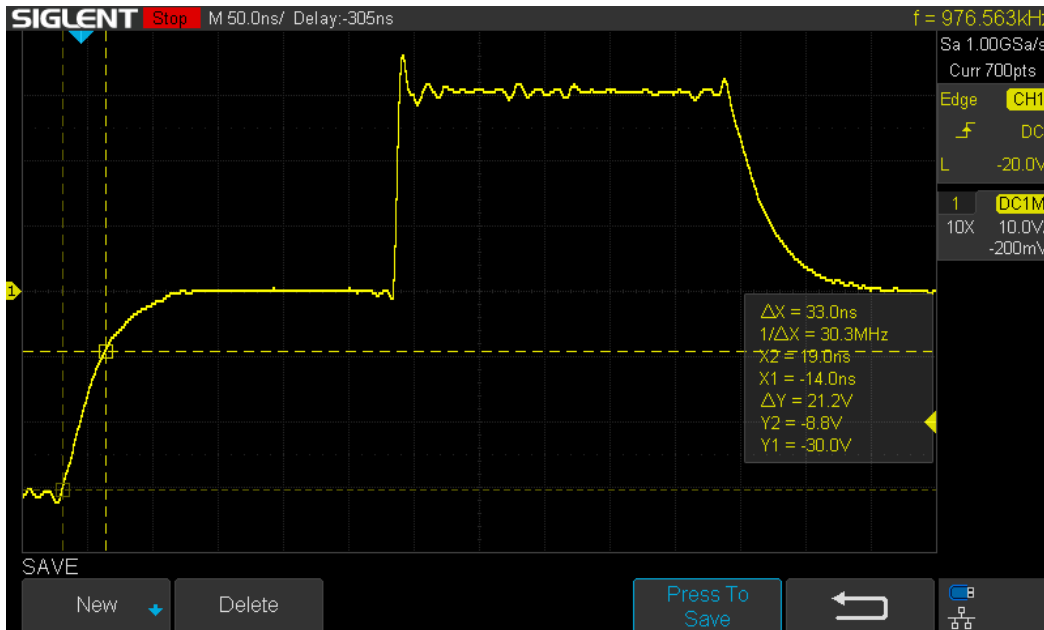


Figure 4.51: measurement of driver PCB output when loaded with resistor.

4.4.1 Driver Output Voltage Waveforms

A new qDE solution was found for the 4 Tx's under test to consider 96 pF output capacitance. The programmed and measured qDE driving parameters are shown in Tab. 4.7.

Table 4.7: Electrical testing programmed and measured driving parameters.

	Expected / Ideal				Measured / Used			
Tx #	15	17	28	34	15	17	28	34
[pF]	0	35	32	9.5	0	30	30	10
Duty [%]	22.6	25.0	20.8	24.8	23.0	23.0	19.3	22.9
Phase [%]	4.8	5	12.2	5.6	4.8	5.5	16.1	6.1
[]	0.50	0.48	0.08	0.58	0.56	0.57	0.28	0.43

When the third state is restored to high impedance, and the Tx remained disconnected, the 3rd state is not distinguishable because the output capacitance of the drivers does not have a path to discharge. This is shown in Fig. 4.52.

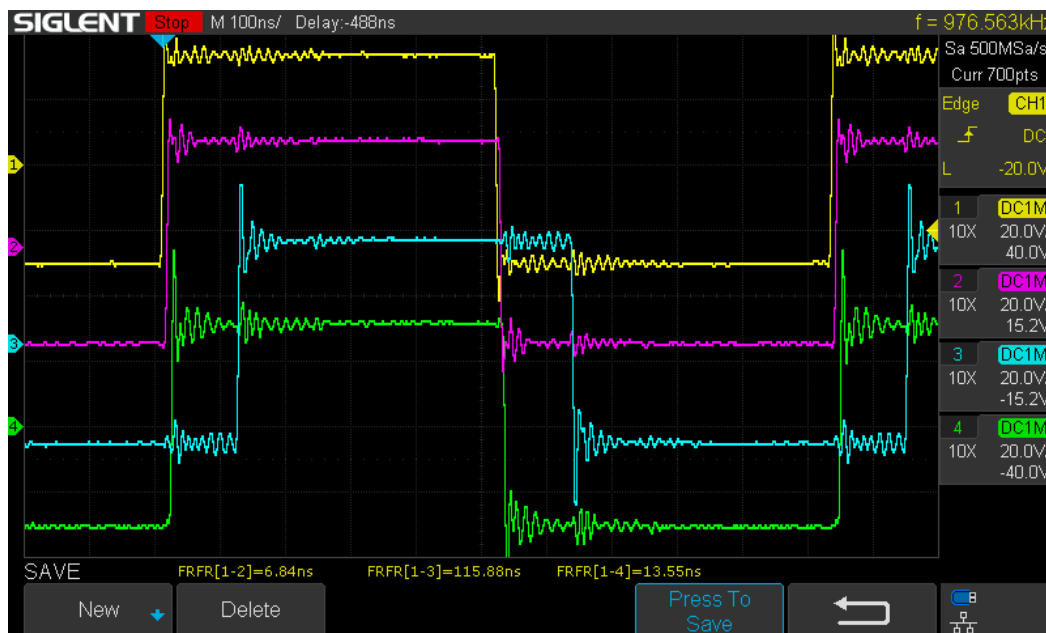


Figure 4.52: No-load driver output voltage with high-impedance state.

It is easier to distinguish the phase shifts before the Tx's are connected. The phase shifts are measured relative to Tx 15. They are shown in Fig. 4.53.

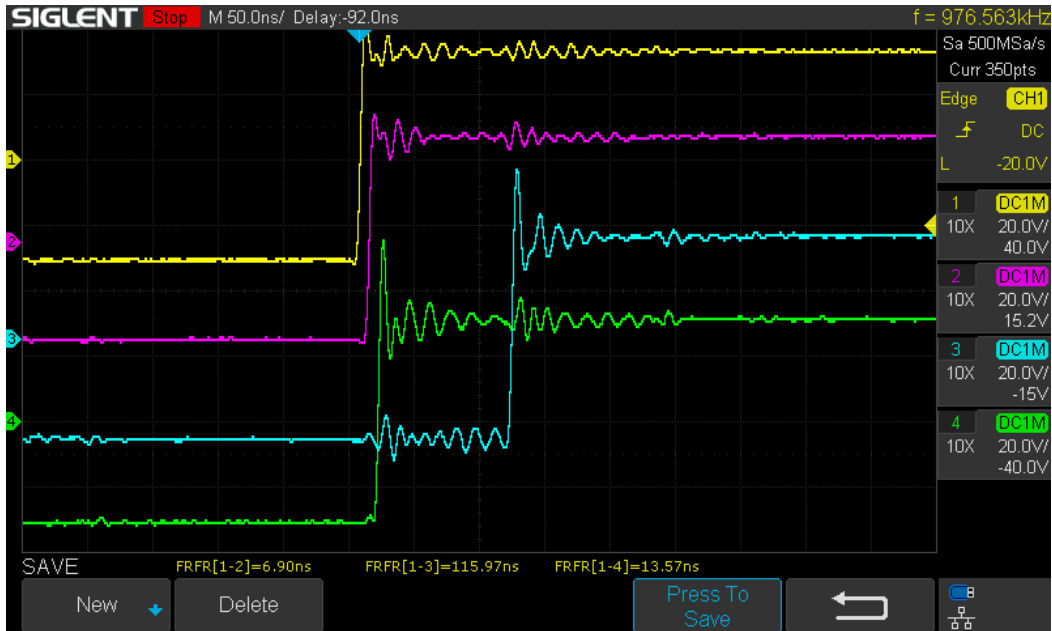


Figure 4.53: No-load driver output voltage with measured phase shifts.

The Tx's are attached to the driver, and the ratio of voltage difference () and duty () are measured. The measurements for the ratio of voltage difference () of Tx 28 is shown in Fig. 4.54.

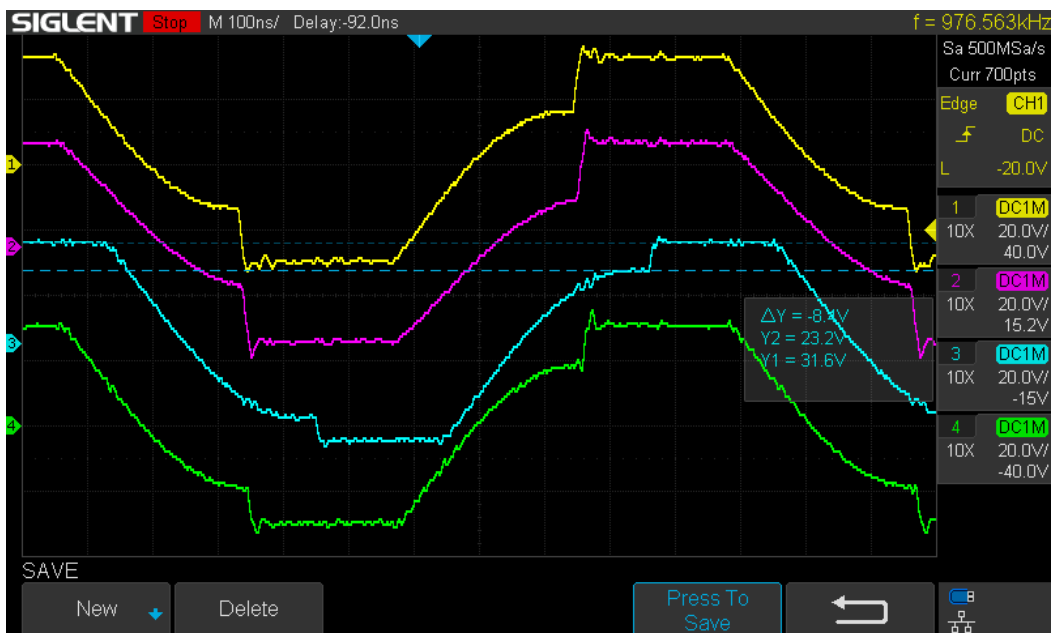


Figure 4.54: Driver output voltage with Tx's connected, showing a $\Delta Y = -8.1V$ measurement.

To test if there is acoustic interference between nearby Tx's on the array, some of the elements were selectively disconnected. The observable effects on the voltage waveforms were visible, but not significant. Removing the 2nd Tx had the most significant impact on the others Tx's, and the resultant waveforms with it removed are shown in Fig. 4.55.

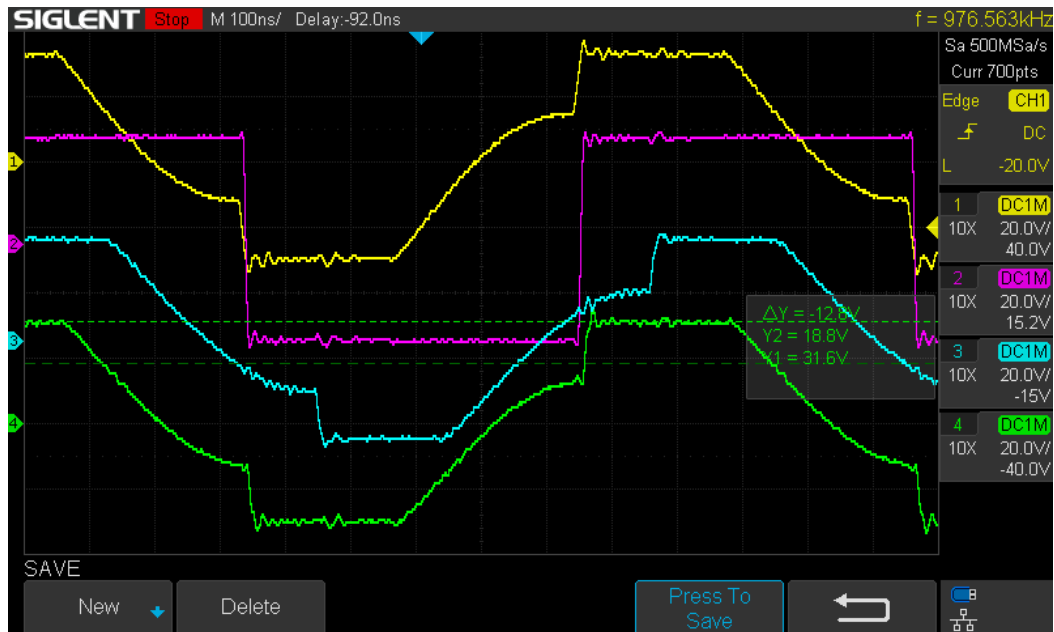


Figure 4.55: Driver output voltage with 4 Tx's connected.

The relative locations of the Tx's are shown in the picture of Fig. 4.56. This figure also shows Tx 28 disconnected.

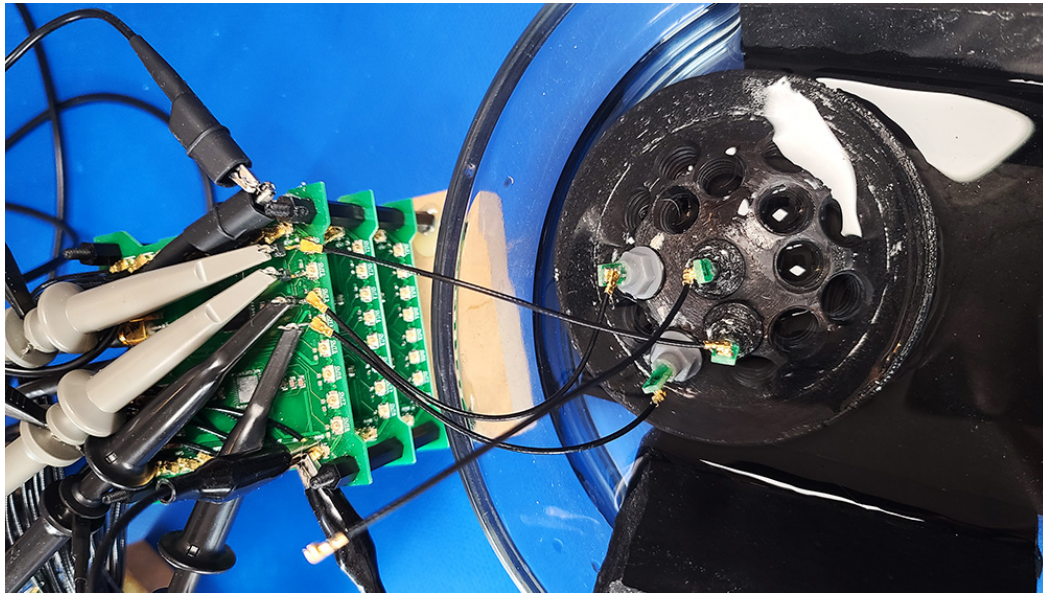


Figure 4.56: Picture of driver output voltage testbench.

4.4.2 Discussion

Tab. 4.7 shows reasonable conformity in the driving parameters between the measured and expected values. A phase discrepancy was noticeable, however it is acceptable considering the measurements were not done with high accuracy, and, as previously tested, the phase has a high tolerance to error. The discrepancy of measurements is also noticeable. This could be due to the rounding of the external capacitors used, or a variance of capacitance on different channels of the driver; only one output channel was tested.

The electrical tests demonstrate that the driving and control system both work as intended in a non-MR setting. It remains to be seen if the waveforms produce equal acoustic power, and if the same electrical performance remains in a MR environment. The acoustic power could be verified through hydrophone testing an entire array, or by independently measuring the acoustic power delivered from each element. The MR compatibility needs to be verified for both effects on the driving and control system, and the system's effects on the MR thermometry imaging.

Chapter 5

Conclusions

The results of this thesis demonstrate the potential of the proposed low-cost conformal phased array system integration, its potential use in applications of head and neck hyperthermia, and the feasibility of rapidly fabricating case-by-case target-oriented arrays. The functionality of the qDE driving system and FPGA were tested in a non-MR environment through simulation and electrical measurements. The design and fabrication process were investigated through acoustic and thermal simulations, and electrical testing.

MATLAB k-Wave acoustic and thermal simulations were used to estimate the performance of a sparse compact conformal transducer. The results indicate that solutions with a 1.5 mm off-axis steering range are possible using twenty-four 7 mm diameter PZT TxS. This is arguably small for an ideal head and neck hyperthermia solution, however, the steering range was doubled when the number of TxS was increased to thirty-six. This work shows that a compact conformal device with a low number of pseudo-randomly distributed TxS may yield sufficient performance for hyperthermia applications of head and neck tumours. It remains to be seen if the low number of TxS translates to acceptable performance in MR testing.

The application of the qDE driving method was successful in balancing the power delivered to all elements in theory, and in practice yielded voltage waveforms that were similar to expectations. The qDE method was successfully implemented with DL-47 7 mm diameter 1 MHz resonance Txs, however, the process of binning was critical to achieving reasonable performance. A group of 40 Txs was binned down to 12, indicating that more control and consistency is required in the fabrication of the Txs. The impacts of nearby transducers appeared negligible in electrical testing, which indicates that qDE tuning of Txs independent of array geometry should be possible.

The FPGA is able to sufficiently control the phase and duty cycle of each Tx at sufficient resolution. The MR tests of static magnetic field () susceptibility for the FPGA indicate that the DE0-Nano device may be sufficiently MR compatible for use directly within the MR bore.

Further work is needed to fully validate the system, such as hydrophone and MR imaging verification. The uncertainties of MR compatibility and reliability of the driving system require further testing to verify that the electrical measurements and functionality observed outside of the MR bore are properly translated during active MR thermometry. A drift in Tx performance over time and usage remains to be tested and may indicate that periodic re-tuning and/or re-binning of a group of Txs is required.

The advantage of this proposed platform extends beyond head and neck hyperthermia or spherical array designs. The independence of individual Txs, the threaded Tx casing design, the overall system modularity and scalability, and the rapid design and production process of array shells allow for new uses of HIFU not possible with current technology. 3D printed array shells can be designed to conform to a specific patient on a specific part of the body, ensuring the array is pointed exactly where it needs to be. For example, for head and neck hyperthermia applications a 3D printed collar can be fabricated to fit the patient with the Tx receptacles printed directly in the collar to point to the tumour. This would significantly mitigate the effects of patient movement.

Bibliography

- [1] K. Hynynen and R. M. Jones, “Image-guided ultrasound phased arrays are a disruptive technology for non-invasive therapy,” eng, *Physics in medicine and biology*, vol. 61, R206–48, 17 Sep. 2016.
- [2] J. G. Lynn, “A new method for the generation and use of focused ultrasound in experimental biology,” *The Journal of general physiology*, vol. 26, no. 2, pp. 179–193, 1942, ISSN: 1540-7748. DOI: 10.1085/jgp.26.2.179.
- [3] K. Hynynen, A. Darkazanli, E. Unger, and J. F. Schenck, “Mri-guided noninvasive ultrasound surgery,” *Medical Physics*, vol. 20, no. 1, pp. 107–115, Jan. 1993, ISSN: 0094-2405. DOI: 10.1118/1.597093.
- [4] W. J. Fry and F. J. Fry, “Fundamental neurological research and human neurosurgery using intense ultrasound,” *IRE Transactions on Medical Electronics*, vol. ME-7, no. 3, pp. 166–181, Jul. 1960, ISSN: 2168-0795. DOI: 10.1109/IRET-ME.1960.5008041.
- [5] R. H. Silverman, “Focused ultrasound in ophthalmology,” eng, *Clinical ophthalmology (Auckland, N.Z.)*, vol. 10, no. 27757007, pp. 1865–1875, Sep. 2016, ISSN: 1177-5483. DOI: 10.2147/OPHT.S99535. [Online]. Available: <https://www.ncbi.nlm.nih.gov/pmc/articles/PMC5053390/>.
- [6] G. T. Haar and C. Coussios, “High intensity focused ultrasound: Physical principles and devices.,” eng, *International journal of hyperthermia : the official journal of European Society for Hyperthermic Oncology, North American Hyperthermia Group*, vol. 23, pp. 89–104, 2 Mar. 2007.
- [7] I. Rivens, A. Shaw, J. Civale, and H. Morris, “Treatment monitoring and thermometry for therapeutic focused ultrasound,” *International Journal of Hyperthermia*, vol. 23, no. 2, pp. 121–139, 2007. DOI: 10.1080/02656730701207842. eprint: <https://doi.org/10.1080/02656730701207842>.

- [8] K. Hynynen, "Mri-guided focused ultrasound treatments," *Ultrasonics*, vol. 50, no. 2, pp. 221–229, 2010, ISSN: 0041-624X. DOI: 10.1016/j.ultras.2009.08.015. [Online]. Available: <http://www.sciencedirect.com/science/article/pii/S0041624X09001012>.
- [9] X. Fan and K. Hynynen, "The effect of wave reflection and refraction at soft tissue interfaces during ultrasound hyperthermia treatments.," eng, *The Journal of the Acoustical Society of America*, vol. 91, pp. 1727–36, 3 Mar. 1992.
- [10] F. J. Fry and F. R. Y. Francis J., "Chapter xiv - intense focused ultrasound: Its production, effects and utilization," in *Ultrasound*, Oxford: Elsevier, 1978, pp. 689–736. DOI: 10.1016/B978-0-444-41641-4.50011-X. [Online]. Available: <http://www.sciencedirect.com/science/article/pii/B978044441641450011X>.
- [11] A. Copelan, J. Hartman, M. Chehab, and A. M. Venkatesan, "High-intensity focused ultrasound: Current status for image-guided therapy," eng, *Seminars in interventional radiology*, vol. 32, no. 26622104, pp. 398–415, Dec. 2015, ISSN: 1098-8963. DOI: 10.1055/s-0035-1564793. [Online]. Available: <https://www.ncbi.nlm.nih.gov/pmc/articles/PMC4640913/>.
- [12] *First us approval of an mrgfus device*, English, Oct. 2020. [Online]. Available: <https://www.fusfoundation.org/the-technology/timeline-of-focused-ultrasound?view=article\&id=2260:first-us-approval-of-an-mrgfus-device\&catid=135:timeline>.
- [13] P. Wust, B. Hildebrandt, G. Sreenivasa, B. Rau, J. Gellermann, H. Riess, R. Felix, and P. M. Schlag, "Hyperthermia in combined treatment of cancer," *The Lancet Oncology*, vol. 3, no. 8, pp. 487–497, 2002, ISSN: 1470-2045. DOI: 10.1016/S1470-2045(02)00818-5. [Online]. Available: <http://www.sciencedirect.com/science/article/pii/S1470204502008185>.
- [14] N. R. Datta, S. G. Ordóñez, U. S. Gaipl, M. M. Paulides, H. Crezee, J. Gellermann, D. Marder, E. Puric, and S. Bodis, "Local hyperthermia combined with radiotherapy and/or chemotherapy: Recent advances and promises for the future," *Cancer Treatment Reviews*, vol. 41, no. 9, pp. 742–753, 2015, ISSN: 0305-7372. DOI: 10.1016/j.ctrv.2015.05.009. [Online]. Available: <http://www.sciencedirect.com/science/article/pii/S0305737215001048>.
- [15] W. C. Dewey, L. E. Hopwood, S. A. Sapareto, and L. E. Gerweck, "Cellular responses to combinations of hyperthermia and radiation," *Radiology*, vol. 123, no. 2, pp. 463–474, 1977, PMID: 322205. DOI: 10.1148/123.2.463. eprint: <https://doi.org/10.1148/123.2.463>.

- [16] P. M. Harari, K. H. Hynynen, R. B. Roemer, D. P. Anhalt, D. S. Shimm, B. Stea, and J. R. Cassady, "Development of scanned focussed ultrasound hyperthermia: Clinical response evaluation.," eng, *International journal of radiation oncology, biology, physics*, vol. 21, pp. 831–40, 3 Aug. 1991.
- [17] B. Emami, R. J. Myerson, H. Cardenes, K. G. Paris, C. A. Perez, W. Straube, L. Leybovich, M. Mildenerger, R. R. Kuske, V. R. Devineni, and N. Kucik, "Combined hyperthermia and irradiation in the treatment of superficial tumors: Results of a prospective randomized trial of hyperthermia fractionation (1/wk vs 2/wk)," *International Journal of Radiation Oncology*Biology*Physics*, vol. 24, no. 1, pp. 145–152, 1992, ISSN: 0360-3016. DOI: 10.1016/0360-3016(92)91034-K. [Online]. Available: <http://www.sciencedirect.com/science/article/pii/036030169291034K>.
- [18] J. van der Zee, D. González, G. C. van Rhoon, J. D. P. van Dijk, W. L. J. van Putten, and A. A. M. Hart, "Comparison of radiotherapy alone with radiotherapy plus hyperthermia in locally advanced pelvic tumours: A prospective, randomised, multicentre trial," *The Lancet*, vol. 355, no. 9210, pp. 1119–1125, Apr. 2000, ISSN: 0140-6736. DOI: 10.1016/S0140-6736(00)02059-6.
- [19] L. Zhu, M. B. Altman, A. Laszlo, W. Straube, I. Zoberi, D. E. Hallahan, and H. Chen, "Ultrasound hyperthermia technology for radiosensitization," eng, *Ultrasound in medicine & biology*, vol. 45, no. 30773377, pp. 1025–1043, May 2019, ISSN: 0301-5629. DOI: 10.1016/j.ultrasmedbio.2018.12.007. [Online]. Available: <https://www.ncbi.nlm.nih.gov/pmc/articles/PMC6475527/>.
- [20] M. R. Horsman, "Angiogenesis and vascular targeting: Relevance for hyperthermia," *International Journal of Hyperthermia*, vol. 24, no. 1, pp. 57–65, 2008. DOI: 10.1080/02656730701829710. eprint: <https://doi.org/10.1080/02656730701829710>.
- [21] J. L. R. Roti, "Cellular responses to hyperthermia (40–46°C): Cell killing and molecular events," *International Journal of Hyperthermia*, vol. 24, no. 1, pp. 3–15, 2008. DOI: 10.1080/02656730701769841. eprint: <https://doi.org/10.1080/02656730701769841>.
- [22] P. B. Elming, B. S. Sørensen, A. L. Oei, N. A. P. Franken, J. Crezee, J. Overgaard, and M. R. Horsman, "Hyperthermia: The optimal treatment to overcome radiation resistant hypoxia.," eng, *Cancers*, vol. 11, 1 Jan. 2019.
- [23] L. J. Anghileri and J. Robert, *Hyperthermia In Cancer Treatment: Volume 2*, en. CRC Press, Jun. 2019, Google-Books-ID: 9qWbDwAAQBAJ, ISBN: 9781000012682.

- [24] S. Rockwell, I. T. Dobrucki, E. Y. Kim, S. T. Marrison, and V. T. Vu, “Hypoxia and radiation therapy: Past history, ongoing research, and future promise.,” eng, *Current molecular medicine*, vol. 9, pp. 442–58, 4 May 2009.
- [25] D. A. Christensen and C. H. Durney, “Hyperthermia production for cancer therapy: A review of fundamentals and methods.,” eng, *The Journal of microwave power*, vol. 16, pp. 89–105, 2 Jun. 1981.
- [26] K. B. Ocheltree, P. J. Benkeser, L. A. Frizzell, and C. A. Cain, “An ultrasonic phased array applicator for hyperthermia,” *IEEE Transactions on Sonics and Ultrasonics*, vol. 31, no. 5, pp. 526–526, 1984, ISSN: 2162-1403. DOI: 10.1109/T-SU.1984.31537.
- [27] H. P. Kok, J. Crezee, N. A. P. Franken, L. J. A. Stalpers, G. W. Barendsen, and A. Bel, “Quantifying the combined effect of radiation therapy and hyperthermia in terms of equivalent dose distributions,” *International Journal of Radiation Oncology*Biophysics*, vol. 88, no. 3, pp. 739–745, 2014, ISSN: 0360-3016. DOI: 10.1016/j.ijrobp.2013.11.212. [Online]. Available: <http://www.sciencedirect.com/science/article/pii/S0360301613035372>.
- [28] C. M. van Leeuwen, J. Crezee, A. L. Oei, N. A. P. Franken, L. J. A. Stalpers, A. Bel, and H. P. Kok, “3d radiobiological evaluation of combined radiotherapy and hyperthermia treatments,” *International Journal of Hyperthermia*, vol. 33, no. 2, pp. 160–169, Nov. 2017, PMID: 27744728. DOI: 10.1080/02656736.2016.1241431. eprint: <https://doi.org/10.1080/02656736.2016.1241431>.
- [29] —, “The effect of time interval between radiotherapy and hyperthermia on planned equivalent radiation dose,” *International Journal of Hyperthermia*, vol. 34, no. 7, pp. 901–909, May 2018, PMID: 29749270. DOI: 10.1080/02656736.2018.1468930. eprint: <https://doi.org/10.1080/02656736.2018.1468930>.
- [30] E. Alsahafi, K. Begg, I. Amelio, N. Raulf, P. Lucarelli, T. Sauter, and M. Tavassoli, “Clinical update on head and neck cancer: Molecular biology and ongoing challenges.,” eng, *Cell death & disease*, vol. 10, p. 540, 8 Jul. 2019.
- [31] M. Canning, G. Guo, M. Yu, C. Myint, M. W. Groves, J. K. Byrd, and Y. Cui, “Heterogeneity of the head and neck squamous cell carcinoma immune landscape and its impact on immunotherapy,” eng, *Frontiers in cell and developmental biology*, vol. 7, no. 31024913, pp. 52–52, Apr. 2019, ISSN: 2296-634X. DOI: 10.3389/fcell.2019.00052. [Online]. Available: <https://www.ncbi.nlm.nih.gov/pmc/articles/PMC6465325/>.

- [32] D. Rischin, L. J. Peters, B. O'Sullivan, J. Giralt, R. Fisher, K. Yuen, A. Trotti, J. Bernier, J. Bourhis, J. Ringash, M. Henke, and L. Kenny, "Tirapazamine, cisplatin, and radiation versus cisplatin and radiation for advanced squamous cell carcinoma of the head and neck (trog 02.02, headstart): A phase iii trial of the trans-tasman radiation oncology group.," eng, *Journal of clinical oncology : official journal of the American Society of Clinical Oncology*, vol. 28, pp. 2989–95, 18 Jun. 2010.
- [33] K. A. R. Price and E. E. Cohen, "Current treatment options for metastatic head and neck cancer," *Current Treatment Options in Oncology*, vol. 13, no. 1, pp. 35–46, 2012, ISSN: 1534-6277. DOI: 10.1007/s11864-011-0176-y.
- [34] J.-P. Machiels, S. Subramanian, A. Ruzsa, G. Repassy, I. Lifirenko, A. Flygare, P. Sørensen, T. Nielsen, S. Lisby, and P. M. J. Clement, "Zalutumumab plus best supportive care versus best supportive care alone in patients with recurrent or metastatic squamous-cell carcinoma of the head and neck after failure of platinum-based chemotherapy: An open-label, randomised phase 3 trial.," eng, *The Lancet. Oncology*, vol. 12, pp. 333–43, 4 Apr. 2011.
- [35] J. Moskovitz, J. Moy, and R. L. Ferris, "Immunotherapy for head and neck squamous cell carcinoma," eng, *Current oncology reports*, vol. 20, no. 29502288, pp. 22–22, Mar. 2018, ISSN: 1523-3790. DOI: 10.1007/s11912-018-0654-5. [Online]. Available: <https://www.ncbi.nlm.nih.gov/pmc/articles/PMC5835060/>.
- [36] M. M. Paulides, G. M. Verduijn, and N. Van Holthe, "Status quo and directions in deep head and neck hyperthermia," *Radiation Oncology*, vol. 11, no. 1, p. 21, 2016, ISSN: 1748-717X. DOI: 10.1186/s13014-016-0588-8.
- [37] S. Pichardo, M. Köhler, J. Lee, and K. Hynnyen, "In vivo optimisation study for multi-baseline mr-based thermometry in the context of hyperthermia using mr-guided high intensity focused ultrasound for head and neck applications.," eng, *International journal of hyperthermia : the official journal of European Society for Hyperthermic Oncology, North American Hyperthermia Group*, vol. 30, pp. 579–92, 8 Dec. 2014.

- [38] J. Lee, G. Farha, I. Poon, I. Karam, K. Higgins, S. Pichardo, K. Hynynen, and D. Enepekides, "Magnetic resonance-guided high-intensity focused ultrasound combined with radiotherapy for palliation of head and neck cancer-a pilot study," eng, *Journal of therapeutic ultrasound*, vol. 4, no. 27042308, pp. 12–12, Apr. 2016, ISSN: 2050-5736. DOI: 10.1186/s40349-016-0055-x. [Online]. Available: <https://www.ncbi.nlm.nih.gov/pmc/articles/PMC4818916/>.
- [39] K. Chinzei, R. Kikinis, and F. A. Jolesz, "Mr compatibility of mechatronic devices: Design criteria," in *Medical Image Computing and Computer-Assisted Intervention - MICCAI'99*, C. Taylor and A. Colchester, Eds., Berlin, Heidelberg: Springer Berlin Heidelberg, 1999, pp. 1020–1030.
- [40] E. S. Ebbini and C. A. Cain, "A spherical-section ultrasound phased array applicator for deep localized hyperthermia," *IEEE Transactions on Biomedical Engineering*, vol. 38, no. 7, pp. 634–643, 1991, ISSN: 1558-2531. DOI: 10.1109/10.83562.
- [41] H. Wan, P. VanBaren, E. S. Ebbini, and C. A. Cain, "Ultrasound surgery: Comparison of strategies using phased array systems," *IEEE Transactions on Ultrasonics, Ferroelectrics, and Frequency Control*, vol. 43, no. 6, pp. 1085–1098, 1996, ISSN: 1525-8955. DOI: 10.1109/58.542052.
- [42] X. Wu and M. Sherar, "Theoretical evaluation of moderately focused spherical transducers and multi-focus acoustic lens/transducer systems for ultrasound thermal therapy," *Physics in Medicine and Biology*, vol. 47, no. 9, pp. 1603–1621, Apr. 2002. DOI: 10.1088/0031-9155/47/9/313.
- [43] A. Partanen, M. Tillander, P. S. Yarmolenko, B. J. Wood, M. R. Dreher, and M. O. Kohler, "Reduction of peak acoustic pressure and shaping of heated region by use of multifoci sonications in mr-guided high-intensity focused ultrasound mediated mild hyperthermia," eng, *Medical physics*, vol. 40, no. 23298120, pp. 013 301–013 301, Jan. 2013, ISSN: 0094-2405. DOI: 10.1118/1.4769116. [Online]. Available: <https://www.ncbi.nlm.nih.gov/pmc/articles/PMC3537758/>.
- [44] V. Chaplin and C. F. Caskey, "Multi-focal hifu reduces cavitation in mild-hyperthermia," eng, *Journal of therapeutic ultrasound*, vol. 5, no. 28413682, pp. 12–12, Apr. 2017, ISSN: 2050-5736. DOI: 10.1186/s40349-017-0089-8. [Online]. Available: <https://www.ncbi.nlm.nih.gov/pmc/articles/PMC5390440/>.
- [45] A. Payne, U. Vyas, N. Todd, J. de Bever, D. A. Christensen, and D. L. Parker, "The effect of electronically steering a phased array ultrasound transducer on near-field tissue heating," eng, *Medical physics*, vol. 38, no. 21978041, pp. 4971–4981, Sep. 2011, ISSN: 0094-2405. DOI: 10.1118/1.3618729. [Online]. Available: <https://www.ncbi.nlm.nih.gov/pmc/articles/PMC3166338/>.

- [46] R. C. Preston, "Measurement and characterisation of the acoustic output of medical ultrasonic equipment part 1," *Medical and Biological Engineering and Computing*, vol. 24, no. 2, pp. 113–120, 1986, ISSN: 1741-0444. DOI: 10.1007/BF02443923. [Online]. Available: <https://doi.org/10.1007/BF02443923>.
- [47] C. A. Cain and S. Umemura, "Concentric-ring and sector-vortex phased-array applicators for ultrasound hyperthermia," *IEEE Transactions on Microwave Theory and Techniques*, vol. 34, no. 5, pp. 542–551, 1986, ISSN: 1557-9670. DOI: 10.1109/TMTT.1986.1133390.
- [48] E. S. Ebbini, S. I. Umemura, M. Ibbini, and C. A. Cain, "A cylindrical-section ultrasound phased-array applicator for hyperthermia cancer therapy," *IEEE Transactions on Ultrasonics, Ferroelectrics, and Frequency Control*, vol. 35, no. 5, pp. 561–572, 1988, ISSN: 1525-8955. DOI: 10.1109/58.8034.
- [49] X. Fan and K. Hynynen, "Ultrasound surgery using multiple sonications—treatment time considerations.," eng, *Ultrasound in medicine & biology*, vol. 22, pp. 471–82, 4 1996.
- [50] S. A. Goss, L. A. Frizzell, J. T. Kouzmanoff, J. M. Barich, and J. M. Yang, "Sparse random ultrasound phased array for focal surgery," *IEEE Transactions on Ultrasonics, Ferroelectrics, and Frequency Control*, vol. 43, no. 6, pp. 1111–1121, 1996, ISSN: 1525-8955. DOI: 10.1109/58.542054.
- [51] L. R. Gavrilov and J. W. Hand, "A theoretical assessment of the relative performance of spherical phased arrays for ultrasound surgery," *IEEE Transactions on Ultrasonics, Ferroelectrics, and Frequency Control*, vol. 47, no. 1, pp. 125–139, 2000, ISSN: 1525-8955. DOI: 10.1109/58.818755.
- [52] K. P. Morrison, G. W. Keilman, and P. J. Kaczkowski, "Single archimedean spiral close packed phased array hifu," in *2014 IEEE International Ultrasonics Symposium*, 2014, pp. 400–404. DOI: 10.1109/ULTSYM.2014.0099.
- [53] B. I. Raju, C. S. Hall, and R. Seip, "Ultrasound therapy transducers with space-filling non-periodic arrays," *IEEE Transactions on Ultrasonics, Ferroelectrics, and Frequency Control*, vol. 58, no. 5, pp. 944–954, 2011, ISSN: 1525-8955. DOI: 10.1109/TUFFC.2011.1895.
- [54] R. D. Saunders and H. Smith, "Safety aspects of mr clinical imaging," *Br Med Bull*, vol. 40, no. 2, pp. 148–154, Jan. 1984, ISSN: 0007-1420. DOI: 10.1093/oxfordjournals.bmb.a071961.
- [55] R. E. Gangarosa, J. E. Minnis, J. Nobbe, D. Praschan, and R. W. Genberg, "Operational safety issues in mri.," eng, *Magnetic resonance imaging*, vol. 5, pp. 287–92, 4 1987.

- [56] E. Kanal, F. G. Shellock, and L. Talagala, "Safety considerations in mr imaging.," eng, *Radiology*, vol. 176, pp. 593–606, 3 Sep. 1990.
- [57] J. F. Schenck, "The role of magnetic susceptibility in magnetic resonance imaging: Mri magnetic compatibility of the first and second kinds.," eng, *Medical physics*, vol. 23, pp. 815–50, 6 Jun. 1996.
- [58] L. P. Panych and B. Madore, "The physics of mri safety," *J. Magn. Reson. Imaging*, vol. 47, no. 1, pp. 28–43, Jan. 2018, ISSN: 1053-1807. DOI: 10.1002/jmri.25761.
- [59] U.S. Department of Health and Human Services Food and Drug Administration Center for Devices and Radiological Health. "Testing and labeling medical devices for safety in the magnetic resonance (mr) environment. draft guidance for industry and food and drug administration staff," United States Food and Drug Administration. (Aug. 2, 2019), [Online]. Available: <https://www.fda.gov/regulatory-information/search-fda-guidance-documents/testing-and-labeling-medical-devices-safety-magnetic-resonance-mr-environment>.
- [60] R. H. Hashemi, W. G. Bradley, and C. J. Lisanti, *MRI: The Basics*, ser. The Basics Series. Lippincott Williams & Wilkins, 2010. [Online]. Available: <https://books.google.ca/books?id=v4LFgAHxNz4C>.
- [61] C. Pamboucas and P. Nihoyannopoulos, "Cardiovascular magnetic resonance at 3 tesla: Advantages, limitations and clinical potential.," eng, *Hellenic journal of cardiology : HJC = Hellenike kardiologike epitheorese*, vol. 47, pp. 170–3, 3 May 2006.
- [62] C. A. for Drugs and T. in Health, "1.5 tesla magnetic resonance imaging scanner versus 3.0 tesla magnetic resonance imaging scanners: A review of the clinical evidence, cost-effectiveness, and guidelines," eng, Ottawa, Tech. Rep., Sep. 2012. [Online]. Available: <https://www.deslibris.ca/ID/234909>.
- [63] J. M. D. Coey, *Magnetism and magnetic materials*. Cambridge, UK ; Cambridge University Press, 2010.
- [64] D. R. Daum, M. T. Buchanan, T. Fjield, and K. Hynynen, "Design and evaluation of a feedback based phased array system for ultrasound surgery," *IEEE Transactions on Ultrasonics, Ferroelectrics, and Frequency Control*, vol. 45, no. 2, pp. 431–438, 1998, ISSN: 1525-8955. DOI: 10.1109/58.660153.

- [65] G. K. J. Lewis and W. L. Olbricht, "Design and characterization of a high-power ultrasound driver with ultralow-output impedance.," eng, *The Review of scientific instruments*, vol. 80, p. 114 704, 11 2009.
- [66] T. Kobus and N. McDannold, "Update on clinical magnetic resonance-guided focused ultrasound applications," eng, *Magnetic resonance imaging clinics of North America*, vol. 23, no. 26499282, pp. 657–667, Nov. 2015, ISSN: 1064-9689. DOI: 10.1016/j.mric.2015.05.013. [Online]. Available: <https://www.ncbi.nlm.nih.gov/pmc/articles/PMC4621790/>.
- [67] A. Bozkurt, O. Farhanieh, R. B. Roy, and A. S. Ergun, "Design of a driver ic for an ultrasound catheter ablation system," in *2014 IEEE International Ultrasonics Symposium*, 2014, pp. 1536–1539. DOI: 10.1109/ULTSYM.2014.0380.
- [68] L. Capineri, "A 15 mhz bandwidth, 60 vpp, low distortion power amplifier for driving high power piezoelectric transducers," *Review of Scientific Instruments*, vol. 85, no. 10, p. 104 701, Oct. 2014, ISSN: 0034-6748. DOI: 10.1063/1.4897155. [Online]. Available: <https://doi.org/10.1063/1.4897155>.
- [69] C. Christoffersen, W. Wong, S. Pichardo, G. Togtema, and L. Curiel, "Class-de ultrasound transducer driver for hifu therapy," *IEEE Transactions on Biomedical Circuits and Systems*, vol. 10, no. 2, pp. 375–382, 2016, ISSN: 1940-9990. DOI: 10.1109/TBCAS.2015.2406119.
- [70] R. Song, C. Christoffersen, S. Pichardo, and L. Curiel, "An integrated full-bridge class-de ultrasound transducer driver for hifu applications," in *2016 14th IEEE International New Circuits and Systems Conference (NEWCAS)*, 2016, pp. 1–4. DOI: 10.1109/NEWCAS.2016.7604776.
- [71] T. Yuan, X. Dong, H. Shekhani, C. Li, Y. Maida, T. Tou, and K. Uchino, "Driving an inductive piezoelectric transducer with class e inverter," *Sensors and Actuators A: Physical*, vol. 261, pp. 219–227, 2017, ISSN: 0924-4247. DOI: 10.1016/j.sna.2017.05.021. [Online]. Available: <http://www.sciencedirect.com/science/article/pii/S0924424716308524>.
- [72] C. Christoffersen, T. Ngo, R. Song, Y. Zhou, S. Pichardo, and L. Curiel, "Quasi class-de driving of hifu transducer arrays," *IEEE Transactions on Biomedical Circuits and Systems*, vol. 13, no. 1, pp. 214–224, 2019, ISSN: 1940-9990. DOI: 10.1109/TBCAS.2018.2888990.
- [73] O. Farhanieh, A. Sahafi, R. B. Roy, A. S. Ergun, and A. Bozkurt, "Integrated hifu drive system on a chip for cmut-based catheter ablation system," *IEEE Transactions on Biomedical Circuits and Systems*, vol. 11, no. 3, pp. 534–546, 2017, ISSN: 1940-9990. DOI: 10.1109/TBCAS.2017.2649942.

- [74] *Ieee standard on piezoelectricity*, 1988. DOI: 10.1109/IEEESTD.1988.79638.
- [75] E. Hafner, “The piezoelectric crystal unit—definitions and methods of measurement,” *Proceedings of the IEEE*, vol. 57, no. 2, pp. 179–201, 1969, ISSN: 1558-2256. DOI: 10.1109/PROC.1969.6912.
- [76] W. Wong, C. Christoffersen, S. Pichardo, and L. Curiel, “An integrated ultrasound transducer driver for hifu applications,” in *2013 26th IEEE Canadian Conference on Electrical and Computer Engineering (CCECE)*, May 2013, pp. 1–5. DOI: 10.1109/CCECE.2013.6567791.
- [77] I. E. Commission, *Iec 61161:2013*, 2013.
- [78] M. Greenspan and C. E. Tschiegg, “Tables of the speed of sound in water,” *The Journal of the Acoustical Society of America*, vol. 31, no. 1, pp. 75–76, Jan. 1959, ISSN: 0001-4966. DOI: 10.1121/1.1907614. [Online]. Available: <https://doi.org/10.1121/1.1907614>.
- [79] B. E. Treeby and B. T. Cox, “Modeling power law absorption and dispersion for acoustic propagation using the fractional laplacian,” *The Journal of the Acoustical Society of America*, vol. 127, no. 5, pp. 2741–2748, May 2010, ISSN: 0001-4966. DOI: 10.1121/1.3377056. [Online]. Available: <https://doi.org/10.1121/1.3377056>.
- [80] G. ter Haar, A. Shaw, S. Pye, B. Ward, F. Bottomley, R. Nolan, and A.-M. Coady, “Guidance on reporting ultrasound exposure conditions for bio-effects studies,” *Ultrasound in Medicine and Biology*, vol. 37, no. 2, pp. 177–183, Feb. 2011, ISSN: 0301-5629. DOI: 10.1016/j.ultrasmedbio.2010.10.021. [Online]. Available: <https://doi.org/10.1016/j.ultrasmedbio.2010.10.021>.
- [81] A. J. Livett and R. C. Preston, “A comparison of the aium/nema, iec and fda (1980) definitions of various acoustic output parameters for ultrasonic transducers,” *Ultrasound in Medicine & Biology*, vol. 11, no. 6, pp. 793–802, 1985, ISSN: 0301-5629. DOI: [https://doi.org/10.1016/0301-5629\(85\)90073-0](https://doi.org/10.1016/0301-5629(85)90073-0). [Online]. Available: <http://www.sciencedirect.com/science/article/pii/S0301562985900730>.
- [82] M. S. Canney, M. R. Bailey, L. A. Crum, V. A. Khokhlova, and O. A. Sapozhnikov, “Acoustic characterization of high intensity focused ultrasound fields: A combined measurement and modeling approach,” *The Journal of the Acoustical Society of America*, vol. 124, no. 19062878, pp. 2406–2420, Oct. 2008, ISSN: 0001-4966. DOI: 10.1121/1.2967836. [Online]. Available: <https://www.ncbi.nlm.nih.gov/pmc/articles/PMC2677345/>.

- [83] Y. Zhou, L. Zhai, R. Simmons, and P. Zhong, "Measurement of high intensity focused ultrasound fields by a fiber optic probe hydrophone," eng, *The Journal of the Acoustical Society of America*, vol. 120, no. 16938956, pp. 676–685, Aug. 2006, ISSN: 1520-8524. DOI: 10.1121/1.2214131. [Online]. Available: <https://www.ncbi.nlm.nih.gov/pmc/articles/PMC1994996/>.
- [84] C. I. Zanelli, S. DeMarta, C. W. Hennige, and M. M. Kadri, "Beamforming for therapy with high intensity focused ultrasound (hifu) using quantitative schlieren," in *1993 Proceedings IEEE Ultrasonics Symposium*, 1993, 1233–1238 vol.2. DOI: 10.1109/ULTSYM.1993.339610.
- [85] Y. Paul, D. V. M. Barthez, R. Léveillé, V. Peter, and D. V. M. Scrivani, "Side lobes and grating lobes artifacts in ultrasound imaging," *Veterinary Radiology & Ultrasound*, vol. 38, no. 5, pp. 387–393, 1997. DOI: <https://doi.org/10.1111/j.1740-8261.1997.tb02104.x>. eprint: <https://onlinelibrary.wiley.com/doi/pdf/10.1111/j.1740-8261.1997.tb02104.x>. [Online]. Available: <https://onlinelibrary.wiley.com/doi/abs/10.1111/j.1740-8261.1997.tb02104.x>.
- [86] IT'IS Foundation, *Tissue properties database v4.0*, en, May 15, 2018. DOI: 10.13099/VIP21000-04-0.
- [87] V. F. Humphrey, "Nonlinear propagation in ultrasonic fields: Measurements, modelling and harmonic imaging," *Ultrasonics*, vol. 38, no. 1, pp. 267–272, 2000, ISSN: 0041-624X. DOI: 10.1016/S0041-624X(99)00122-5. [Online]. Available: <http://www.sciencedirect.com/science/article/pii/S0041624X99001225>.
- [88] T. G. Muir and E. L. Carstensen, "Prediction of nonlinear acoustic effects at biomedical frequencies and intensities," *Ultrasound in Medicine & Biology*, vol. 6, no. 4, pp. 345–357, 1980, ISSN: 0301-5629. DOI: 10.1016/0301-5629(80)90004-6. [Online]. Available: <http://www.sciencedirect.com/science/article/pii/0301562980900046>.
- [89] L. Filipczyński, T. Kujawska, R. Tymkiewicz, and J. Wójcik, "Nonlinear and linear propagation of diagnostic ultrasound pulses," *Ultrasound in Medicine & Biology*, vol. 25, no. 2, pp. 285–299, 1999, ISSN: 0301-5629. DOI: 10.1016/S0301-5629(98)00174-4. [Online]. Available: <http://www.sciencedirect.com/science/article/pii/S0301562998001744>.

- [90] M. Tabei, T. D. Mast, and R. C. Waag, “A k-space method for coupled first-order acoustic propagation equations,” *The Journal of the Acoustical Society of America*, vol. 111, no. 1, pp. 53–63, 2002. DOI: 10.1121/1.1421344. eprint: <https://doi.org/10.1121/1.1421344>. [Online]. Available: <https://doi.org/10.1121/1.1421344>.
- [91] M. D. Verweij, B. E. Treeby, v. K. W. A. Dongen, and L. Demi, “Simulation of ultrasound fields,” in *Comprehensive Biomedical Physics*, A. Brahme, Ed., Elsevier, 2014, pp. 465–499. DOI: [urn:nbn:nl:ui:25-db6c7fa2-2a2b-4953-949c-cc376f100800](https://nbn:nl:ui:25-db6c7fa2-2a2b-4953-949c-cc376f100800). [Online]. Available: [https://research.tue.nl/nl/publications/simulation-of-ultrasound-fields\(db6c7fa2-2a2b-4953-949c-cc376f100800\).html](https://research.tue.nl/nl/publications/simulation-of-ultrasound-fields(db6c7fa2-2a2b-4953-949c-cc376f100800).html).
- [92] B. T. Cox, J. G. Laufer, K. P. Kostli, and P. C. Beard, “Experimental validation of photoacoustic k-space propagation models,” vol. 5320, Jul. 2004. DOI: 10.1117/12.531178. [Online]. Available: <https://doi.org/10.1117/12.531178>.
- [93] B. E. Treeby, J. Jaros, A. P. Rendell, and B. T. Cox, “Modeling nonlinear ultrasound propagation in heterogeneous media with power law absorption using a k-space pseudospectral method,” *The Journal of the Acoustical Society of America*, vol. 131, no. 6, pp. 4324–4336, Jun. 2012, ISSN: 0001-4966. DOI: 10.1121/1.4712021. [Online]. Available: <https://doi.org/10.1121/1.4712021>.
- [94] B. Treeby, B. Cox, and J. Jaros, *K-wave user manual*, version 1.1.
- [95] J. L. Robertson, B. T. Cox, and B. E. Treeby, “Quantifying numerical errors in the simulation of transcranial ultrasound using pseudospectral methods,” in *2014 IEEE International Ultrasonics Symposium*, Sep. 2014, pp. 2000–2003. DOI: 10.1109/ULTSYM.2014.0498.
- [96] C. Christoffersen, *20mm transducer array characterization for class de driving with experimental results*, en, 2018. DOI: 10.24433/CO.851D8745-9A18-4035-B8CF-24A786D0765E.V2.

Appendices

Appendix A

Extracted Transducer Characteristics

Table A.1: Extracted transducer characteristic from group A transducers, around .

Tx name							
T001	964	384	147	995	11.3	2408	39
T004	970	596	103	999	7.8	3441	36
T005	963	574	135	997	15.3	1786	20
T006	961	462	112	993	8.6	3191	43
T009	969	645	75	997	4.9	5516	54
T010	966	545	98	994	6.8	4009	46
T011	950	551	149	990	12.5	2240	26
T012	975	515	26	996	1.1	23816	291
T013	966	435	97	994	6.1	4417	64

Table A.2: Extracted transducer characteristic from group A transducers, around

Tx name							
T001	1062	391	111	1086	5.6	3983	64
T004	1076	806	59	1090	1.7	12731	99
T005	1070	587	84	1094	4.2	5231	56
T006	1055	537	75	1083	4.4	5146	60
T009	1062	593	102	1083	5.1	4372	46
T010	1062	563	69	1090	4.0	5594	62
T011	1054	591	123	1085	12.9	1766	19
T012	1061	473	117	1090	7.8	2872	38
T013	1061	604	95	1082	4.8	4679	49

Table A.3: Extracted transducer characteristic from group B transducers.

Tx name							
T001	293	345	193	320	37.9	7787	142
T002	289	270	305	313	52.9	5719	133
T003	288	138	398	315	76.7	3970	181
T004	291	379	275	312	43.5	6896	114
T005	290	199	126	312	19.8	15222	481
T006	291	233	210	313	32.7	9153	247
T007	290	262	728	305	92.8	3241	78

Table A.4: Extracted transducer characteristic from 31 of 40 group C transducers.

Tx name							
01	965	382	54	985	2.3	11984	197
03	976	254	139	985	2.8	9616	238
04	970	571	100	985	3.7	7259	80
05	966	427	148	985	7.1	3820	56
06	965	534	45	985	1.9	14262	168
09	969	688	69	985	2.6	10447	95
10	965	507	72	985	3.1	8762	109
11	965	688	55	985	2.4	11397	104
12	975	489	35	985	0.7	36368	467
13	972	388	134	985	4.0	6747	109
14	965	450	67	985	2.9	9477	132
15	965	518	95	985	4.3	6294	76
17	971	498	6	985	0.2	149840	1891
19	968	261	197	985	7.6	3564	86
20	965	235	46	985	1.9	14373	384
22	971	263	137	985	4.0	6710	161
23	972	262	110	985	3.0	8919	214
24	975	287	45	985	0.9	30135	661
25	970	156	105	985	3.4	8021	323
28	967	287	125	985	4.9	5515	121
30	970	220	139	985	4.5	6043	172
34	971	534	42	985	1.2	22754	267
36	969	244	118	985	4.0	6744	173
37	975	514	22	985	0.4	59782	730
39	968	422	140	985	5.7	4730	70
40	976	236	37	985	0.7	37455	999

Appendix B

MATLAB Function Descriptions

B.1 Prime Number Search

To balance memory increases with computation efficiency a factor ,`N_range_scale`, is defined by the user to limit how much the grid size can increase when searching for a prime number. The lowest prime number within the range is selected. The relevant section of code is shown in Fig. B.1, where an `N_range_scale` value of 1.5 is selected.

```
N_range_scale = 1.5; % scale to increase N_min
for i = N_min:N_max % find prime numbers
    factors_max(i - N_min + 1) = max(factor(i));
end
for i = primes(100) % find lowest prime number
    number = N_min + find(factors_max == i) - 1;
    if isfinite(number)
        N_optimal = min(number);
        break
    else
        N_optimal = N_min;
    end
end
```

Figure B.1: `FUS_Array_Prime.m` : Find prime numbers for grid sizes.

B.2 FUS_Array_GenRandSpherical.m

The function `FUS_Array_GenRandSpherical.m` was created to fit the required number of tx onto the array surface using a pseudo-random approach, but reproducible with the same parameters. The variables passed to this function include the seed, array geometry, the number of Tx's, and the Tx total diameter including casing. The seeds are used for the random number generator. Each time functions attempts to find a seed, it generates a new point in spherical coordinates that are between the bounds of theta and phi. The points are then converted to rectangular coordinates and verified to see if they are within a certain proximity of any other point. If they are, then it attempts to find a location again but with the next random number in the sequence associated with that seed. If there are no proximity breaches, then it is considered a good position, and the function either attempts to find a Tx position or exits the function because the required number of tx positions were found. The relevant code is shown in Fig. B.2.

```

search_limit = 500; % limit for attempts at finding location
rng(seed); % set seed for random number generator
while failed == 0 && run == 1
    for m = 1:N
        cond = 0; % initialize flag for breaking while loop
        while cond == 0
            for search = 0:search_limit
                S(m,1) = r;
                S(m,2) = rand*theta;
                S(m,3) = rand*phi;
                x = S(m,1)*cos(S(m,2))*sin(S(m,3));
                y = S(m,1)*sin(S(m,2))*sin(S(m,3));
                z = S(m,1)*cos(S(m,3));
                D = sqrt( (x-C(:,1)).^2 + (y-C(:,2)).^2 + (z-C(:,3)).^2 );
                C(m,1) = x; C(m,2) = y; C(m,3) = z;
                D_count = sum( D < X ); % # of 'D' less than min tx spacing
                if D_count == 0
                    cond = 1; % exit due to minimum distance
                    break;
                end
            end
            if search >= search_limit
                failed = 1; % failed due to attempt limit
                return;
            end
        end % end ---> for search = 1:search_limit
    end % end ---> while cond == 0
end % end ---> for m = 1:N
if m >= N % if required number of valid tx locations is acheived
    run = 0;
end
end
end

```

Figure B.2: `FUS_Array_GenRandSpherical.m` : Searching for valid tx positions.

Appendix C

MATLAB Simulation Exported Phases

Table C.1: Phases [degrees] exported from MATLAB for FPGA implementation.

Tx #	Pos #1	Pos #2	Pos #3	Pos #4	Pos #5	Pos #6	Pos #7
x [mm]	0.00	1.50	-1.50	0.00	0.00	0.00	0.00
y [mm]	0.00	0.00	0.00	1.50	-1.50	0.00	0.00
z [mm]	-1.50	0.00	0.00	0.00	0.00	0.00	1.50
1	61.9	118.1	334.1	288.0	162.7	180.0	17.3
2	44.6	129.6	321.1	50.4	41.8	180.0	33.1
3	106.6	190.1	257.8	60.5	31.7	180.0	335.5
4	50.4	25.9	66.2	148.3	302.4	180.0	27.4
5	64.8	296.6	155.5	311.0	139.7	180.0	14.4
6	168.5	193.0	254.9	226.1	221.8	180.0	277.9
7	168.5	358.6	93.6	126.7	316.8	180.0	277.9
8	155.5	273.6	171.4	270.7	180.0	180.0	289.4
9	99.4	301.0	149.8	220.3	229.0	180.0	342.7
10	77.8	190.1	260.6	136.8	315.4	180.0	1.4
11	139.7	191.5	259.2	197.3	250.6	180.0	303.8
12	164.2	280.8	164.2	181.4	269.3	180.0	282.2
13	145.4	194.4	254.9	253.4	193.0	180.0	299.5
14	96.5	90.7	2.9	239.0	208.8	180.0	345.6
15	174.2	95.0	357.1	321.1	122.4	180.0	272.2
16	169.9	321.1	122.4	60.5	31.7	180.0	276.5
17	174.2	132.5	312.5	319.7	132.5	180.0	272.2
18	122.4	267.8	182.9	214.6	233.3	180.0	321.1
19	36.0	13.0	79.2	33.1	59.0	180.0	41.8
20	90.7	230.4	217.4	7.2	85.0	180.0	351.4
21	171.4	135.4	309.6	132.5	318.2	180.0	275.0
22	172.8	296.6	155.5	302.4	142.6	180.0	273.6
23	60.5	283.7	167.0	99.4	352.8	180.0	18.7
24	92.2	30.2	63.4	211.7	237.6	180.0	348.5

Appendix D

Driver Printed Circuit Board Schematic

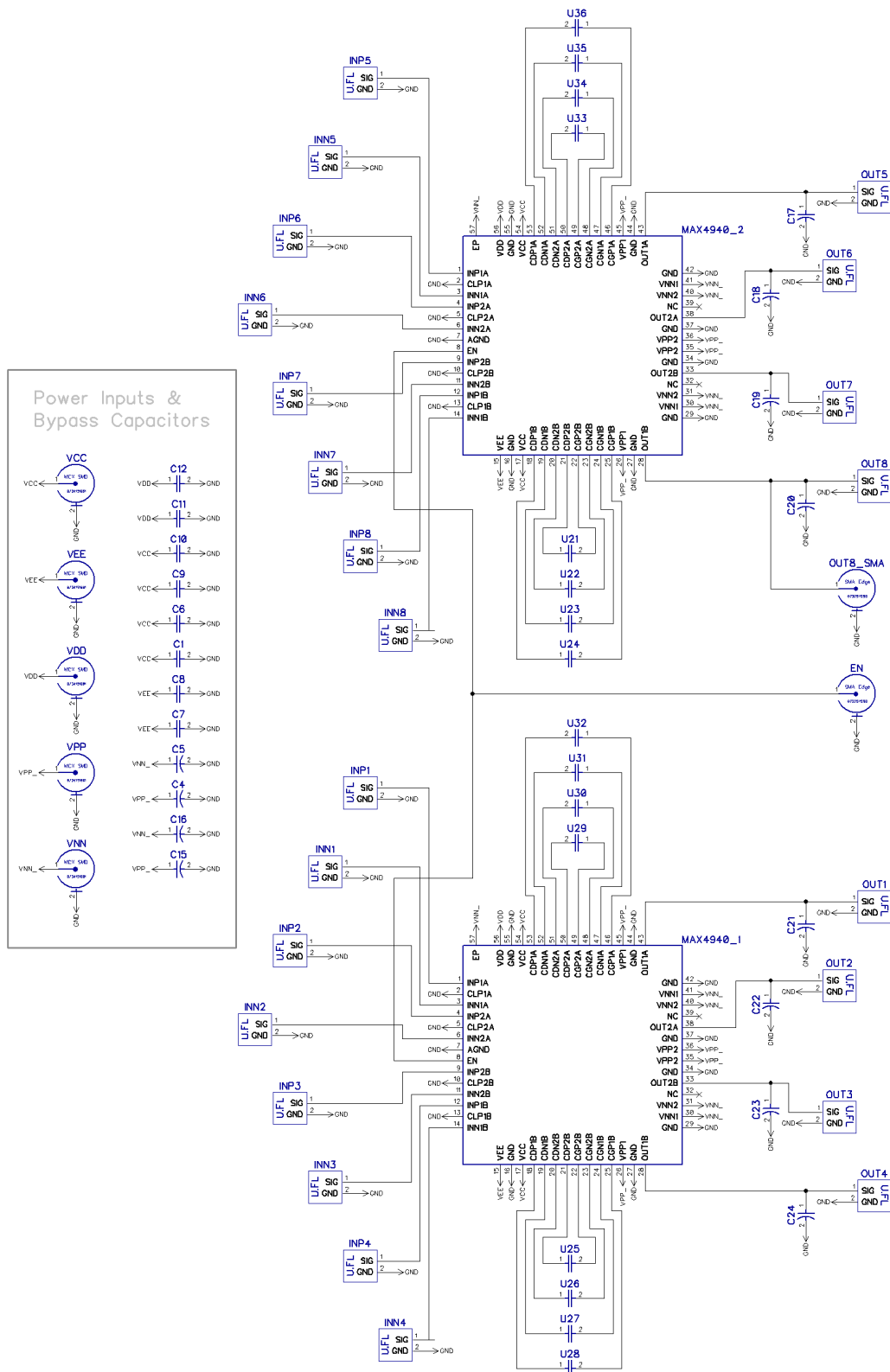


Figure D.1: Driver PCB v2 electrical schematic.

Appendix E

ModelSim Waveform

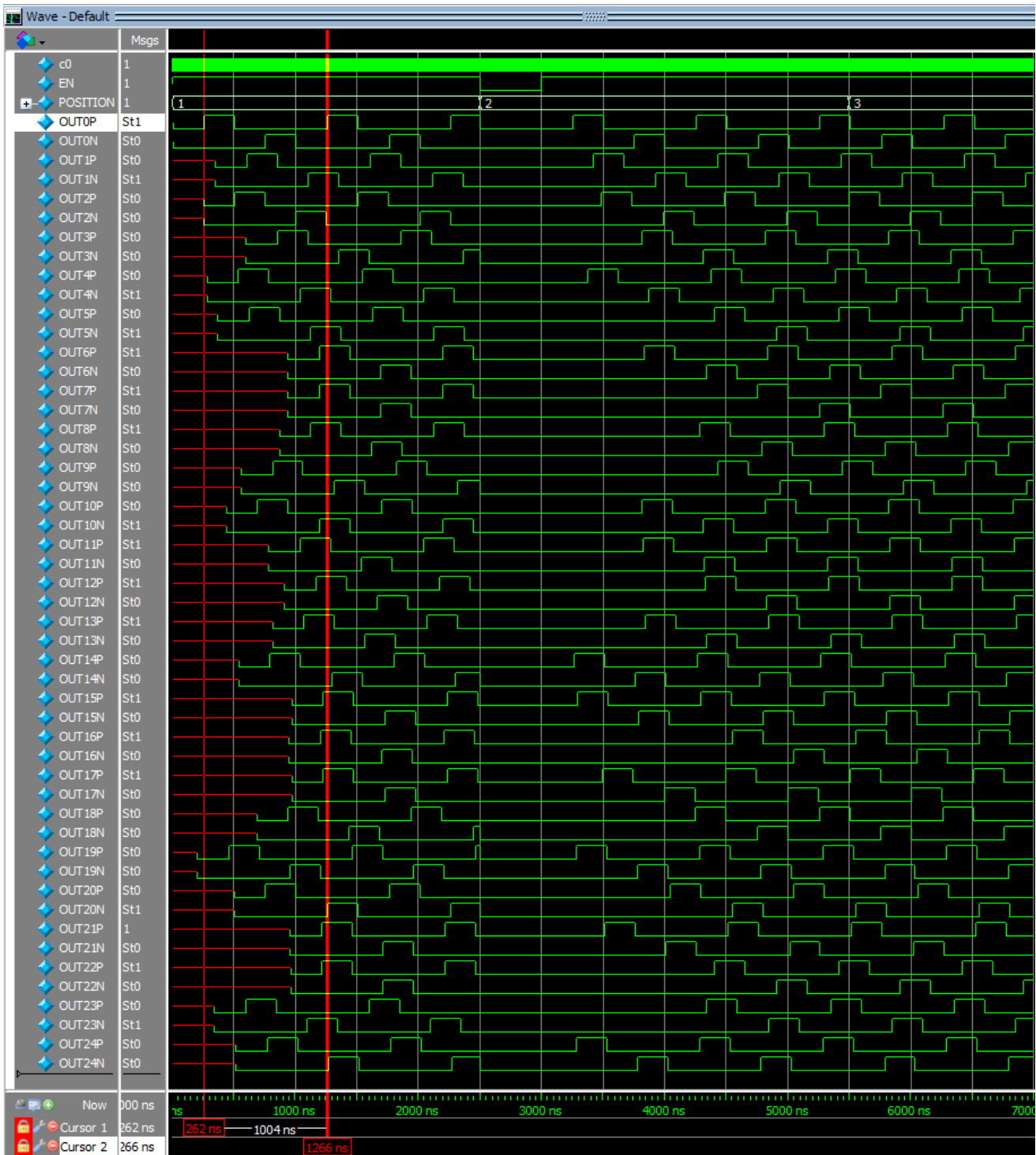


Figure E.1: ModelSim waveform showing all 48 tx signals for 24 tx array.